



Chair of Materials Physics

Master's Thesis



Selective Laser Melting of a Zr-based Bulk  
Metallic Glass for Medical Applications

Mirjam Spuller, BSc

November 2021



**MONTANUNIVERSITÄT LEOBEN**

www.unileoben.ac.at

**EIDESSTÄTTLICHE ERKLÄRUNG**

Ich erkläre an Eides statt, dass ich diese Arbeit selbständig verfasst, andere als die angegebenen Quellen und Hilfsmittel nicht benutzt, und mich auch sonst keiner unerlaubten Hilfsmittel bedient habe.

Ich erkläre, dass ich die Richtlinien des Senats der Montanuniversität Leoben zu "Gute wissenschaftliche Praxis" gelesen, verstanden und befolgt habe.

Weiters erkläre ich, dass die elektronische und gedruckte Version der eingereichten wissenschaftlichen Abschlussarbeit formal und inhaltlich identisch sind.

Datum 02.11.2021

*Mirjam Spuller*

\_\_\_\_\_  
Unterschrift Verfasser/in  
Mirjam Spuller

## Acknowledgments

First of all, I would like to thank my supervisor Dr. Wolfgang Waldhauser for giving me the opportunity to work on this interesting topic. Likewise, I would like to thank Univ. Prof. Dr. Jürgen Eckert for his supervision. Their support, patience and wide knowledge in this field were extremely helpful for creating this thesis and provided me with a solid basis for my future scientific career.

Furthermore, a thank you is owed to the team of Joanneum Research in Niklasdorf, who supported and encouraged me throughout the whole experimental part of this thesis. Additionally, I would like to thank Dr. Anton Hohenwarter and Mag. Dr. Florian Spieckermann for any technical support and inspiring discussions. Moreover, I would like to thank Gerda Grünbacher for carrying out the cytotoxicity, cell adhesion and cell growth tests. Without all that, my thesis would not have been possible in this form.

Also, I would like to thank my friends for their encouraging words during the period of working on this thesis. It would have been much harder without their mental support. Particularly, I would like to thank Philipp and Julia, who are always there for me.

Finally, I would like to thank my family, especially my parents, for supporting my studies at the University of Leoben; they always stand by my side and offer me the support I needed to achieve my aims in both life and work. Thank you for your parental care throughout my whole life.

## Abstract

Selective laser melting (SLM) is a promising additive manufacturing technique to fabricate biocompatible bulk metallic glass (BMG) components for medical applications such as personalized implants or scaffolds. The aim of this thesis was to find appropriate process parameters in order to produce fully dense and glassy samples from a Zr-based metallic glass powder (trade name VIT105). Besides, mechanical properties, biocompatibility, and influences of a post processing were investigated to examine the BMG's suitability for its use in the medical field. To achieve this goal, a SLM parameter study was conducted as a first step. Then, those fabricated samples were investigated regarding their relative density, microstructure, and thermodynamic behaviour. In addition, (micro-)hardness measurements were carried out. Afterwards, further samples were fabricated with a satisfying process parameter combination and subjected to different heat and surface treatments. 4-point bending test and cytotoxicity tests were carried out using these samples. Within the cytotoxicity tests, cell adhesion and cell growth on the samples surfaces were examined as well.

The SLM parameter study showed that a minimum volume energy density is needed for the production of dense samples. However, not only the volume energy density is decisive for the relative density but also the specific combination of the process parameters. Especially the scanning velocity of the laser plays a crucial role in the production of the BMG. It was found that it has a considerable impact on the resulting microstructure and determines the structural relaxation, glass transition temperature and indentation elastic modulus of the sample. 4-point bending tests showed that the as-built samples exhibit adequate flexural strengths and elasticity. Nonetheless, the investigations also showed that the BMG's properties strongly depend on the building direction and orientation of the testing. Furthermore, it was discovered that a blasting treatment with glass microbeads or corundum is beneficial to achieve higher flexural strengths. However, only samples blasted with glass microbeads are undoubtedly biocompatible. Samples treated with corundum are cytotoxic. Even if a heat treatment below the glass transition temperature improves the cell viability, it impairs the mechanical performance of the BMG. Moreover, the investigations pointed out that samples which are crystallised are unsuitable with respect to their manufacturability and usability.



## Kurzfassung

Selektives Laserschmelzen (SLM) ist eine vielversprechende additive Fertigungstechnik zur Herstellung biokompatibler Komponenten aus massivem metallischen Glas (BMG), welche als personalisierte Implantate oder Scaffolds Anwendung finden sollen. Ziel dieser Arbeit war es, geeignete Prozessparameter zu finden, um aus einem Zr-basierten metallischen Glaspulver (Handelsname VIT105) massive Proben mit amorpher Mikrostruktur herzustellen. Außerdem wurden mechanische Eigenschaften, Biokompatibilität und Einflüsse einer Nachbehandlung untersucht, um die Eignung des BMGs für den medizinischen Bereich zu ermitteln. Dazu wurde im ersten Schritt eine SLM-Parameterstudie durchgeführt. Die Proben aus dieser Studie wurden hinsichtlich ihrer relativen Dichte, Mikrostruktur und ihres thermodynamischen Verhaltens untersucht. Außerdem wurden (Mikro-)Härtemessungen durchgeführt. Anschließend wurden weitere Proben mit einer geeigneten Prozessparameterkombination hergestellt und verschiedenen Wärme- und Oberflächenbehandlungen unterzogen. An diesen Proben wurden 4-Punkt-Biegetests und Zytotoxizitätstests durchgeführt. Zusätzlich wurde im Rahmen der Zytotoxizitätstests auch die Zelladhäsion und das Zellwachstum auf der Probenoberfläche untersucht.

Die SLM-Parameterstudie zeigte, dass für die Herstellung massiver Proben eine minimale Volumenenergiedichte erforderlich ist. Entscheidend für die relative Dichte ist jedoch nicht nur die Volumenenergiedichte, sondern auch die spezifische Parameterkombination. Insbesondere die Laserscangeschwindigkeit spielt bei der Herstellung des BMGs eine entscheidende Rolle. Es wurde festgestellt, dass diese einen großen Einfluss auf die resultierende Mikrostruktur hat und die strukturelle Relaxation, die Glasübergangstemperatur und den Elastizitätsmodul der Probe bestimmt. 4-Punkt-Biegeversuche zeigten, dass die erzeugten Proben ausreichende Biegefestigkeiten und Elastizitäten aufweisen. Dennoch zeigten die Untersuchungen, dass die Eigenschaften des BMGs stark von der Bau- und Prüfrichtung abhängen. Darüber hinaus wurde festgestellt, dass eine Strahlbehandlung mit Glasperlen oder Korund vorteilhaft ist, um höhere Biegefestigkeiten zu erreichen. Allerdings sind nur die mit Glasperlen gestrahlten Proben zweifellos biokompatibel. Die mit Korund behandelten Proben sind zytotoxisch. Auch wenn eine Wärmebehandlung unterhalb der Glasübergangstemperatur die Lebensfähigkeit der Zellen verbessert, beeinträchtigt diese die mechanische Leistungsfähigkeit des BMGs. Darüber hinaus haben die Untersuchungen gezeigt, dass kristallisierte Proben hinsichtlich ihrer Herstellbarkeit und Verwendbarkeit ungeeignet sind.

# Content

1. Introduction .....	6
2. Theoretical Background .....	7
2.1. Metallic Glasses .....	7
2.1.1. Concept of Glass Formation .....	9
2.1.2. Thermal Stability of Bulk Metallic Glasses .....	11
2.1.3. Properties of Bulk Metallic Glasses .....	12
2.1.4. Processing of Bulk Metallic Glasses .....	14
2.2. Additive Manufacturing (AM) .....	15
2.2.1. Selective Laser Melting (SLM) .....	16
2.2.2. Process Parameters and Issues concerning the SLM Process .....	17
2.3. Selective Laser Melting of Bulk Metallic Glasses for Medical Applications .....	20
2.3.1. Challenges faced with Selective Laser Melting of Bulk Metallic Glasses .....	21
3. Materials and Experiments .....	23
3.1. Powder and Powder Characterisation .....	23
3.2. Selective Laser Melting .....	23
3.3. Characterisation of the Bulk Samples .....	25
3.4. Post Processing .....	28
3.4.1. Heat Treatment .....	28
3.4.2. Surface Treatment .....	28
3.5. 4-Point Bending Tests .....	29
3.6. Cytotoxicity, Cell Adhesion and Cell Growth .....	31
4. Results and Discussion .....	33
4.1. Powder Characterisation .....	33
4.2. SLM Parameter Study .....	36
4.2.1. Relative Density and Microstructure Analysis .....	36
4.2.2. XRD Measurements .....	43
4.2.3. DSC Measurements .....	44
4.2.4. Indentation Tests and Vickers Hardness .....	48
4.3. Building of Tensile Test Samples .....	52
4.4. Influence of a Post Processing .....	54

4.4.1.	Influence of a Heat Treatment .....	54
4.4.2.	Influence of a Surface Treatment .....	57
4.5.	4-Point Bending Tests .....	63
4.6.	Cytotoxicity, Cell Adhesion and Cell Growth .....	72
5.	Conclusions .....	75
6.	References .....	77
7.	Appendix.....	83
7.1.	Building Jobs – SLM Parameter Study.....	83
7.1.1.	Layer Thickness $ts_1 = 0.05$ mm .....	83
7.1.2.	Layer Thickness $ts_2 = 0.02$ mm .....	85
7.2.	Relative Density - LOM Micrographs.....	86
7.2.1.	Layer Thickness $ts_1 = 0.05$ mm .....	86
7.2.2.	Layer Thickness $ts_2 = 0.02$ mm .....	91
1.1.	Relative Density - Further Density Contour Maps .....	94
1.2.	XRD Pattern of Samples of the Parameter Study .....	94
1.2.1.	Layer Thickness $ts_1 = 0.05$ mm .....	94
1.2.2.	Layer Thickness $ts_2 = 0.02$ mm .....	95
1.3.	Further DSC Plots of Samples of the Parameter Study.....	96
1.4.	Tensile Test Samples' chosen Geometry.....	97
1.5.	4-Point Bending Tests – Samples' Dimensions and Results .....	97
1.5.1.	1 <sup>st</sup> Test Series – vertically built Samples, different Surface Treatment.....	97
1.5.2.	2 <sup>nd</sup> Test Series – vertically built Samples, different Heat Treatment.....	98
1.5.3.	3 <sup>rd</sup> Test Series – horizontally built Samples, different Test Orientation .....	98

# 1. Introduction

Due to the outstanding mechanical and chemical properties of bulk metallic glasses (BMGs), a lot of research and development have been carried out in this area for the last three decades. BMGs are a relatively new material class, which consists of at least three metallic elements. Contrary to metals in their traditional sense, BMGs are frozen-in metal melts with an amorphous microstructure. Thus their properties differ from those of classical metals with a crystalline microstructure. While exhibiting near-theoretical strength, they also show a large elasticity and low Young's moduli. Furthermore, they are wear- and corrosion-resistant, due to the lack of crystal defects like dislocations and grain boundaries [1, 2]. Due to these properties, biocompatible BMGs, such as Zr-based and Ti-based BMGs, have become possible future materials for medical applications. Surgical instruments, implants and scaffolds are examples for potential products.

To produce BMG components methods, such as casting and thermoplastic forming, can be used. However, there are some limitations regarding these techniques. Both are insufficient to fabricate hollow, complex shaped, and large-scale parts. Therefore, selective laser melting (SLM), an additive manufacturing method, represents a potential opportunity for this purpose. Thereby, three-dimensional (3D) metallic parts can be built layer upon layer according to computer aided design (CAD) data. Due to the layer-wise building, the high cooling rates, which are necessary to obtain the amorphous microstructure and thus the outstanding properties of the BMG, can be achieved. Moreover, an enormous design-freedom exists, which is beneficial for the fabrication of personalized implants. Nonetheless, because of many factors affecting the SLM process and consequently the resulting part, challenges have to be mastered in the case of using the additive manufacturing processing route for BMG components.

The aim of this thesis is to find appropriate process parameters in order to fabricate fully dense Zr-based BMG samples, which exhibit an amorphous microstructure. Therefore, a parameter study is carried out, whereby the main process parameters are varied. The prepared samples are then investigated by different methods, such as light optical microscopy, X-ray diffraction, differential scanning calorimetry, and (micro-) hardness measurements. Further samples for mechanical and biocompatibility tests are produced with a selected parameter set by which a dense and amorphous sample will be obtained. In addition, the influence of heat and surface treatments on the samples properties will be analysed.

## 2. Theoretical Background

In the following chapter, the theoretical background and some fundamental knowledge on (bulk) metallic glasses and the additive manufacturing process, selective laser melting, are presented. First, the material class of bulk metallic glasses are discussed both generally regarding to their glass formation, properties, and processing possibilities. Furthermore, some information on selective laser melting is given. This includes the working principle, relevant process parameters and other issues which concern the processing technique. In the end, some comments regarding to the manufacturing of bulk metallic glasses for medical applications are made, whereby the challenges faced during the processing are also offered to the reader.

### 2.1. Metallic Glasses

Typically metals and their alloys are considered as solid materials with a crystalline structure. In the solid state the constituent atoms of the material are highly ordered in three dimensions and occupy specific places in a periodic way. This corresponds to a low-energy state that is adopted from the material after solidification under equilibrium conditions, viz. cooling the melt with low cooling rates. In contrast to that, the atoms in metallic glasses do not exhibit a defined long-range order, so that they are described as non-crystalline, amorphous or also glassy solids (Figure 1a). Because of the metallic glasses' amorphous structure, they show their unique properties such as near-theoretical strength, low Young's modulus, large elasticity, and high corrosion and wear resistance [1, 3].

In order to obtain the disordered atomic structure of metallic glasses, the metal melt has to be cooled fast enough to suppress the metal's crystallization, i.e. the cooling rate curve should not intersect the crystalline 'nose' in a continuous cooling transformation (CCT) diagram. In Figure 1b, a schematic CCT diagram for a metallic glass shows different cooling rate curves. The curve with the lowest cooling rate,  $R_{\text{cryst}}$ , intersects the crystalline 'nose': as a result the melt undergoes crystallization and a solid with a crystalline structure is formed. However, if the cooling rate is higher than a critical cooling rate,  $R_c$ , glass formation occurs [1]. In other words, a metallic glass is a frozen-in metal melt [4].

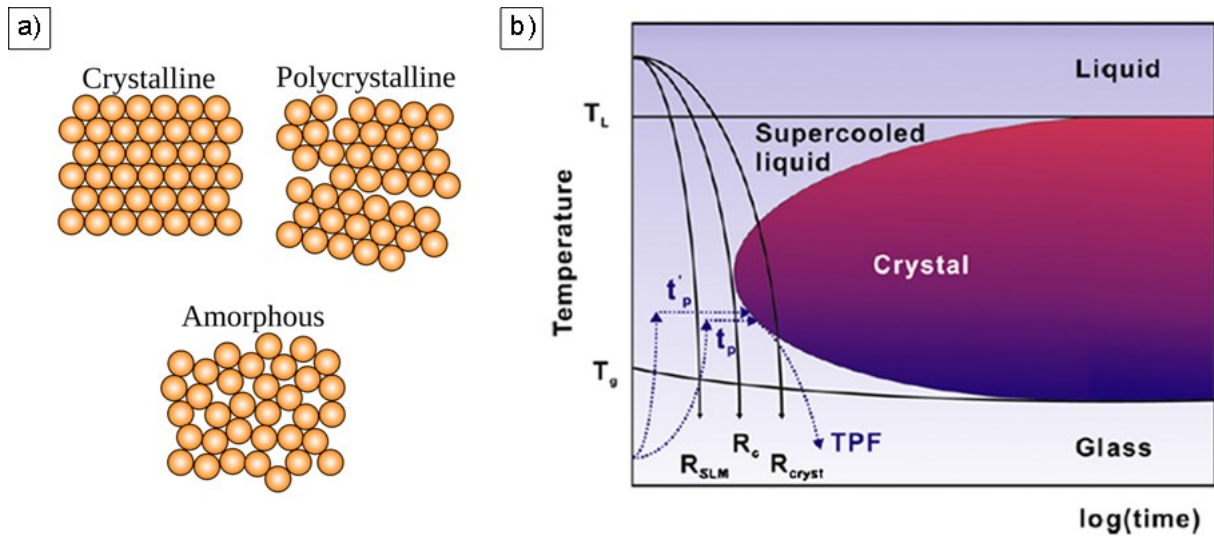


Figure 1: a) Illustration of different arrangement of atoms occurring in solid materials [5]. b) Schematic CCT diagram for a metallic glass. Glass formation only takes place, if the applied cooling rate is higher than the critical cooling rate  $R_c$ . A cooling rate achieved by Selective Laser Melting,  $R_{SLM}$ , and a temperature profile used for Thermoplastic Forming (TPF) are shown in the figure as well [1].

In 1960, Pol Duwez et al. at the California Institute of Technology in Pasadena, California, observed this phenomenon for the first time by quenching a molten Au-25.at% Si alloy from 1300°C to room temperature [6]. The cooling rate of a million degrees per seconds ( $10^6$  K/s), achieved by the gun technique of liquid quenching, prevents an ordering of the atoms and a non-crystalline structure was obtained in the solidified alloy. Scientists' suspicions about the possibility of producing amorphous structures in metals and alloys by rapid quenching the melt was confirmed over the course of the following years and further metallic glasses were developed [3].

Nonetheless, in these early days of metallic glasses, the samples' geometry of metallic glasses was restricted to thin ribbons, foils and powders in order to achieve the high cooling rate. This geometrical restriction made it difficult to find wider application for metallic glasses [7, 8]. However, successive research in terms of the understanding of vitrification and development of various processing techniques enabled a production of 'bulk' metallic glasses (BMGs), which exhibit a section thickness or diameter of a few millimetres to a few centimetres. Nowadays, a large number of different glass forming alloys, mostly consisting of at least three elements, are known [1, 8, 9].

### 2.1.1. Concept of Glass Formation

As mentioned above, a metallic glass is a frozen-in metal melt. In Figure 2a, the dependence of the specific volume of a metal on the temperature is shown. There are two different solidification routes, depending on whether the metal is a glass forming one or not. When cooling down the metallic melt (liquid), its volume decreases in both cases. When going below the melting/freezing point,  $T_m$ , a metastable undercooled liquid (or supercooled liquid (SCL), if the liquid state can be maintained well below the freezing point, without any solidification), is formed. In the case of the classical metal, nucleation and crystallisation takes place at a certain undercooling  $\Delta T$ . Due to the rearrangement of the atoms into a stable and ordered configuration shrinkage occurs. This is evident in the strong reduction of the specific volume at the melting point or rather a few degrees below. However, the solidification of glass forming metals follows the second route. Instead of crystallisation, the metal melts can be significantly undercooled. This can, for example, be achieved for example due to the imposition of a high cooling rate. While decreasing the temperature, the volume of the undercooled liquid is reduced and its viscosity increases (Figure 2c). Well below the freezing point, the viscosity is so high that the amorphous metallic melt is frozen-in. For all practical purpose, this resembles a solid and is referred to as (metallic) glass. The temperature at which the undercooled/supercooled liquid becomes a solid glass is the glass transition temperature,  $T_g$ . In reality, however, this is rather a temperature interval in which the metal melt vitrifies. Additionally, the glass transition temperature depends on the history of the glass, i.e. at which cooling rate the glass was prepared. Low cooling rates (but higher rates than the critical one) result in lower glass transition temperatures, and higher ones shift the  $T_g$  to higher temperatures (Figure 2a). Hence, the glass transition temperature is a kinetic parameter, which underlines the kinetic nature of the vitrification phenomenon. However, not only the glass transition temperature is determined by the cooling rate, but the frozen-in structural state and consequently the properties of the glass are also determined by it [3, 4].

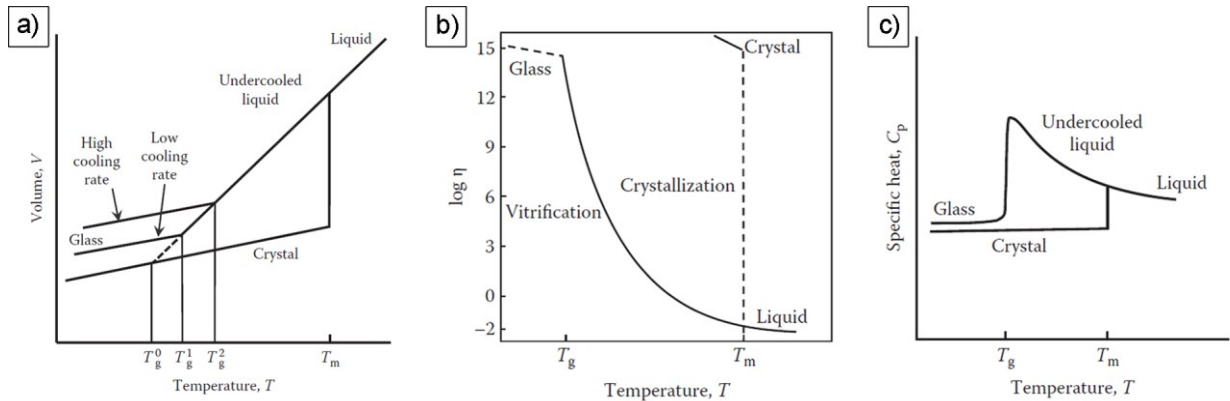


Figure 2: Dependence of a) the specific volume b) the viscosity and c) the specific heat on the temperature for a classical metal and a glass-forming one [3].

Whether a metallic alloy can be transformed into the glassy state or not is dependent on the cooling rate on the one hand. On the other hand, the alloy should show a high glass-forming ability (GFA), which includes slow crystallisation kinetics and/or a slowdown of structural relaxation in order to prevent atomic rearrangements while cooling down the alloy [1]. Especially for BMGs, there are some key empirical criteria to meet the requirements for a high GFA [2, 3]:

- multicomponent alloy, which contains three or more elements
  - reduction of the energetic advantage of forming an ordered structure due to increased complexity and size of the crystal unit cell
- atomic radius mismatch between the constituent elements greater than 12%
  - efficient packing with less free volume of clusters in the liquid, thus increased liquid-solid interfacial energy and decreased atomic diffusivity
- negative heat of mixing between the main elements
  - increases energy barrier at liquid-solid interface, decreased atomic diffusivity, retards atomic rearrangements and the nucleation rate of crystals, extension of the temperature range of the SCL
- using a composition close to a deep temperature eutectic
  - formation of a stable liquid at low temperatures

Since these criteria contribute to the shift of the crystallisation field in the CCT diagram to larger times, the critical cooling rate could be reduced for the alloys and consequently the fabrication of BMGs was facilitated. Typical critical cooling rates for BMGs are between  $10^2$  and  $10^6$  K/s [1, 2]. However there are also compositions which have critical cooling rates lower than 100 K/s [7].



### 2.1.2. Thermal Stability of Bulk Metallic Glasses

Due to the solidified amorphous structure, a metallic glass is not in a thermodynamically stable (equilibrium) state and a driving force toward the equilibrium (crystalline) state exists. Depending on the temperature and the provided time, the glass can relax and eventually crystallise. The temperature at which crystallisation takes place is the crystallization temperature,  $T_x$ . It represents an upper limit for applications, since a metallic glasses loses its amorphous microstructure and consequently its unique properties. However, the crystallisation temperature of a metallic glasses is, similar to the glass transition temperature, dependent on the heating rate. A higher heating rate results in a higher crystallisation temperature. In contrast to that, crystallisation can also take place at temperatures lower than  $T_x$ , if sufficient time is provided [3].

The thermodynamic behaviour of BMGs is usually determined by means of a differential scanning calorimeter (DSC) or a differential thermal analyser (DTA) during continuous heating of the glassy alloy at a constant heating rate. Thereby, the glass transition temperature,  $T_g$ , the crystallisation temperature,  $T_x$ , and the melting temperatures can be investigated. In Figure 3a, a schematic DSC plot of an as-quenched BMG is depicted. Therein, the three characteristic temperatures are visible. Until  $T_g$ , the BMG maintains the glassy structure. However, it undergoes structural relaxation since it is not in configurational equilibrium. During the heating below  $T_g$ , the as-quenched glass slowly transforms into a lower energy state, which means that an annihilation of free volume takes place and an 'ideal' glass is formed. Especially a metallic glasses produced with higher cooling rates exhibit a frozen-in structure with a large amount of free volume. Thus, the atomic diffusivity is high in the glass and pronounced structural relaxation can occur [3]. In Figure 3b, the event of structural relaxation can clearly be seen in the DSC plot. The grey-dashed area corresponds to the enthalpy, which is released while the structural relaxation took place [4]. Due to the structural relaxation and annihilation of free volume the BMGs physical properties change. Examples are decreased specific heat, reduced diffusivity, increased elastic constants (by about 7%), significantly increased viscosity (by more than five orders of magnitude), and loss of (bend) ductility in some cases. Furthermore, the BMGs' density slightly increases by 0.1% - 0.15% due to the rearrangement of the atoms [3].

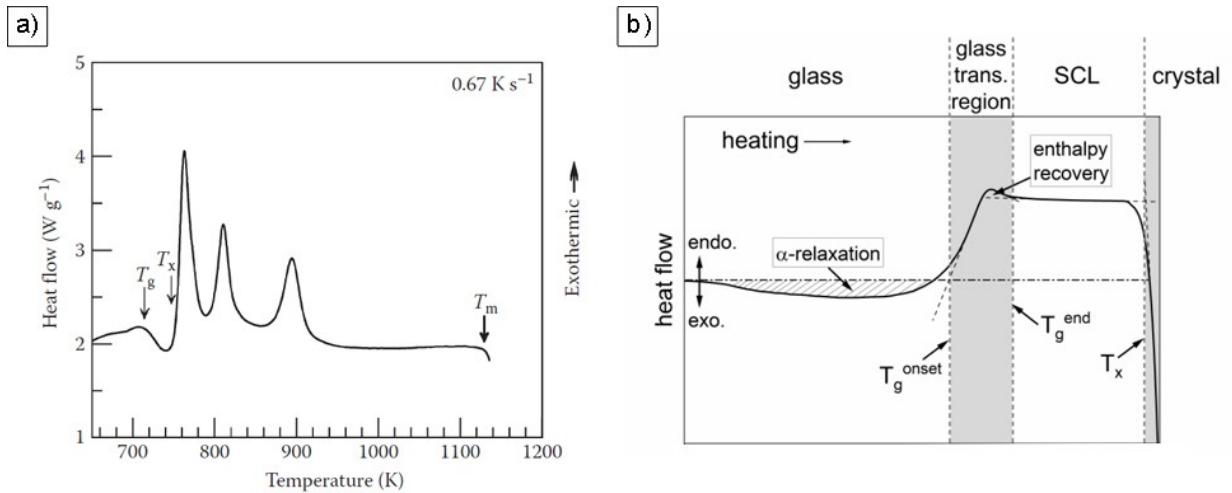


Figure 3: a) Schematic DSC plot of a bulk metallic glass [3]. b) Schematic DSC plot of a metallic glass, where pronounced structural relaxation takes place below the glass transition temperature [4].

After the glass transition, defined by the onset and end temperature, the supercooled liquid (SLC) is formed. By further increasing the temperature, the crystallisation of the BMG occurs. The crystallisation is clearly discernible by significant exothermic peaks. Using the resulting DSC plot, the crystallisation onset temperature,  $T_{x,on}$ , the peak temperature,  $T_p$ , and the enthalpy of crystallisation,  $\Delta H_x$ , can be defined. The endothermic transformation at high temperatures corresponds to the melting of the alloy. Since most BMGs are alloys, they exhibit a range of melting temperatures starting at the solidus temperature and ending at the liquidus temperature [3, 4].

### 2.1.3. Properties of Bulk Metallic Glasses

Even if BMGs appear to be conventional metals – gray, opaque, and shiny [2], they behave differently: compared to their crystalline counterparts, BMGs' yield strengths are higher (up to 5 GPa for a Cobalt-based BMG [10] and 2 GPa for Zr-based glasses [11]) and are approaching the theoretical strength limit. Additionally, they exhibit an extremely high elastic limit (about 2 - 3% [7]), and the BMGs' Young's moduli are considerably lower compared to crystalline materials. Related to the high yield strength, the hardness of BMGs are high as well (up to 1100 HV for Fe-based BMG) [4]. Therefore, the wear resistance of the alloys is superb. In Figure 4a, a comparison of the strength and hardness values of various BMGs to the values of some crystalline materials is shown.

The origin of the unique mechanical properties of the BMGs is thought to be a result of the lack of the long range order (periodicity) of the constituent atoms [1, 4, 8]. Due to the amorphous structure, plastic deformation via dislocations is unfeasible. Consequently, another deformation mechanism takes place, which explains the outstanding mechanical properties of the BMGs. At temperatures well below the  $T_g$ , the plastic deformation process in BMGs is an inhomogeneous one and takes place in a highly concentrated manner in thin shear bands. It is suggested that during the deformation the viscosity of the metallic glass in the shear bands is decreasing. This can happen either due to the formation of free volume or adiabatic heating. As a result, the applied stress can be accommodated therein. The vein-like patterns typically observed at the BMGs' fracture surfaces give an indication that a reduction of viscosity takes place (Figure 4b). The inhomogeneous deformation combined with the tightly packed glassy structure makes the metallic glass unstable at very high stresses and finally it fails catastrophically [3, 4, 8].

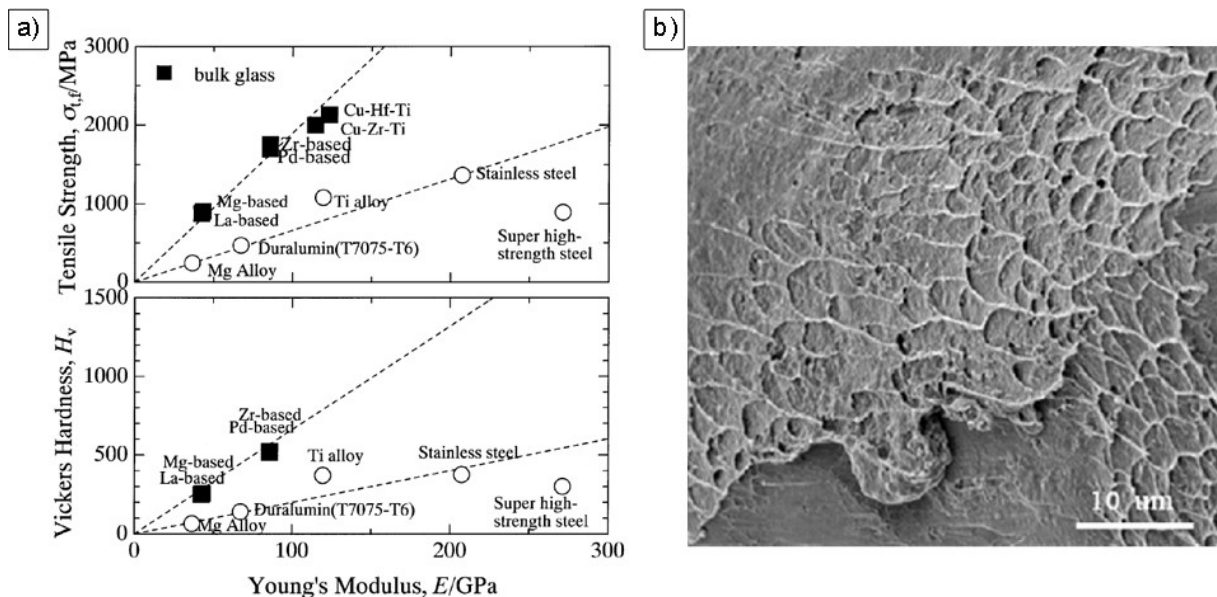


Figure 4: a) Mechanical properties (tensile strength, Vickers hardness and Young's moduli) of BMGs (■) and crystalline materials (○) [12], b) vein-like pattern observed at the fracture surface of a Zr-based BMG [13].

For a safe use, it is important to fully characterise the BMG regarding their physical, mechanical, and chemical properties. Especially the corrosion behaviour becomes crucial when BMGs are used in aggressive and hostile environments such as high temperatures, oxidizing atmospheres and corrosive media. However, for biomedical applications the behaviour of the material in physiological solutions or environment is extremely relevant as well in order to avoid dangerous consequences (infections, injuries, intoxications). Compared to crystalline alloys with similar composition, BMGs show a higher corrosion resistance. This is unexpected, since they are in a high-energy

state. However, the absence of crystal defects (grain boundaries, dislocation, precipitations) and the chemical homogeneity is beneficial in the respect to their chemical stability. Furthermore, metallic glasses based on zirconium form stable oxide layers, which reduce the release of alloy elements and therefore increase the biocompatibility. Thus, surgical instruments and implants made out of BMG can utilise the special combination of chemical and mechanical properties [3, 7, 14].

Resulting from the disordered structure and the presence of free volume, the density of the BMGs are lower than their crystalline counterparts. Metallic glasses and BMG alloys are mostly measured by means of the Archimedean principle, which is a gravimetric determination of the density. When the amorphous alloy is heat-treated, the density increases due to the ordering of the atoms and annihilation of the free volume. Slow heat conduction and a high electrical resistivity (about two orders of magnitude higher compared to their crystalline counterparts) results from the disordered arrangement of the atoms as well. However, some Fe-based and Co-based alloys benefit from this absence of crystalline grains. They are outstanding soft-magnetic materials with low coercivity and low remanence, which can find application in the electronics industry [1–3, 15].

### **2.1.4. Processing of Bulk Metallic Glasses**

Due to the need of rapid solidification to obtain the glassy structure and consequently the outstanding properties of the BMG, the processing method has to be chosen accordingly. Casting is the commonly used technique; however, thermoplastic forming (TPF) is also a possible fabrication route [1]. Although casting has a lot of advantages, such as reduced tool costs, low energy consumption, one step process [16], the capability to produce more complex shaped geometries is insufficient. With casting only simple shaped parts, for instance rods and plates, can be fabricated. Furthermore, it has to be considered that the material of the casting mold has a high thermal conductivity and large heat capacity on the one hand [1]. Therefore, a popular manufacturing process is copper mold casting [3]. On the other hand, when the section thickness of the BMG part increases, the cooling rate decreases and a BMG alloy with a high GFA has to be used in order to obtain a larger fully glassy part. Consequently, it can be concluded that either a good glass former is necessary or the parts section thickness is restricted to a maximum of about 1 mm [1, 3, 17].

If more complex parts are required, there is the possibility to apply the thermoplastic forming (TPF) process to the BMG alloy. This process is similar to the one used for shaping polymers (thermoplastics) or silicate glasses. In Figure 1, the used temperature profile for TPF is depicted. The BMG alloy is heated to temperatures

between  $T_g$  and  $T_x$  (supercooled liquid), and due to its drastic decrease in viscosity the material can be shaped relatively easy. It is necessary that the forming is completed before crystallization starts. Therefore, the process requires both a low viscosity and a long processing time is required. A long processing time can either be achieved by increasing the GFA of the BMG or by shortening the heating time (temperature profile  $t_p$ ). Although the thermoplastic forming enables the production of BMGs with near-net shape finish and extremely smooth surfaces, it is difficult or even impossible to produce complex hollow and/or large-scale structures [1, 4, 16].

Since both the casting and thermoplastic forming entail many limitations for the fabrication of complicated BMG parts with greater dimensions, it is necessary to evolve and study alternative processing methods. A promising technique is selective laser melting (SLM), an additive manufacturing method, wherewith complexly shaped three-dimensional parts can be directly fabricated.

### **2.2. Additive Manufacturing (AM)**

Additive Manufacturing, also known as Rapid Prototyping (RP), is a broad term referring to production processes evolved over the last decades. According to the American Society for Testing and Materials (ASTM), AM is “a process of joining materials to make objects from 3D model data, usually layer upon layer, as opposed to subtractive manufacturing and formative manufacturing methodologies” [18]. In the AM process, a formless raw material, such as liquid, powder, suspension, filament, or sheet is selectively joined. Therefore, AM enables a great design freedom. High individuality and variance in the production of the parts is given as well. Moreover, the AM process is efficient regarding material resources. A high material utilization can be achieved since material is only joined where needed. Depending on the specific AM technique, excessive material can be reconditioned and reused. Furthermore, a great advantage of the near-net-shape production is that only little or no post processing is necessary afterwards. This enables the manufacturing of parts which are challenging to machine or to produce with other techniques. Further advantages of AM are its cost-efficient usability for small batches and that the manufacturing time of the parts can be kept relatively short. Therefore, AM has become a revolutionary technology in various industrial sectors such as automotive, aerospace, consumer products and medical/dental applications [19, 20].

Due to the growing demand in the various sectors, different AM methods were developed within the last years. In this thesis, Selective Laser Melting (SLM), a powder

bed fusion process, is utilized and will be described over the following pages. Detailed information on other techniques can be found in [21].

### 2.2.1. Selective Laser Melting (SLM)

SLM is a widely used AM method to produce fully dense metallic parts with properties comparable to those of bulk materials produced with conventional manufacturing technologies [22, 23]. Since the method falls in the category of powder bed fusion processes, metallic materials in the form of powder are used as a raw material. During the process, a high intensity laser, mainly fiber lasers and/or Nd:YAG lasers [24], is used as an energy source to build the part according to the computer aided design (CAD) data. In Figure 6, a schematic illustration of the SLM process chain is shown. The main process steps are as follows [23, 25]:

- Preparation of the parts' CAD data, which includes the conversion of the CAD model to a STL (stereolithography, known as the primarily developed AM technique) file and its being sliced into cross-sectional layers. Typically used layer thicknesses vary between 20  $\mu\text{m}$  and 100  $\mu\text{m}$ .
- Layer-by-layer construction of the part:
  - When the building chamber is filled with the protective inert gas in order to reduce the oxygen content, the recoater distributes powder in the defined layer thickness from the reservoir onto the building platform.
  - The high intensity laser scans the powder bed along specific traces, the so-called scanning strategy, defined by the slices of the 3D CAD data. Thereby, selected areas of powder are molten and solidification of the resulting melt pools takes place. Thus, the loosely powder particles are fused together. Since the heat is conducted to areas adjacent to the melt pool, a connection to the material below can be established as well.
  - Once the selective exposure of the layer is completed, the building platform is lowered by the set layer thickness. In contrast, the powder reservoir is raised. Again, new powder is distributed onto the building platform and the laser selectively fuses the newly applied powder particles together.
  - These main steps are repeated until a solid three-dimensional part is built. After cooling down, the part can be taken out of the building chamber.
- Eventually, a post processing of the part, is necessary. This can be the removing of the parts' support structure, a surface treatment or a heat treatment.

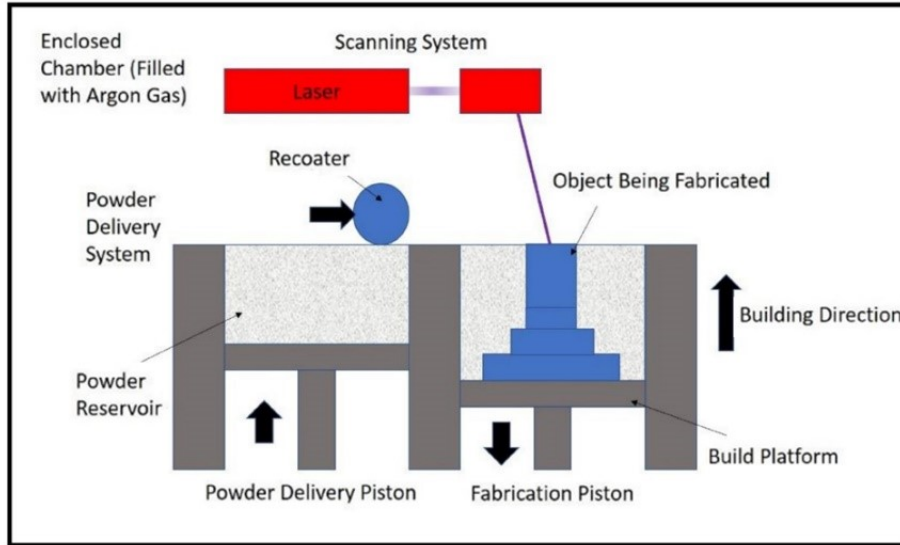


Figure 5: Schematic illustration of a selective laser melting (SLM) building chamber [22].

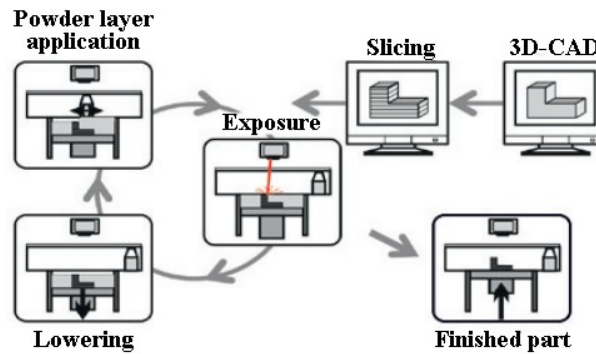


Figure 6: Process chain of the SLM process [26].

### 2.2.2. Process Parameters and Issues concerning the SLM Process

Since a fundamental objective in the production of components by SLM is the achievement of high-density parts and the fulfilment of their desired properties, an understanding of the numerous interrelating parameters determining the SLM process is important. Besides some parameters that not being able to be varied and thereby being defined by the SLM machine (laser wave length, spot size of the laser) or fixed by the used material (viscosity, heat conductivity), there are adjustable manufacturing parameters. The volume energy density,  $E$  ( $\text{J}/\text{mm}^3$ ), which is applied to the powder during the SLM process, is given by:

$$E = \frac{P}{v * h * ts}, \quad (1)$$

where  $P$  is the laser power,  $v$  is the scanning velocity,  $h$  is the scan spacing or hatching, and  $t_s$  is the layer thickness. Figure 7a schematically depicts these parameters. Since a minimum critical energy density is essential to exceed the melting temperature of the material and to produce high density parts with desired properties, these parameters have to be optimised [27]. However, Equation (1) does not take into account other important factors such as the laser offsets at the corners, the laser diameter and its offset at the surface of the melt, and the direction of building and the protective gas flow [28]. Furthermore, the scanning strategy is not considered in the equation either. As already mentioned, it is the pattern of defined traces, which the laser follows during the exposure of a layer. Different patterns, which consist of individual vectors, can be seen in Figure 7b. The vectors can be arranged in a unidirectional or bidirectional way, but also as an island scanning (inter-layer), where the vectors are rotated from section to section. Additionally, the pattern can be rotated between superposed layers by a specific rotation angle. It is known that the quality of the SLM-fabricated part produced is influenced by the design of the scanning strategy [27, 29, 30].

SLM is a complex metallurgical process [27], where metallic powder is selectively molten and fused together. By varying the in Equation (1) mentioned process parameters, the energy input into the powder and consequently the amount of melting can be modified. Due to that, relatively small melt pools, which are in the order of 100  $\mu\text{m}$ , can be generated. This allows a rapid heat extraction and therefore local solidification rates in the order of  $10^3 - 10^5$  K/s can be realized. Therefore, it is possible to produce complex components by SLM, which exhibit a specific microstructures and consequently tailored properties. In particular, the fast cooling can inhibit the formation of thermodynamically stable phases and promotes the metastable ones instead. Hence, SLM facilitates the vitrification and allows the fabrication of glassy metallic components using glass-forming powders as a raw material [1, 31]. In Figure 1, the cooling rate,  $R_{\text{SLM}}$ , illustrates this possibility.



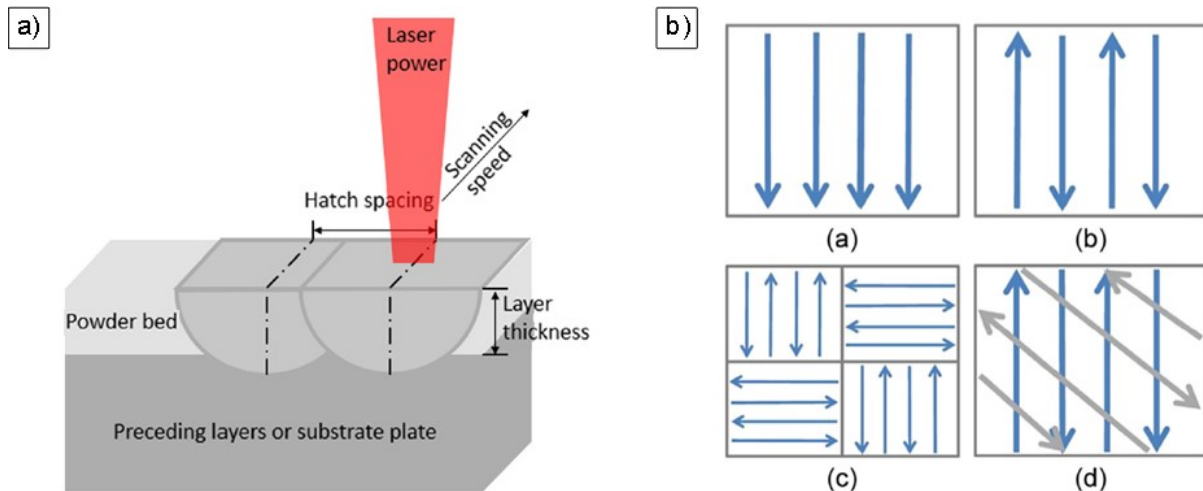


Figure 7: a) Manufacturing parameters of SLM, which can be adjusted: laser power, scanning velocity, hatching, and layer thickness [32] b) different scanning strategies within one layer [27].

The density, microstructure, and resulting properties of the SLM-fabricated parts solely by the parameters related to the laser and the scanning. As a starting material, the powder, its properties and characteristics play a crucial role as well. For example, the powder's morphology (shape and size of the powder particles) can determine the flow properties and the particles' packing when a layer of powder is applied on the building platform. This in turn influences the resulting density and quality of the SLM-produced part. For the SLM process, spherical powder particles with a high packing density are beneficial. In addition, a narrow particle size distribution of the powder is necessary to produce high quality parts by SLM. Here it has to be mentioned that the layer thickness of the part should be chosen according to the powder's morphology. Dependent on the particle size distribution and the mean diameter characterised by  $D_{10}$ ,  $D_{50}$ , and  $D_{90}$  a thicker or rather thinner value of the layer thickness is reasonable [25, 27, 32].

However, another issue, which is highly connected to the process parameters, is the overall poor surface quality of the SLM-fabricated part. Due to the layer-wise nature of the process, the chosen layer thickness strongly influences the surface roughness; a larger layer thickness also increases the surface roughness. However, other process parameters and their combination have an great impact on the surface quality as well [33]. The occurrence of porosities, adherent powder particles, balling associated glitches, ripple patterns and other defects are determined by all the interrelated parameters and therefore are a result of the introduced energy density [34]. It has to be noted that this poor surface quality demands a subsequent surface treatment, which can be long and expensive, to meet the given requirements, regarding to mechanical, chemical, and physical properties of the metallic part.

Furthermore, materials manufactured by SLM exhibit an anisotropy and heterogeneity mainly determined by the building direction. DebRoy et al. [19] and Kok et al. [35] found that the anisotropic behaviour for crystalline materials is influenced by following factors: grain morphology, crystallographic texture, lack-of-fusion defects, phase transformation, heterogeneous recrystallization, layer banding and microstructural coarsening. The microstructural anisotropy determines the mechanical properties of the materials and thereby, the mechanical properties are dependent on the building direction of the part [36].

### **2.3. Selective Laser Melting of Bulk Metallic Glasses for Medical Applications**

Additive manufacturing and the SLM method has become a more and more established technology for the production of medical products such as orthopaedic implants and scaffolds. Due to the capability of SLM to build complex geometries and functional metallic parts directly in a single step, it is possible to create personalized parts with improved matching of mechanical properties and enhanced osteo-integration. This has the potential to reduce surgery, rehabilitation and recovery times, improve implant fixation and reduce the likelihood of revision surgery [37]. Thus, the patient's well-being can be increased, while costs, through shorter operating time and patient care, are reduced.

Currently used metallic implants are manufactured out of conventional medical materials such as stainless steels, Co-based and Ti-based alloys. Despite their continuously improved performance, they are still deficient regarding their bio/mechano-compatibility (high modulus and lack of elasticity), corrosion resistance, and fatigue behaviour. However, bulk metallic glasses (BMGs) can fulfil the required material properties and thus become potential materials for non-absorbable medical applications. Their extremely high fracture strength, relatively low elastic modulus, and high strain to fracture, are extremely beneficial for the application as orthopaedic implants and scaffolds. In Figure 8, a comparison of the yield strength and young's modulus of BMGs from literature [38] to the values of stainless steel, Co–Cr and Ti-based alloys and the cortical bone is shown. Therein, the mechanical properties of the Zr-based BMG used in this thesis is marked as well. Due to the relatively low modulus of the BMG, the mismatch between the human bone and the implant is smaller. Therefore, the adverse effect of “stress shielding”, which results in slower bone healing, bone resorption and the potential to lose the implant, can be prevented, when using the BMG as an implant material. At the same time, the high yield strength of the material ensures a good resistance against loading so that the patient has less

limitation in daily life after the surgery. Furthermore, BMGs exhibit good corrosion properties in physiological solutions, and in contrast to common metallic biomaterials, they show better cell growth and attachment support. Moreover, stable oxide layers formed on the BMG increases the biocompatibility [39–41].

Due to the potential of BMGs for application in the medical field, their development has been expedited in the past decades. Nonetheless, the processing of complexly shaped, three-dimensional BMG components is challenging, since restrictions in scalability and flexibility exist when using conventional manufacturing routes. Therefore, the SLM process is an attractive method to fabricate personalised medical implants with outstanding properties [39].

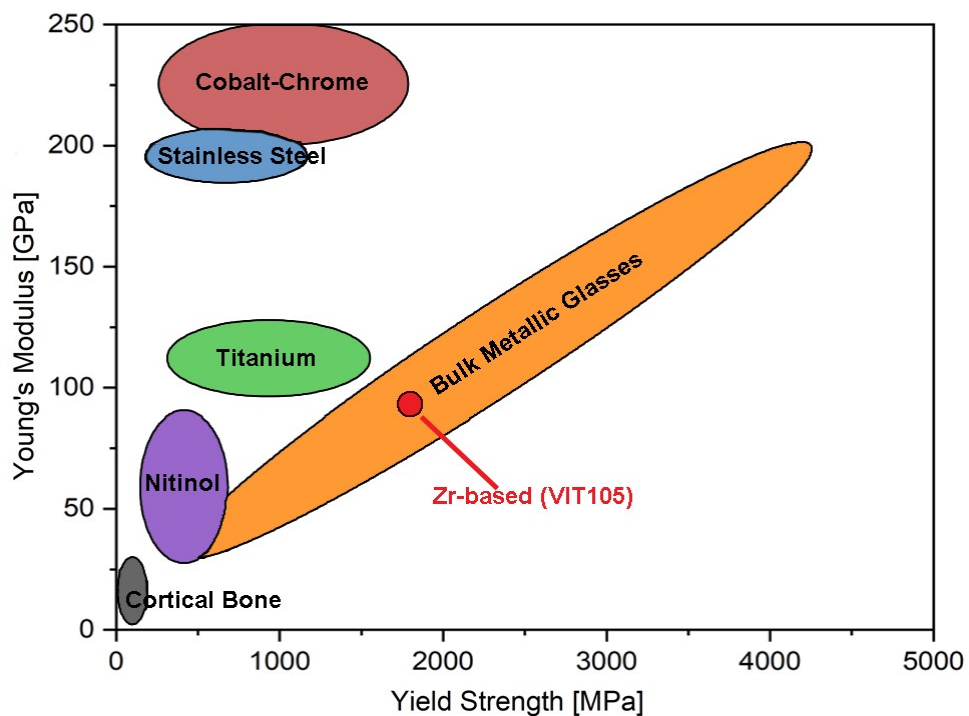


Figure 8: Comparison of mechanical properties of BMGs, stainless steel, Cobalt–Chrome, Ti-based alloys, and the cortical bone; redrawn from [41]. The values of the Zr-based BMG (VIT105) [11] used in this thesis are marked as well .

### 2.3.1. Challenges faced with Selective Laser Melting of Bulk Metallic Glasses

Although SLM provides the possibility to produce bulk metallic glasses, there are still challenges to overcome. First of all, appropriate process parameters have to be found in order to obtain a dense part. Due to the many influencing and interrelated parameters, which were discussed in section 2.2.2, a parameter study, where various combinations of the process parameters are executed, is necessary. When searching for process parameters for the BMG, it is crucial to consider the resulting

microstructure. The amorphous nature of the SLM-fabricated samples should be ensured so that the advantageous properties of the BMG are not negatively impacted. For the Zr-based BMG, which was used in this thesis, some investigations were already done in other research groups [29, 30]. It was found that higher laser energy densities lead to partial crystallisation during the process. Pauly et al. [29] defined a critical energy density of  $E_{\text{crit}} = 15 \text{ J/mm}^3$  for the BMG alloy. However, since the densification plays an important role as well, they found out that there is a process window between 12 and 15  $\text{J/mm}^3$  in which highly dense and fully glassy SLM components can be produced. Li et al. [30] could also obtain amorphous samples, which only have a few pores with an energy density of  $13.3 \text{ J/mm}^3$ . Additionally, both research group emphasized the sensitivity of the alloy to the used scanning strategy with regards to the distribution of the pores and the chemical homogeneity of the material. Nonetheless, as some influencing parameters are different in the present work (machine, laser spot size, powder particle distribution, layer thickness...) these process parameters can only be a rough guide.

Furthermore, the BMG should be used in the medical field as implants or scaffolds. Therefore, the surface topography is essential. The biological response, which includes cell adhesion, spread, migration, proliferation, and differentiation of cells, is highly influenced by the surface quality of the SLM-fabricated part [42]. Due to the poor quality of the as-built part, a suitable surface treatment has to be found to fix the deficiencies (adherent powder particles, ripple pattern...) caused by the SLM process. Common surface treatments for SLM-fabricated parts are polishing, etching and media blasting due to their low costs, practicality and simplicity [43].

Besides the mentioned challenges, the resulting mechanical properties of the SLM-fabricated BMG are also important. As mentioned above, the layer-wise nature of the built part can result in anisotropic mechanical properties. However, since the BMG does not have a crystalline microstructure, anisotropies caused grains cannot arise. Nonetheless, appropriate process parameters, where a good connection between the individual layers, a good densification and a homogeneous elemental distribution within the BMG can be established, are necessary in order to obtain isotropic material properties.

## 3. Materials and Experiments

### 3.1. Powder and Powder Characterisation

In this thesis, gas-atomized Zr-based metallic glass powder (trade name VIT105) with a nominal composition of  $Zr_{65.5}Cu_{15.6}Ni_{11.8}Ti_{3.3}Al_{3.7}$  (in wt%, produced by Nanoval GmbH & Co. KG, Germany) was chosen. The specified particle size and the  $d_{50}$  value of the powder were below 100  $\mu m$  and 25.2  $\mu m$ , respectively. Particle size distribution of the supplied powder was determined by means of Dynamic Image Analysis in a CAMSIZER X2, carried out by the voestalpine BÖHLER Edelstahl GmbH & Co KG, Kapfenberg. In order to investigate the powder particles' morphology (shape, surface, size and microstructure) a Tescan Vega 3 scanning electron microscope (SEM) was used. The actual chemical composition was determined by energy-dispersive X-ray (EDX) measurements using the same SEM. Furthermore, X-Ray diffraction (XRD) and differential scanning calorimetry (DSC) measurements of the powder were carried out as described in Section 3.3.

### 3.2. Selective Laser Melting

All SLM samples were produced by a TruPrint1000 (TRUMPF, Figure 9a) powder bed fusion system equipped with a 200 W fiber laser, which has a spot size of 30  $\mu m$ . To ensure an inert atmosphere ( $O_2$  content < 100 vol.ppm) during the manufacturing, argon was used as a protective gas. As a building platform, a Ti-6Al-4V substrate with a diameter of 100 mm was chosen. SLM Parameter Studies were carried out with two different layer thicknesses, namely  $ts_1 = 0.05$  mm and  $ts_2 = 0.02$  mm. To find suitable parameters for a dense sample production the energy density was varied between 8 and 34  $J/mm^3$ . According to Equation (1), the laser power,  $P$ , varied between 80 W and 180 W for  $ts_1$  and between 40 W and 80 W for  $ts_2$ . The hatching,  $h$ , altered from 0.06 mm to 0.20 mm for  $ts_1$  and from 0.08 mm to 0.10 mm for  $ts_2$ . The scanning velocity,  $v$ , ranged from 800 mm/s to 3000 mm/s for both layer thicknesses. All combinations of the used parameters, the corresponding energy input,  $E$ , and the sample identifications can be found in the Appendix in Section 7.1. As a scanning strategy, a pattern of unidirectional vectors, which was rotated by  $67^\circ$  in superposed layers, was used. For the SLM parameter studies, cubes (1 cm x 1cm x 1 cm, (L x B x H)) with a 3 mm high block support structure were produced. Such a support structure enables a safe detaching of the cubes and should reduce chemical contamination due to the different material of the substrate. All samples were rotated between  $15^\circ$  and  $20^\circ$  around the z-axis (building direction) to ensure a stable recoating procedure. Photographs of the production of the cubes can be seen in Figure 9b-e.

From one selected parameter set, namely 08\_06 ( $E = 33.33 \text{ J/mm}^3$ ,  $P = 80 \text{ W}$ ,  $h = 0.10 \text{ mm}$ ,  $v = 1200 \text{ mm/s}$ ,  $ts2 = 0.02 \text{ mm}$ ), further cubic samples ( $1 \text{ cm} \times 1 \text{ cm} \times 1 \text{ cm}$ ), cylindrical samples, 4-point bending test samples ( $30 \text{ mm} \times 3 \text{ mm} \times 3 \text{ mm}$ ) and, hexagonal platelets ( $15 \text{ mm} \times 1 \text{ mm}$ , ( $R \times t$ )) for cytotoxicity tests were produced. For the cubes, the vertically built cylindrical samples and the vertically built platelets the same building strategy as in the SLM parameter study was used.

The cylindrical samples were built in two different constructive executions. On the one hand tensile test samples with a geometry based on ASTM E8 were fabricated. The used geometry is shown in the Appendix, Section.1.4. Samples with a uniform diameter of 6 mm were built on the other hand. The samples were built in vertical direction as shown for the 4-point bending test samples in Figure 11b. The height of the samples were for both variants  $H = 85 \text{ mm}$ .

The 4-point bending test samples were produced in both horizontal ( $L_s = 30 \text{ mm}$ ) and vertical direction ( $H_s = 30 \text{ mm}$ ). The horizontal ones were built with the same strategy as the cubes and platelets. However, for the vertical samples the time between two following recoating procedures were set to 30 seconds considering the heat development because of the greater height of these samples.

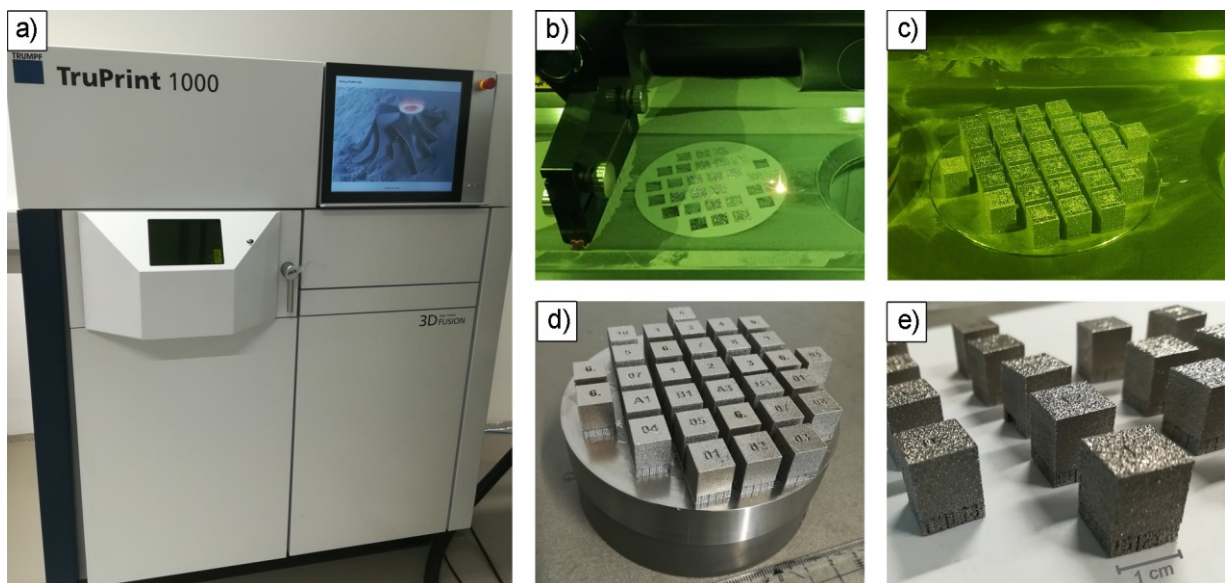


Figure 9: a) TruPrint1000 (TRUMPF) powder bed fusion system, b-e) SLM-fabrication of cubes investigated in this thesis.

### 3.3. Characterisation of the Bulk Samples

In order to determine the relative density,  $\rho_{rel}$ , of the SLM-fabricated cubes, produced with different processing parameters, density measurements using the Archimedean Principle in ethanol were carried out. Additionally, the same cubes were cut to investigate the microstructure of two perpendicular planes, the yz -plane and xy-plane, with a light optical microscope (LOM). A schematic drawing of the directions is shown in Figure 10a. To perform optical density measurements, the particle analysis menu of the image processing software ImageJ, was used. For this purpose 2 micrographs of each direction (xy and yz) were taken with the LOM. From these micrographs a representative picture section of 3.52 mm x 2.64 mm was taken. Subsequently, the micrographs were converted to 8-bit images, and an individually defined threshold-level separates the pores from the bulk material. Cut-off pores at the edges of the micrographs are excluded from the measurements. The software displays the selected area fraction of the pores in a table and an image with the contours of the individual pores. The results of the analysis were evaluated by Microsoft Excel, where the average area fraction of the pores was calculated and the relative density of the sample thereof.

To visualise the melting pools and the layer-wise structure of the yz- plane, the samples, which were also used for the optical density measurements, were chemically etched. For this, a solution of 45 ml distilled water (H<sub>2</sub>O), 45 ml of nitric acid (HNO<sub>3</sub>) and 10 ml of hydrofluoric acid (HF) was prepared. The etching time was 45 s [44]. Micrographs were taken with the LOM afterwards.

X-ray diffraction (XRD) characterisation of selected samples of the SLM parameter study (Table 1) was done with a BRUCKER D2 Phaser diffractometer with Co-K $\alpha$  radiation. All the XRD scans of the cubes were conducted on the yz-plane and are therefore representative of the whole sample. In Figure 10b the characterised yz-plane is shown. The measurements were implemented for 2Theta ( $2\theta$ ) from 20° to 120° with 3000 steps and 0.5 seconds per step. Also other samples fabricated in the scope of this thesis, i.e. tensile test samples, bending test sample, were measured with this investigation tool and the same parameters.

In order to gather information about the phase transitions' temperatures, the crystallization enthalpy and the structural relaxation differential scanning calorimetry (DSC) measurements were performed with a METTLER TOLEDO DSC 3+ with a heating rate of 20 K/min. For these measurements aluminium crucibles were used as well as 50 ml/min argon gas flow to reduce oxidation. The samples for the DSC measurements were cut from the same cube, on which density measurements and XRD were performed, Figure 10c. The heating cycle (5 min isotherm holding at 550 K,

heating up (20 K/min) from 550 K - 850 K, 5 min isotherm holding at 850 K, cooling down (20 K/min) to 550 K) was repeated two times in order to verify the measurements and to ensure a complete crystallisation of the sample. The glass transition temperature was determined by the means of the curve of the fully crystalline sample.

Vickers hardness of selected samples of the SLM parameter study (Table 1) was measured on the xy- and yz-plane. On each plane 5 measurements with a load of 5 kgf (HV5) were carried out for 10 seconds. An average hardness value was calculated of all the measured values and should represent the hardness of the whole sample. The measurements were performed manually with a FRANK hardness tester. In addition, micro-indentation measurements were performed with an instrumented indentation tester from the company Anton Paar, in order to determine the indentation hardness as well as the indentation elastic modulus for selected samples. For this, 5 indentations with an indent spacing of 100  $\mu\text{m}$  per sample on the yz-plane were performed with a loading rate of 2 N/mm and a maximum load of 1 N. The evaluation of the hardness and elastic modulus was performed with the software CSM Indentation. Thereby, the Oliver & Pharr method was used.

To determine the load for Vickers hardness measurements, the indentation size effect was measured on one sample, namely 01\_13. For this determination the maximum loading was varied from 0.05 N to 30 N and 3 indentations per load with an indent spacing of 100  $\mu\text{m}$  were carried out on the yz-plane. The loading rate was held constant at 2 N/mm for all these measurements.

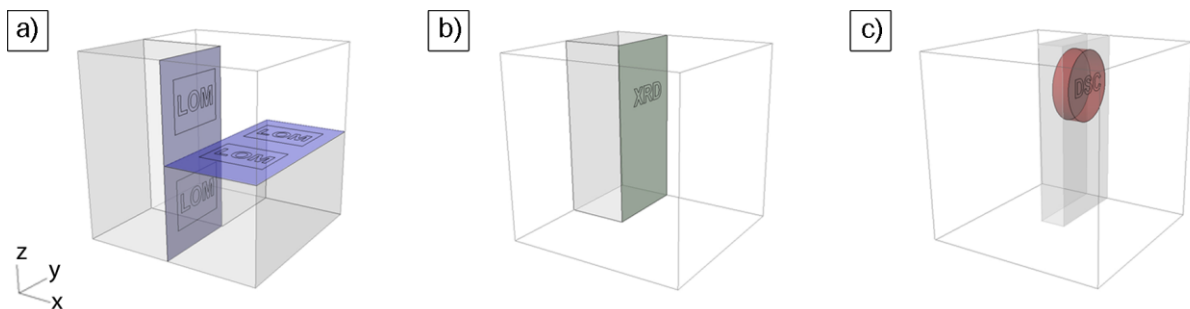


Figure 10: Schematic drawings of the cubic samples (1 cm x 1 cm x 1 cm) for a) LOM investigations and optical density measurements b) XRD measurements and c) DSC measurements.



Sample ID	Power [W]	Speed [mm/s]	Hatching [mm]	Layer Thickness [mm]	Energy Density [J/mm <sup>3</sup> ]	XRD measurement	DSC measurement	Hardness measurement
01_13	140	1600	0.10	0.05	17.50	x	x	x
02_18	160	1200	0.15	0.05	17.78	x	x	x
03_10	140	800	0.20	0.05	17.50	x	x	x
04_13	120	2000	0.08	0.05	15.00	x	x	x
05_08	100	2200	0.06	0.05	15.15	x	x	x
05_11	100	2800	0.06	0.05	11.90	x	x	
07_A1	40	800	0.08	0.02	25.00			x
07_A3	80	2000	0.08	0.02	25.00		x	x
07_B3	80	2400	0.08	0.02	20.83		x	
07_16	80	2800	0.08	0.02	16.67		x	x
08_02	40	1000	0.10	0.02	20.00			x
08_04	60	1200	0.10	0.02	25.00			x
<b>08_06</b>	<b>80</b>	<b>1200</b>	<b>0.10</b>	<b>0.02</b>	<b>33.33</b>	<b>x</b>	<b>x</b>	<b>x</b>
09_01	40	800	0.08	0.02	31.25			x
09_02	60	1200	0.08	0.02	31.25			x
09_05	60	1800	0.08	0.02	20.83			x
09_06	80	1600	0.08	0.02	31.25	x	x	x

Table 1: Relevant samples of the SLM parameter study and their process parameters. Samples were chose for XRD, DSC measurements and Vickers hardness measurements. The parameter set of samples 08\_06 was selected for the production of bending test and biocompatibility test samples and is highlighted in the table.

### 3.4. Post Processing

#### 3.4.1. Heat Treatment

To study the influence of a subsequent heat treatment on the microstructure and consequently on the mechanical and cytotoxic properties of the SLM-fabricated samples, as-built samples were isothermally annealed at 650 K (below  $T_g$ ) and 850 K (above  $T_x$ ) for 60 minutes in each case. The heat treatment was carried out in a protective gas muffle furnace from LINN High Therm GmbH using Ar-gas to reduce oxidation during the process.

In the first step, as-built cubes with the selected parameter set 08\_06 of the SLM parameter study were heat-treated and investigated. For the investigations, the above described methods and the equipment were employed. Afterwards, the cytotoxicity and 4-point bending test samples were also heat-treated. However, in the case of the heat treatment above  $T_x$ , difficulties regarding the subsequent surface treatment occurred. Therefore, the heat treatment of the 4-point bending test samples at 850 K were carried out after the surface treatment.

#### 3.4.2. Surface Treatment

Since as-built parts will hardly find application in the medical field due to the adherent powder particles on the surface, a subsequent surface treatment after the SLM process is necessary. Because of this, the influence of two different blasting treatments was investigated. To compare the treatments, the hexagonal platelets and 4-point bending tests were treated with glass microbeads ( $\text{SiO}_2$ , 150  $\mu\text{m}$  - 250  $\mu\text{m}$ ) for 60 s on the one hand and with corundum ( $\text{Al}_2\text{O}_3$ , 150  $\mu\text{m}$  – 212  $\mu\text{m}$ ) for 30 s on the other hand. For the blasting processes a blasting machine from RAGA Strahltechnik GmbH was utilised. The treatments were carried out with a pressure of 3.5 bar and a blasting angle of 45°.

After each post processing (heat and surface treatment), the surface roughness of the hexagonal platelets as representatives was measured. These measurements were carried out with a portable surface roughness tester (Mitutoyo SJ210;  $\lambda_c = 0.8$  mm  $v = 0.5$  mm/s). Each sample was measured 5 times and the average of  $R_a$  and  $R_z$  was calculated out of these values. Furthermore, micrographs of the samples surfaces were taken with a stereomicroscope and with the SEM at different magnifications. In order to detect glass or corundum particles implanted during the surface treatment, EDX measurements were executed with the SEM as well.

### 3.5. 4-Point Bending Tests

In order to investigate the room temperature mechanical behaviour of the SLM-fabricated BMG samples, 4-point bending tests were performed at the Erich Schmid Institute of Material Science in Leoben, Austria. Thereby, the influence of the building orientation and the post processing was investigated. For the measurements, different test series, were carried out using a Zwick universal testing machine (Zwick Roell, type Z100, Germany). The dimensions of the test setup can be seen in Figure 11a. The loading was applied with a cross head speed of 0.1 mm/min until fracture occurred. To measure the deflection more accurately, an inductive sensor connected to the software program DASYLab was additionally used. Flexural stress was then calculated according to

$$\sigma_b = \frac{M_b}{W} = \frac{3F(L-l)}{2b_s h_s^2} \quad (2)$$

where  $F$ ,  $L$ ,  $l$ ,  $b_s$ , and  $h_s$  are the applied force, the distance between the supportings, the distance between the loading points and, the sample's width and height, respectively.

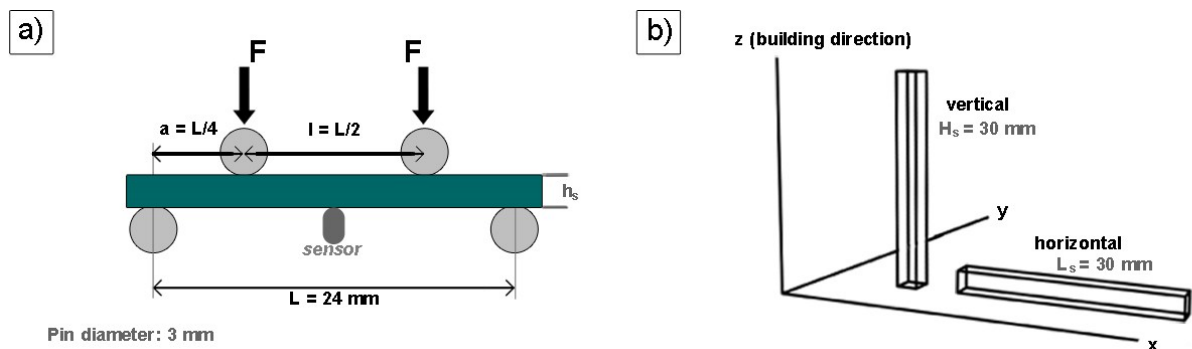


Figure 11: Schematic illustration of a) the 4-point bending test setup and b) the different building directions of SLM-fabricated bending test samples.

As mentioned above, different test series were carried out. First, vertically built samples with different surface treatment were tested (as-built, glass blasted and corundum blasted samples) in order to investigate the influence of the surface treatment on the mechanical properties. In the second test series, vertically built samples with one selected surface treatment, the glass blasting, were measured. Therein, samples in different thermodynamic state (as-built, structural relaxed and crystalline) were tested. In the third test series the bending behaviour of glass blasted samples built in horizontal direction were investigated. In this test series, the samples were inserted in 3 different orientation ( $H0^\circ$ ,  $H180^\circ$ ,  $H90^\circ$ ; Figure 39). In the first two test series the vertically built

samples were always inserted into the test setup with the same orientation, named V. An overview of the measured samples is given in Table 2.

The width,  $b_s$ , and height,  $h_s$ , of the various samples were measured on each side and in the middle of the beam using a digital calliper. For the calculation of the flexural stress and strain the average values of these measurements were used. All the values can be found in the Appendix, Section 1.5.

Test series	Samples	Building direction	Heat Treatment	Surface Treatment	Testing orientation
1	ASB7 - ASB10	Vertical	---	---	V
1	G1 - G3	Vertical	---	Glass blasted	V
1	K4 - K6	Vertical	---	Corundum blasted	V
2	12 - 21	Vertical	---	Glass blasted	V
2	24 - 29	Vertical	650 K/60 minutes	Glass blasted	V
2	40 - 46	Vertical	850 K/60 minutes	Glass blasted	V
3	H1 - H5	Horizontal	---	Glass blasted	H0°
3	H6 - H8	Horizontal	---	Glass blasted	H180°
3	H9 - H15	Horizontal	---	Glass blasted	H90°

*Table 2: Overview of the measured bending test samples built in vertical and horizontal direction and subjected to different post processing (heat and surface treatments). The testing orientation was varied depending on the sample.*

### 3.6. Cytotoxicity, Cell Adhesion and Cell Growth

To evaluate the behaviour of the SLM-fabricated Zr-based BMG regarding its cytotoxicity, in-vitro tests according to ISO 10993-5 and ISO 10993-12 were carried out at the Medical University Graz. As samples for the evaluations, the vertically built hexagonal platelets were used. Thereby, four different types of samples (as-built + glass blasted / as-built + corundum blasted / heat-treated at 650 K + glass blasted / heat-treated at 650K + corundum blasted) were tested to investigate the influence of the applied heat treatment and surface treatments on the cytotoxicity. To simulate the case of application as implants, the cell line Saos-2 which is a human osteosarcoma cell line was chosen for the tests. The test procedure was as follows:

- sterilising the samples using 70% ethanol twice for 5 minutes,
- rinsing them twice in phosphate-buffered saline (PBS),
- expose the samples to UV light for one hour before incubating them in the culture medium, a McCoy's 5a Medium,
- incubation for 24 hours with slight shaking at 37°C, 5% CO<sub>2</sub>,
- adjusting the pH value after incubation to 7.0 - 7.5,
- adding the cell culture to the culture medium,
- analysing the cell growth after 72 hours.

For the determination of the number of viable cells a colorimetric method (Cell Titer 96® Aqueous Non-Radioactive Cell Proliferation Assay [45]) was used. For this a small amount of the CellTiter® Aqueous One Solution Reagent was directly added to the culture wells. After an incubation time of 1 - 4 hours the absorbance at 490 nm was recorded with a 96-well plate reader. The amount of the absorbance is directly proportional to the number of living cells in the culture. In the presence of cytotoxic substances, cell growth inhibition with different proliferation and division rates appears. As a result, the amount of absorbance changes. The defined cut-off limit is 70% compared to the control cells grown under physiological cultivation condition. In the executed cytotoxicity test different dilutions of the culture medium (pure medium, 1:2, 1:5, 1:10 and 1:20) were used and in each case 4 SLM-fabricated platelets were tested. Additionally, a negative (untreated, non-cytotoxic) and a positive (cytotoxic) control was included in order to confirm the validity of the test system. In Figure 12, a picture of the test setup is shown. The results of the photometric analysis were also verified by microscopy.

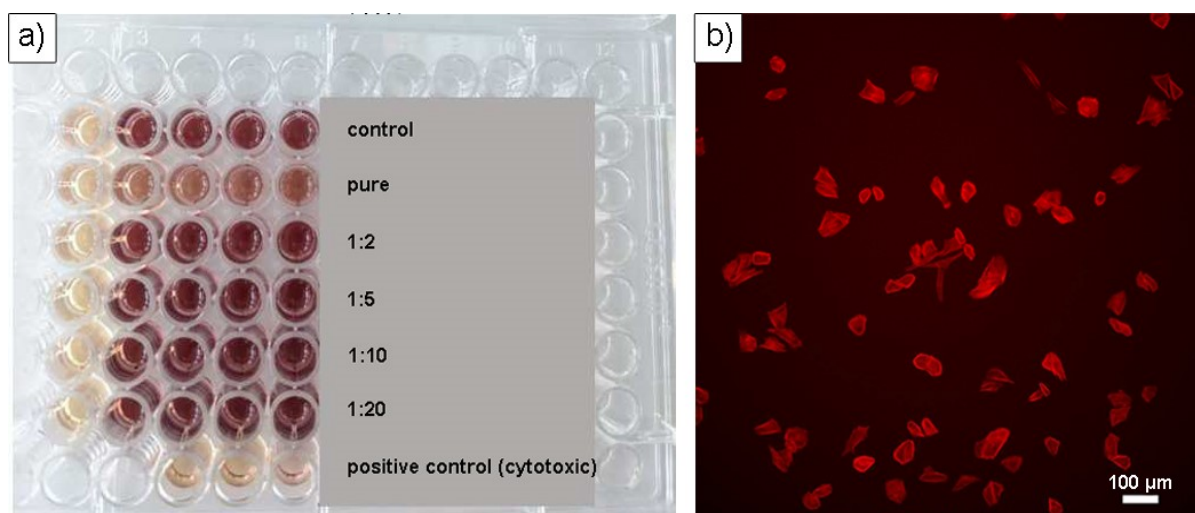


Figure 12: a) Setup of the cytotoxicity test, b) stained cells (cell line Saos-2).

In order to visualise the cells morphology and to investigate the surface adhesion of the cells, samples with grown cells were treated with Invitrogen™ Rhodamine Phalloidin. Rhodamine Phalloidin is a probe highly affine to F-actin, which is a specific protein that forms microfilaments in cells. Coupled together with the red-orange fluorescent dye, tetramethylrhodamine (TRITC), Rhodamine Phalloidin enables an accurate investigation of the cells shape, size, and structure [46]. An example of Rhodamine Phalloidin stained cells are presented in Figure 12b.

For the investigation of the cells, a fluorescent phalloidin stock solution (methanolic) was prepared first. Then, the grown cells were fixed in 3.7% methanol-free formaldehyde solution (10 minutes at room temperature) and permeabilized with a solution of acetone (3 minutes at  $-20^{\circ}\text{C}$ ). Afterwards, the cells were stained with the fluorescent phalloidin solution (20 minutes at room temperature). More precise information of the staining process can be found in [47]. The stained cells were analysed with a fluorescence microscopy (Excitation/Emission: 540/565 nm).

## 4. Results and Discussion

### 4.1. Powder Characterisation

In Figure 13, the powder particles of the  $Zr_{65.5}Cu_{15.6}Ni_{11.8}Ti_{3.3}Al_{3.7}$ -BMG are shown. The SEM micrographs were taken of the as received powder (Figure 13a and b) as well as of the embedded and subsequently grounded powder (Figure 13c and d). The majority of the particles are of spherical shape. However, there are also larger particles, which exhibit a rod- or needle-shaped morphology. The surface of the particles is mostly smooth and homogeneous; only a few particles show some small satellites and a splattered surface. The spherical shape and the smooth surface have a positive effect on the pourability and flowability of the powder. The internal structure of the powder particles is mainly pore free.

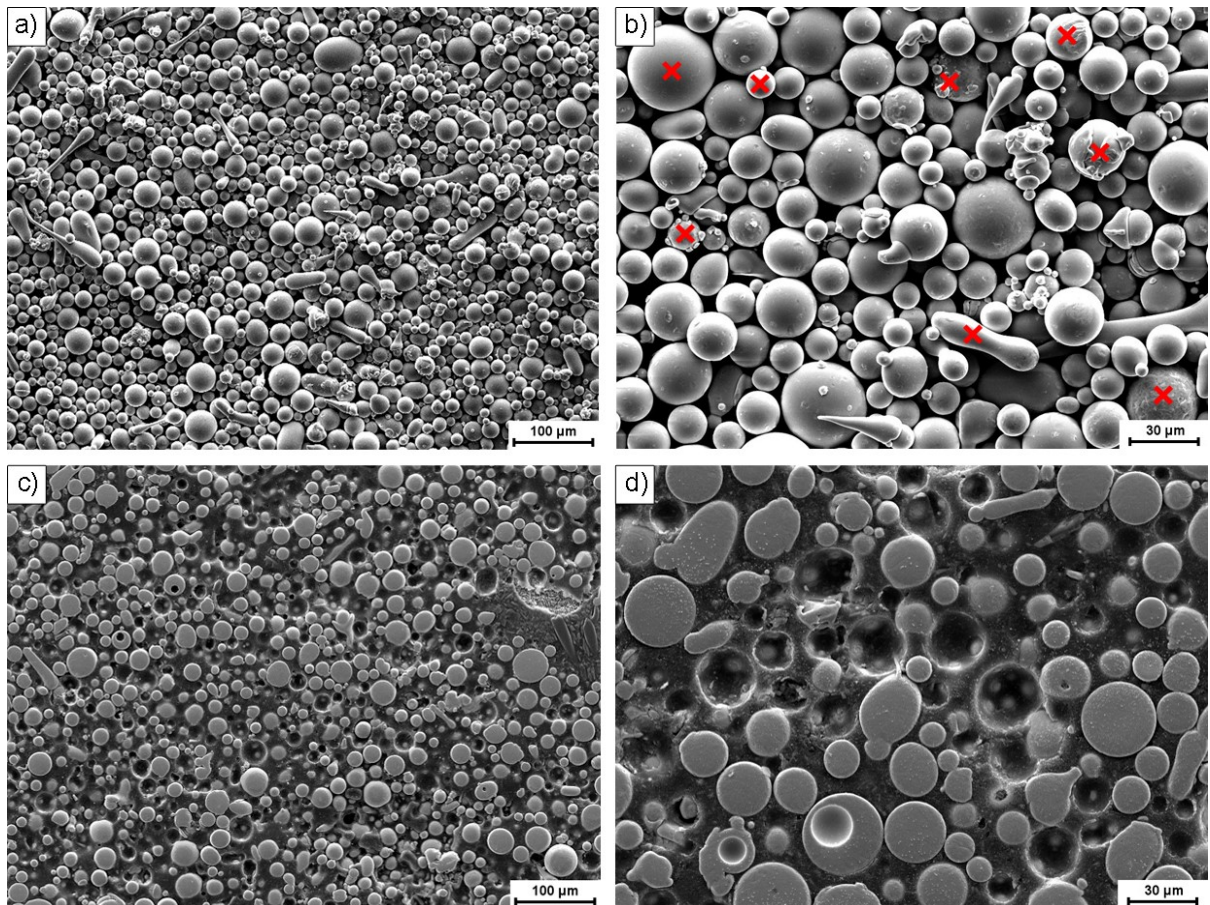


Figure 13: SEM micrographs of the BMG powder particles used for the SLM process: a) powder particles - as received b) magnified image of the as received powder particles; red crosses marking the points, where EDX spot measurements were taken, c) powder particles- embedded and grounded d) magnified image of the grounded particles.



The results from the particle size analysis are shown in Figure 14. The size distribution ranges from 1  $\mu\text{m}$  to 300  $\mu\text{m}$ . The values of  $D_{10}$ ,  $D_{50}$ , and  $D_{90}$  are  $15.2 \pm 0.76 \mu\text{m}$ ,  $24.6 \pm 1.23 \mu\text{m}$ , and  $36.4 \pm 1.82 \mu\text{m}$ , respectively. The measured average sphericity of the particles is 0.93. However, smaller particles with a size lower than 70  $\mu\text{m}$  have a sphericity higher than 0.9 and, the larger particles are mainly nonspherical, Figure 14b. This result corresponds to the micrographs taken with the SEM.

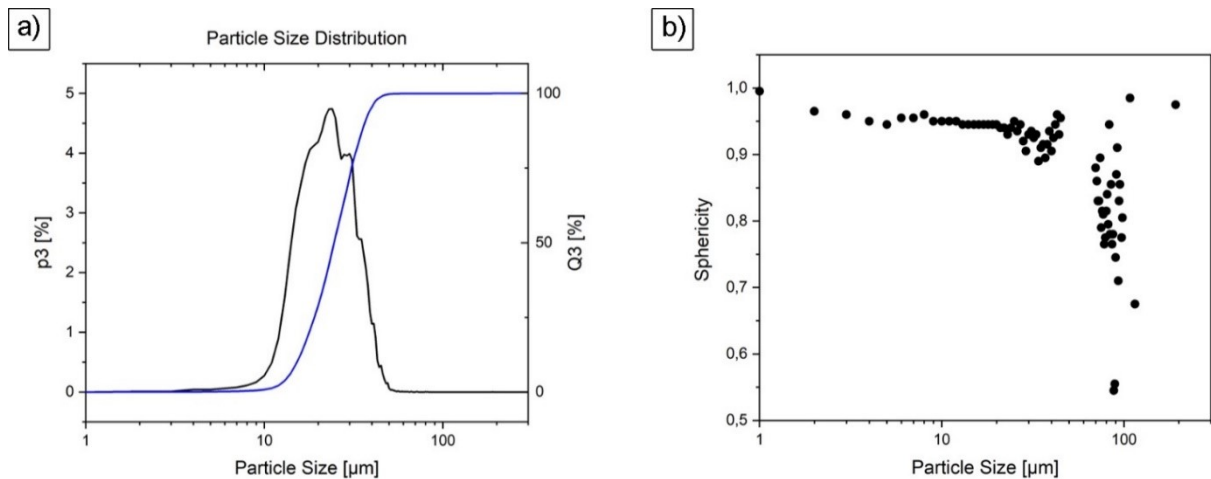


Figure 14: Results of the particle size analysis of the supplied VIT105 powder. a) Particle Size Distribution, and b) representation of the sphericity of the powder particles.

EDX measurements with the SEM were done as spot measurements on various powder particles to determine the powder particles' actual chemical composition. The spots are marked as red crosses in Figure 13b. The evaluated data of these measurements are shown in Table 3. Hardly any differences are observed between nominal and measured composition.

To get a rough appraisal of how the elements are distributed, an EDX map was further recorded (Figure 15). It can clearly be seen that the elements are distributed homogeneously and the measurement shows that the composition is in good accordance with the given specification.



	Zr	Cu	Ni	Ti	Al
<b>Nominal</b>	65.5	15.6	11.8	3.3	3.7
<b>Spot measurements (8 single measurements, Figure 13)</b>					
Maximum	67.95	18.53	13.18	4.89	4.70
Minimum	60.80	14.21	10.27	3.89	3.20
Average	64.99 ± 2.19	15.60 ± 1.41	11.19 ± 0.98	4.31 ± 0.40	4.05 ± 0.48
<b>EDX map</b>	60.35 ± 0.10	18.48 ± 0.10	13.22 ± 0.10	4.09	3.86

Table 3: Results of the EDX measurements in wt% of the powder.

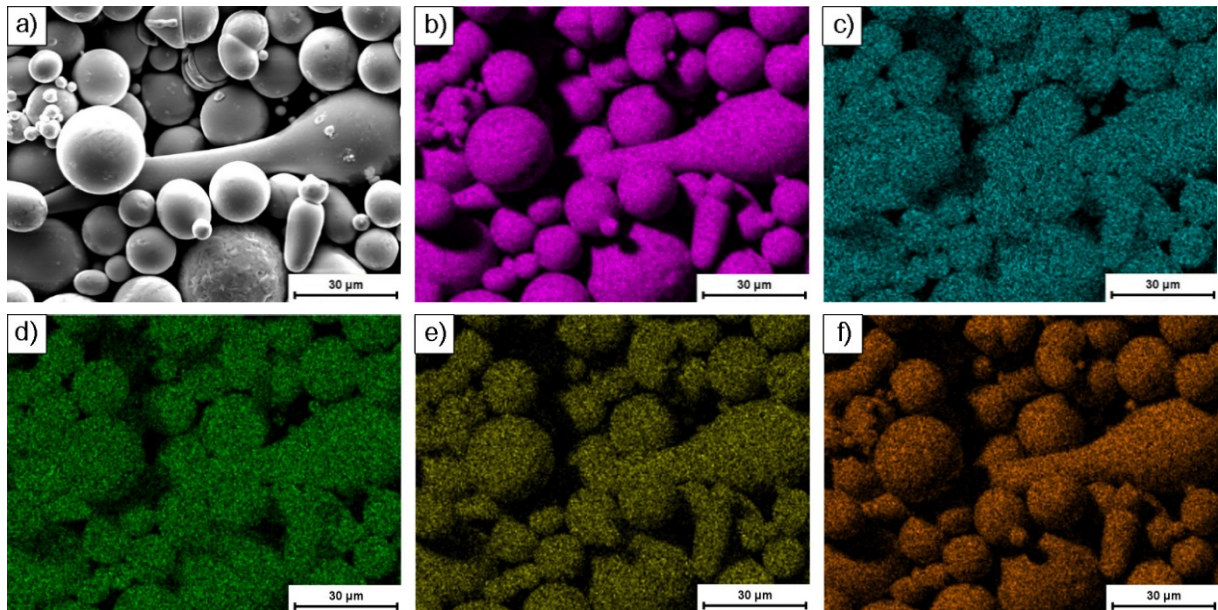


Figure 15: a) SEM micrograph of the analysed powder and the corresponding EDX maps of b) Zr c) Cu d) Ni e) Ti f) Al.

## 4.2. SLM Parameter Study

For the SLM parameter study, various building jobs with different laser parameters (laser power,  $P$ , scanning velocity,  $v$ , and hatching,  $h$ ) and consequently different volume energy densities,  $E$ , were carried out. The used parameters for the building jobs are given in Section 7.1. At a starting point, parameters based on previous research of Li et al. [30] and Pauly et al. [29] were utilised for the larger layer thickness  $t_{s1}$  and greater hatchings. Additionally, building jobs with smaller hatchings were carried out. For layer thickness  $t_{s2}$ , the results of the before investigated samples with a layer thickness of  $t_{s1}$  provided a rough indication, which energy density is necessary to obtain dense samples.

### 4.2.1. Relative Density and Microstructure Analysis

In Figure 16, selected LOM micrographs of 4 different samples of the SLM parameter study with the same layer thickness of 0.05 mm are shown. These micrographs represent the behaviour of the microstructure of the cubes produced with different parameters. Micrographs of the other investigated samples of this layer thickness can be found in the Appendix, Section 7.2. From the micrographs, it can be seen that the samples produced with an energy density of  $8.89 \text{ J/mm}^3$  have a lot of pores. As a result no dense samples were obtained with these parameter sets. However, the size of the pores decreases simultaneously with the hatching. Furthermore, the pores' morphology varies with regard to the chosen hatching, observed in the  $yz$ -plane (Figure 16e-g). While the pores are oriented in building direction in sample 03\_19, which has the largest used hatching of 0.20 mm, the sample 05\_07 with a hatching of 0.06 mm has pores oriented perpendicularly to the building direction. This is an indication that in the samples which are produced with larger hatching, the vector lines of the scanning pattern were too far away from each other and the energy density was too low to melt enough powder and establish an adequate connection. Because of that, there are also not-molten powder particles present in those pores. This characteristic is also observed for the hatching of 0.15 mm and 0.10 mm. For the samples which were built with smaller hatching than 0.10 mm it seems that, the hatching is good enough. However, no acceptable connection between the built layers could be obtained, either due to the power being too low or due to the scanning velocity being too high.

Denser samples could be produced with an energy density higher than approximately  $15 \text{ J/mm}^3$  for all used hatchings. As an example for a dense sample, micrographs of sample 01\_13 are shown in Figure 16d and h. There are only a few pores with an almost spherical shape visible. The determined feret diameter of the largest pore found

on the micrographs of this sample throughout the optical density measurements with ImageJ was  $85 \mu\text{m}$ . In comparison to that, the largest pore in sample 03\_19 had a feret diameter of  $2107 \mu\text{m}$ .

In Figure 17a and b the values of the measured relative densities,  $\rho_{\text{rel}}$ , of the SLM-fabricated cubes are shown as a function of the energy density used in the building jobs. The densities of all cubes from the SLM parameter study were determined and related to the density given in [48]. Again, it becomes obvious that samples produced with low energy density are porous. In contrast, the samples are getting denser when the energy input increases. The greater distribution of the optically determined relative densities results from the dependence of the chosen image section and selected pores. Especially in porous samples with numerous pores this dependence plays a significant role. Nonetheless, the trend of the relative density is identical to the one in the density measurements using the Archimedean principle. The observed tendency that the smaller hatchings are advantageous for producing dense samples is confirmed by the density measurements. However, the values show that samples with a hatching of  $0.06 \text{ mm}$  are less dense than samples with a hatching of  $0.08 \text{ mm}$ .

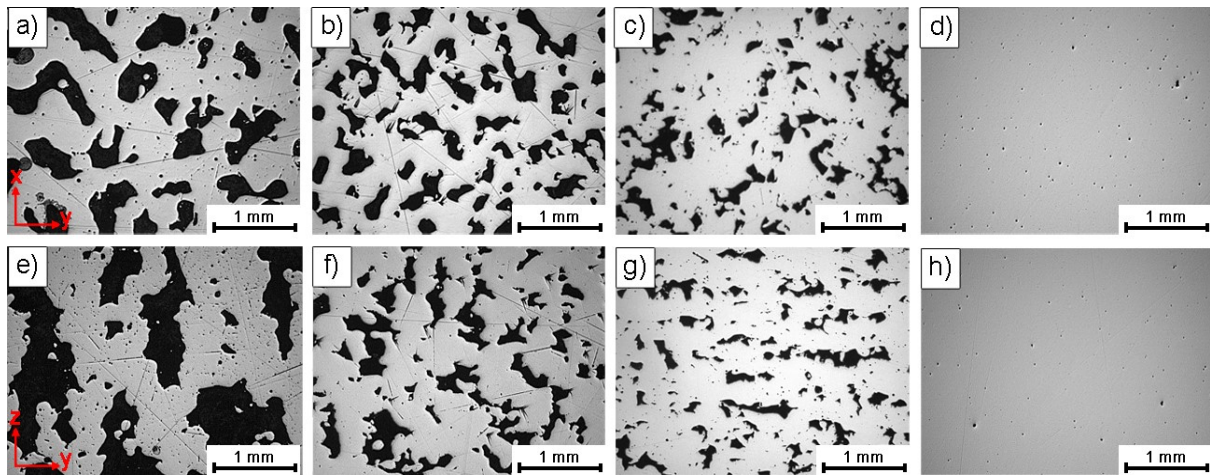


Figure 16: LOM images of cubic samples produced with a layer thickness  $ts1 = 0.05 \text{ mm}$ . Upper row:  $xy$ -plane; lower row:  $yz$ - plane. a), e)  $E = 8.89 \text{ J/mm}^3$ ,  $h = 0.20 \text{ mm}$  (sample: 03\_19), b), f)  $E = 8.89 \text{ J/mm}^3$ ,  $h = 0.10 \text{ mm}$  (sample: 01\_05), c), g)  $E = 8.89 \text{ J/mm}^3$ ,  $h = 0.06 \text{ mm}$  (sample: 05\_07), d), h)  $E = 17.50 \text{ J/mm}^3$ ,  $h = 0.10 \text{ mm}$  (sample: 01\_13).

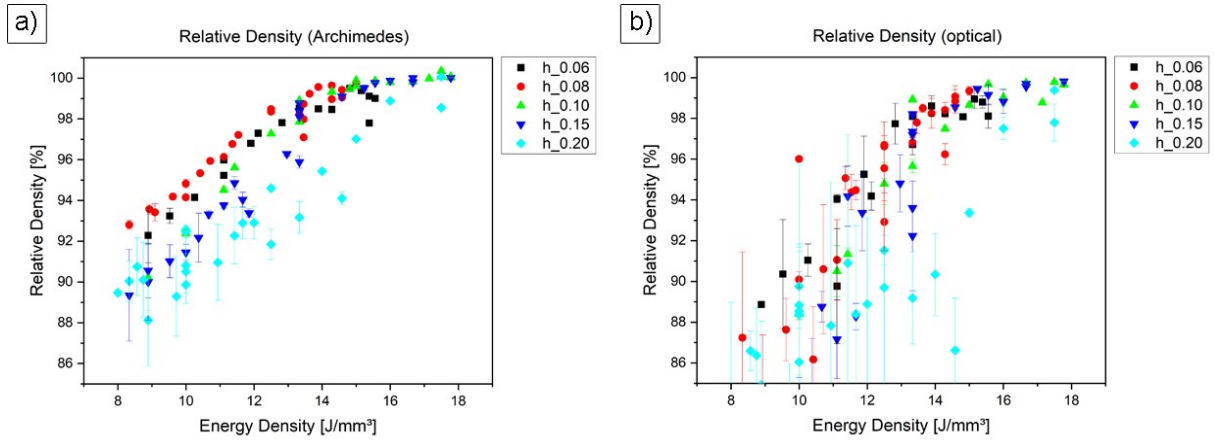


Figure 17: Relative densities of the cubes fabricated with a layer thickness of  $ts_1 = 0.05$  mm, different hatchings and energy densities. a) Relative density measured by the Archimedean principle and b) relative density determined optically.

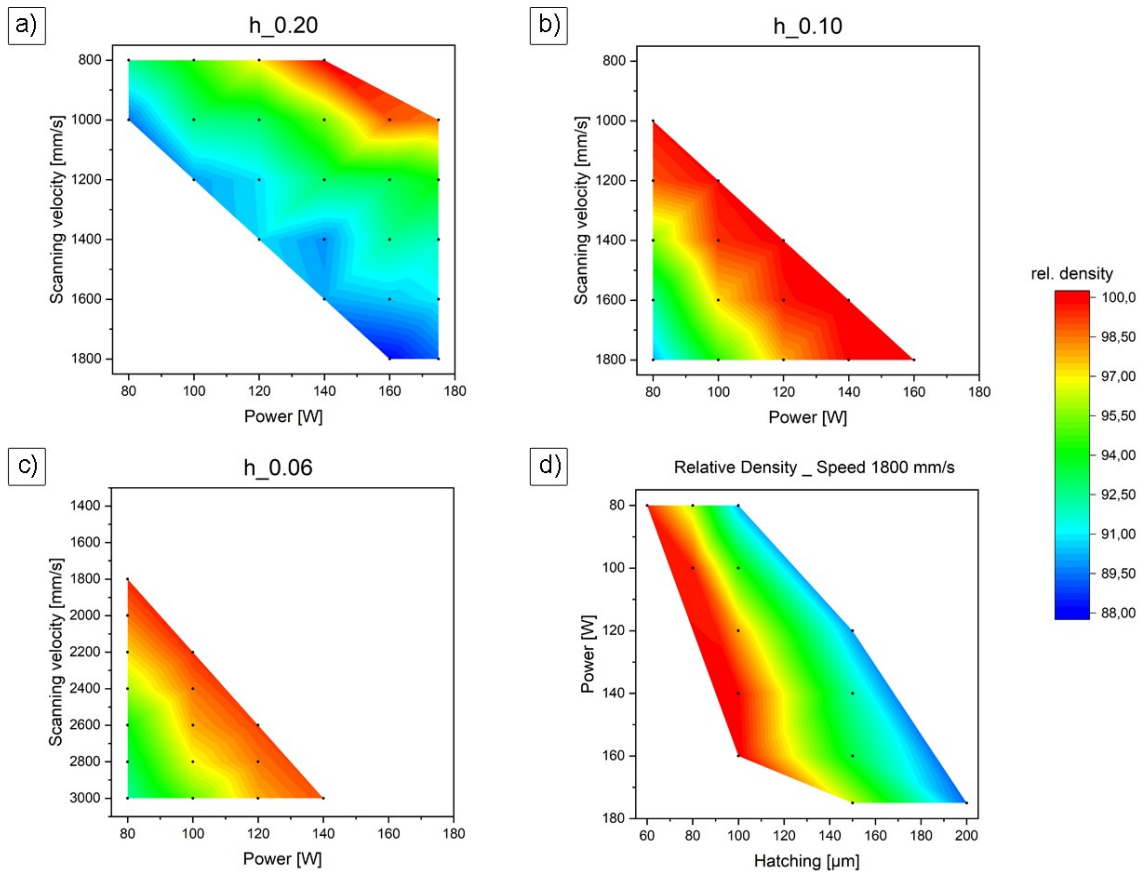


Figure 18: Relative density, measured by the Archimedean principle, as a function of scanning velocity and laser power for the cubes produced with layer thickness of  $ts_1=0.05$  mm and a hatching of a) 0.20 mm, b) 0.10 mm and c) 0.06 mm. d) Relative densities of cubes produced with a given scanning velocity of 1800 mm/s.



Since there is a relation between all the process parameter (Equation (1)), it is not enough to only consider the energy density and the hatching as a criterion for producing BMGs by SLM. In Figure 17, it can be seen that for a given hatching and energy density the values of the relative density differ slightly. Therefore, the relation between the used laser power, the laser velocity and the resulting relative density of the built cubic samples were plotted as density contour maps with OriginPro 2020 (Figure 18a-c). From these maps it becomes clear that for a given hatching and energy density, it is favourable to use lower laser power and velocity rather than higher values of these parameters to obtain denser samples. However, according to [30], amorphous Zr- based BMGs can be produced by using low energy input and a laser velocity of more than 1500 mm/s. Thus, a scanning velocity of 1800 mm/s was chosen for the density contour map in Figure 18d to visualise the needed power and hatching so as to obtain a dense sample with a layer thickness of 0.05 mm.

LOM micrographs of selected cubic samples with the thinner layer thickness of 0.02 mm are shown in Figure 19a-h. Again, these micrographs are representatives. Further micrographs of the different samples can be found in the Appendix in Section 7.2. Compared to the samples with a layer thickness of 0.05 mm, the samples with an energy density of  $16.67 \text{ J/mm}^3$  still have a lot of pores. Furthermore, the assumption that a lower hatching of 0.08 mm is more advantageous than a hatching of 0.10 mm cannot be transferred to this layer thickness. For lower energy densities, the samples with the smaller hatching clearly show a lower relative density. Only at higher energy densities ( $E > 20 \text{ J/mm}^3$ ), the samples become denser. At these energy densities, the difference in the used hatching vanishes (Figure 20).

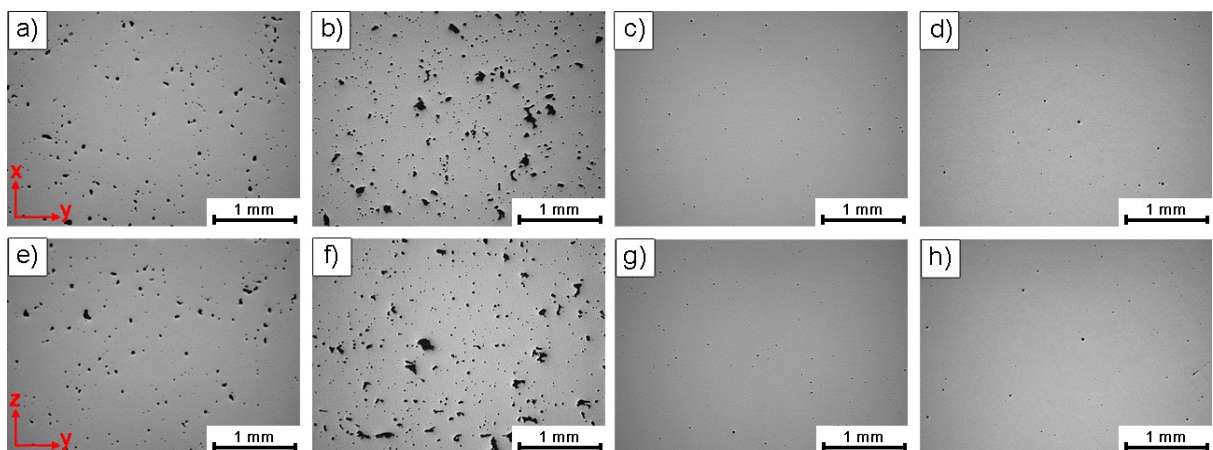


Figure 19: LOM micrographs of the investigated cubic samples of the SLM parameter study with a layer thickness of  $ts_2 = 0.02 \text{ mm}$ . a), e)  $E = 16.67 \text{ J/mm}^3$ ,  $h = 0.10 \text{ mm}$  (sample: 06\_05), b), f)  $E = 16.67 \text{ J/mm}^3$ ,  $h = 0.08 \text{ mm}$  (sample: 07\_16), c), g)  $E = 33.33 \text{ J/mm}^3$ ,  $h = 0.10 \text{ mm}$  (sample: 08\_06), d), h)  $E = 31.25 \text{ J/mm}^3$ ,  $h = 0.08 \text{ mm}$  (sample: 09\_06).

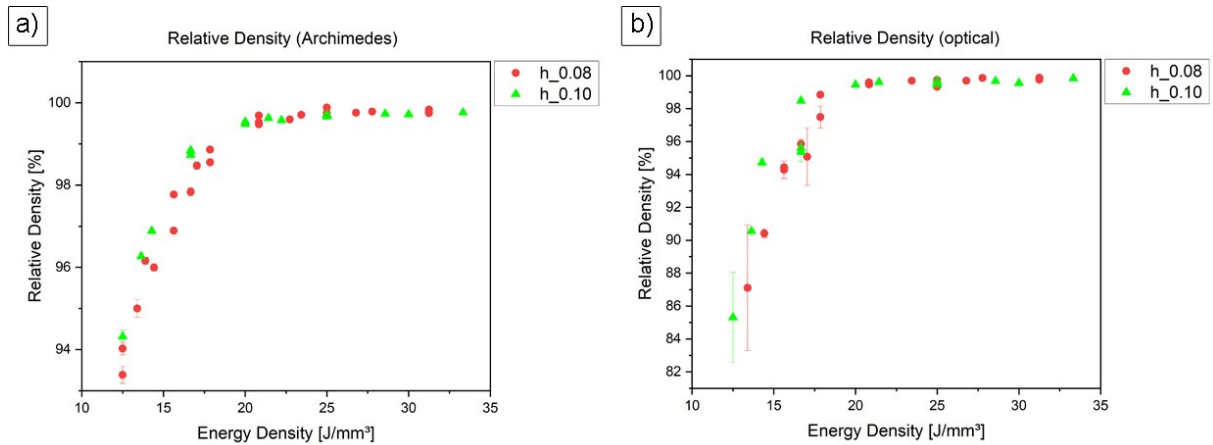


Figure 20: Relative densities of the cubes fabricated with a layer thickness of  $ts_2 = 0.02$  mm, different hatchings and energy densities. a) Relative density measured by the Archimedean principle and b) relative density determined optically.

An explanation for the low relative density of samples produced with an energy density lower than  $20 \text{ J/mm}^3$  could be the high scanning velocities. As mentioned above, it is favourable to have lower values of the laser's velocity to produce samples with fewer pores. If one compare the process parameters of sample 06\_05 ( $\rho_{\text{rel,archimedes}} = 98.85 \pm 0.06 \%$ ) to sample 01\_01 ( $\rho_{\text{rel,archimedes}} = 99.80 \pm 0.08 \%$ ) it becomes evident that despite having been produced the samples with almost the same energy density, the same hatching and laser power, the scanning velocity is  $2400 \text{ mm/s}$  for sample 06\_05 and  $1000 \text{ mm/s}$  for sample 01\_01. Therefore, as long as the laser power and the hatching is held constant and the layer thickness is reduced, a not too high scanning velocity and consequently a higher energy density are needed for the production of dense samples. A strong dependence of the relative density on the used power was also not observed for this layer thickness. However, the density measurements, especially the optically ones, may indicate that there is also a minimum required laser power to obtain dense samples, since there is an increase in relative density with increasing power for a given energy density.

A listing of the densest samples of the different layer thicknesses and used hatchings are provided in Table 4. Since the parameter study was performed to find parameters for the production of dense BMG samples, only these samples were of greater interest for further experiments. Process parameters of the samples can be found in Table 1 and in the Appendix in Section 7.1. Only in a few cases also other samples were analysed to find more correlations.

<b>Layer Thickness ts1</b>				
Hatching [mm]	$\rho_{rel,archimedes}$ maximum [%]	Sample [-]	$\rho_{rel,optical}$ maximum [%]	Sample [-]
0.20	100.07 ± 0.08	03_10	99.384 ± 0.015	03_10
0.15	100.02 ± 0.08	02_18	99.813 ± 0.069	02_18
0.1	100.35 ± 0.10	01_13	99.786 ± 0.069	01_13
0.08	99.90 ± 0.09	04_13	99.351 ± 0.212	04_13
0.06	99.48 ± 0.07	05_01	98.955 ± 0.484	05_08
<b>Layer Thickness ts2</b>				
Hatching [mm]	$\rho_{rel,archimedes}$ maximum [%]	Sample [-]	$\rho_{rel,optical}$ maximum [%]	Sample [-]
0.10	99.77 ± 0.03	08_06	99.848 ± 0.022	08_06
0.08	99.83 ± 0.03	09_06	99.877 ± 0.010	09_06

Table 4: Summary of the densest samples for layer thickness ts1 and ts2 and different hatchings. Process parameters of the various samples can be found in Table 1 and in the Appendix, Section 7.1.

In Figure 21 LOM micrographs of the chemically etched yz-plane of two samples with different layer thicknesses are shown. In Figure 21a, a sample with a layer thickness of 0.05 mm is shown and in Figure 21b, one with a layer thickness 0.02 mm. Both samples were produced with the same hatching of 0.10 mm, but with different values of the laser power and velocity. Since the etching preferably takes place at the melt pool boundaries, it is possible to visualise the during the SLM process formed structure. Elemental segregation, crystallisation or oxidation can be the explanation for the different etch rates at the boundaries [49, 50]. The melt pool pattern in both samples is complex. Therefore, it is hard to identify the periodicity of the scanning pattern and the layer-by-layer structure. One reason for this complex pattern is the rotation of the scanning pattern 67° in superposed layers. However, this indicates that the resulting microstructure is quite homogeneously. Besides, a clear difference is visible between the two layer thicknesses. The resulted melt pool pattern of the sample produced with thinner layer thickness is much finer and the layered structure is slightly more visible. Nevertheless, melt pool layers as depicted in [50] cannot be defined for the sample shown in Figure 21b.

In order to investigate, if elemental segregation took place during the SLM process EDX measurements were performed at the yz-plane of the samples. However, no accumulations of the containing elements were found in the investigated sample 01\_13 and the detected weight proportion of the sample is in good accordance with the given chemical composition of the used powder. The results of the EDX measurements are given in Table 5. Elements, like carbon and oxygen which can be detected almost always, were excluded from the EDX measurements.

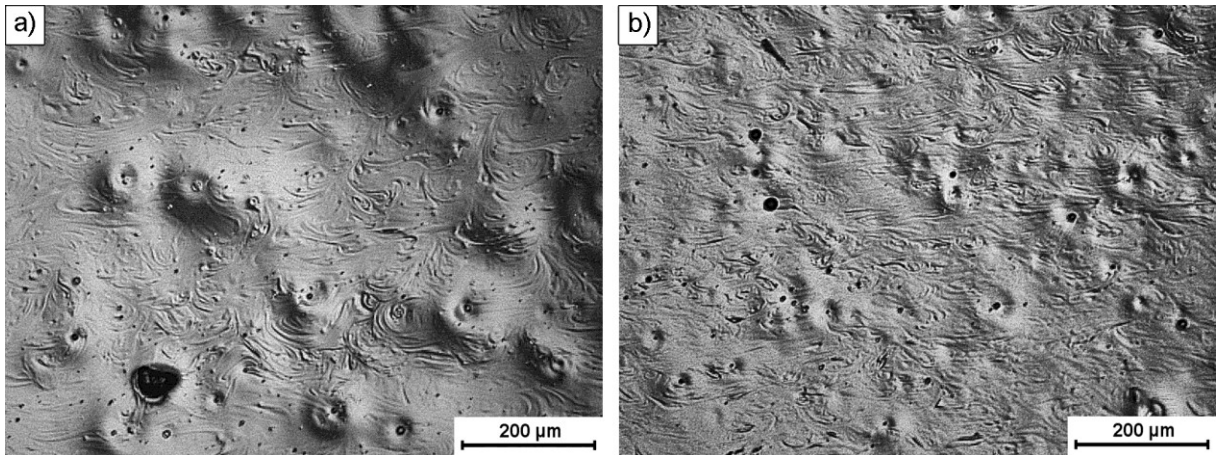


Figure 21: Chemically etched cross section of a) sample 01\_13, layer thickness 0.05 mm and b) sample 08\_06, layer thickness 0.02 mm.

	<b>Zr</b>	<b>Cu</b>	<b>Ni</b>	<b>Ti</b>	<b>Al</b>
Area 1	64.97	15.69	11.38	4.20	3.87
Area 2	65.03	15.64	11.40	4.13	3.80
Area 3	65	15	11	4	4
Average	$65.27 \pm 0.38$	$15.51 \pm 0.22$	$11.26 \pm 0.18$	$4.18 \pm 0.03$	$3.86 \pm 0.04$

Table 5: Results of the EDX spectroscopy measured on the yz-plane of the SLM-fabricated sample 01\_13.



### 4.2.2. XRD Measurements

X-Ray diffraction pattern of selected samples produced with different process parameters (Table 1) compared with the diffraction pattern of the used BMG powder are shown in Figure 22. The XRD pattern of the powder particles shows a broad scattering maximum without crystalline peaks, which is characteristic for metallic glasses. Therefore, it can be stated, that the used raw material mainly exhibits an amorphous microstructure. However, all the SLM-fabricated samples show this broad maximum as well, suggesting the amorphous nature of the sample produced by SLM. As all the tested samples are produced with the highest energy density within the used hatchings, it can be deduced that samples with lower energy density are also amorphous. To prove this assumption, other samples produced with lower energy densities were measured in the same way. These measurements confirmed this assumption. The additionally measured XRD patterns can be found in the Appendix, Section 1.2. Furthermore, no differences in the XRD patterns between samples produced with same energy density, but different laser power and velocity were found.

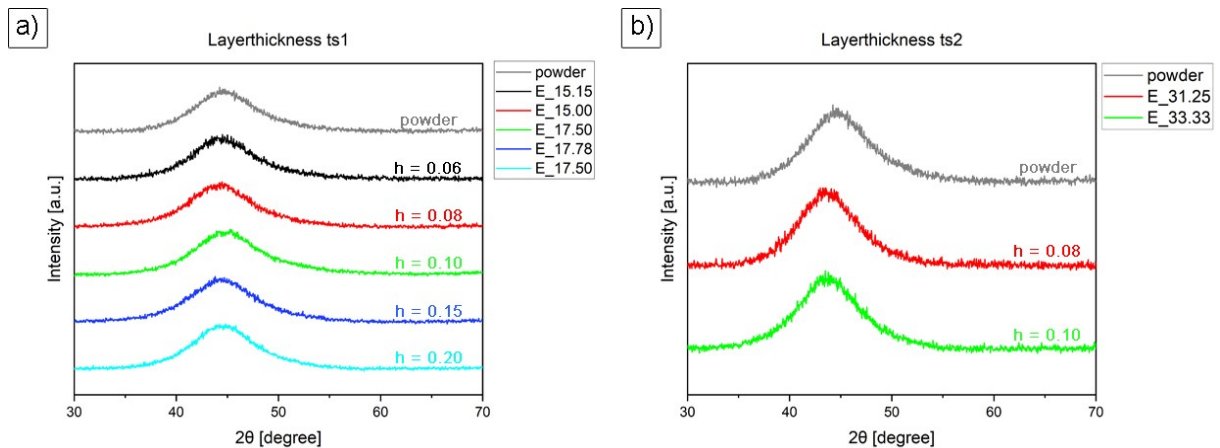


Figure 22: X-ray diffraction patterns of the used BMG powder and selected SLM-fabricated samples (Table 1). a) XRD patterns of samples produced with a layer thickness  $ts1 = 0.05$  mm and b) XRD pattern of samples produced with layer thickness  $ts2 = 0.02$  mm.

### 4.2.3. DSC Measurements

DSC measurements were carried out with a heating rate of 20 K/min to verify the results of the XRD measurements and to confirm the amorphous nature of the samples of the SLM parameter study. Furthermore, transition temperatures, crystallisation enthalpies and the structural relaxation were determined for various samples. Figure 23 shows the DSC curves of selected samples compared to the curve of the used powder. The comparison clearly shows that there is not only a difference between the samples and the powder, but also among the samples themselves. One difference can be seen at the third crystallisation peak above 800 K. While the DSC curve of the powder shows a well pronounced third crystallisation peak, the samples do not. Moreover, the crystallisation peak of the samples becomes even less pronounced when the used energy density increases (01\_13:  $E = 17.50 \text{ J/mm}^3$ , 04\_13:  $E = 15.00 \text{ J/mm}^3$ , 08\_06:  $E = 33.33 \text{ J/mm}^3$ , 09\_06:  $E = 31.25 \text{ J/mm}^3$ ). This can be an indication that partial crystallisation, which cannot be detected either with XRD nor EDX, takes place during the SLM process when higher energy densities are used. Another difference can be seen in the temperature range between 500 K and 650 K, where structural relaxation occurs.

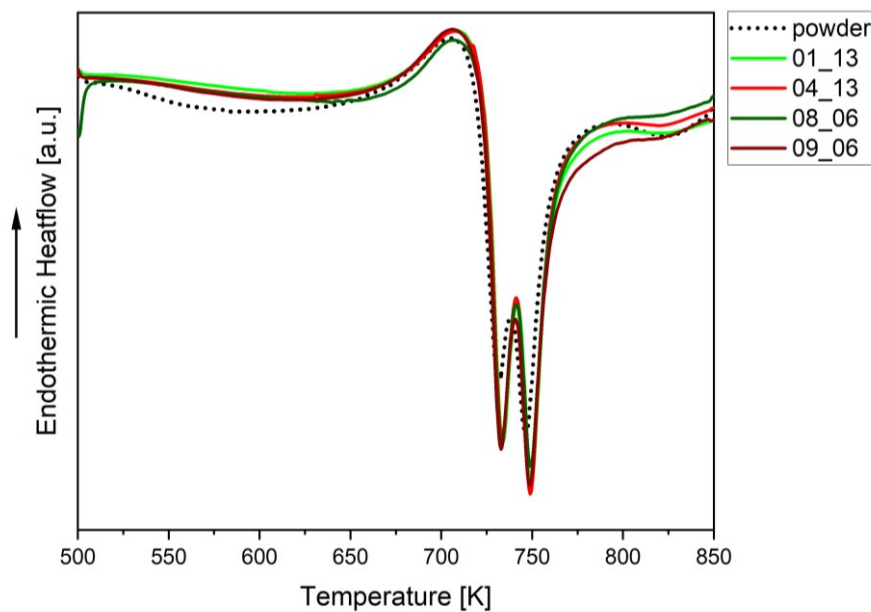


Figure 23: DSC curves of the used powder in comparison to the DSC curve of different SLM-fabricated samples obtained from the parameter study (Table 1). Measurements were executed at a heating rate of 20 K/min.

A detailed plot of the DSC curves in the temperature range between 500 K and 650 K is shown in Figure 24a. The determined values of the enthalpy of structural relaxation,  $\Delta H_{str}$ , are listed in Table 6. The results of the DSC measurements show that there is a correlation of the enthalpy and the scanning velocity which was used in the SLM process to produce the cubic samples (Figure 24b). To compare,  $\Delta H_{str}$  of the powder is marked in the figure as a dashed line. It is evident that with increased scanning velocities and lower laser power, samples with higher values of  $\Delta H_{str}$  can be obtained. While the sample 03\_10 ( $P = 140$  W,  $v = 800$  mm/s,  $E = 17.50$  J/mm<sup>3</sup>) exhibits an enthalpy of only  $-3.29 \pm 0.03$  J/g, the samples 01\_13 ( $P = 140$  W,  $v = 1600$  mm/s,  $E = 17.50$  J/mm<sup>3</sup>) and 07\_16 ( $P = 80$  W,  $v = 3000$  mm/s,  $E = 16.67$  J/mm<sup>3</sup>) have an enthalpy of  $-6.27 \pm 0.10$  J/g and  $-11.55 \pm 0.65$  J/g, respectively. An explanation for this could be, the different cooling rates of the samples, caused by different process parameters.

However, since the SLM process is influenced by many factors, such as the process parameters, the temperature distribution on the building platform, the used powder, and printing conditions, and only a few samples are measured one time by DSC, this

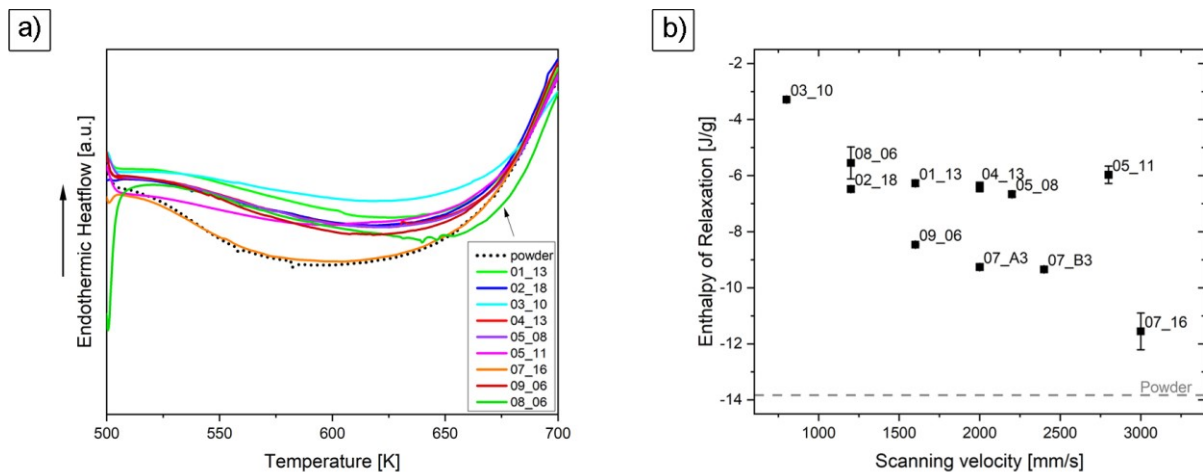


Figure 24: a) Detailed plot of the DSC curves measured at a heating rate of 20 K/min to investigate the enthalpy of structural relaxation, b) correlation between the determined enthalpy of structural relaxation ( $\Delta H_{str}$ ) and the scanning velocity used in the SLM process. Data points are labelled with the samples' identification. Process parameters of the samples can be found in Table 1.

The onset temperatures of the glass transition,  $T_{g,on}$ , determined by means of the DSC curve of the fully crystalline sample, are listed in Table 6. There are only slight differences between the values, with exception of the value of sample 08\_06. As seen in Figure 24a, its curve is slightly shifted to the right compared to the others. Consequently, the onset temperature is also shifted to higher values. Nevertheless, a minimal increase in the glass transition temperature with increasing scanning velocity (Figure 25a) can be found. This is in line with the assumption that with higher used scanning velocities the cooling rate of the sample is higher and consequently the glass transition point moves to higher temperatures.

In Table 6, the values of the determined crystallisation enthalpy  $\Delta H_x$  and the crystallisation onset temperature  $T_{x,on}$  of the first crystallisation peak are listed as well. The  $\Delta H_x$  values of the SLM-fabricated samples are in the same order as the  $\Delta H_x$  value of the powder. The only outlier is the sample 03\_10 with a  $\Delta H_x$  of  $-33.60 \pm 0.12$  J/g (Figure 25b). A reason for the tremendous difference may be the combination of a slow scanning velocity of 800 mm/s and a high laser power of 140 W, at which the sample was produced. As a consequence of these two process parameters, a lower cooling rate could be achieved and a formation of nanocrystals could take place during the SLM process. Similar to the glass transition temperature, the crystallisation onset temperature  $T_{x,on}$  of the samples follows the same trend: with increasing scanning velocity the onset temperature increases as well. This is also a result of the different thermal history of the samples. At this point it has to be mentioned, that the first two crystallisation peaks of the SLM-fabricated samples are shifted to the right by a few degrees (powder:  $T_{p1} = 731$  K,  $T_{p2} = 749$  K, samples:  $T_{p1} = 735 \pm 2$  K,  $T_{p2} = 751 \pm 1$  K) (Figure 23). In addition to the peak temperatures, the crystallisation end point was determined at  $840 \pm 1$  K for all measured samples.

From these results the temperatures for the subsequent heat treatment were derived. Since the onset temperature of the glass transition was determined at around 678 K, the temperature for the heat treatment below  $T_g$ , was defined to be at 650 K. For the heat treatment above  $T_x$ , a temperature of 850 K was chosen.

Sample	Glass Transition Temperature, $T_{g,on}$ [K]	Enthalpy of Crystallisation $\Delta H_x$ [J/g]	Crystallisation Onset Temperature, $T_{x,on}$ [K]	Enthalpy of Relaxation $\Delta H_{str}$ [J/g]
Powder	$678.1 \pm 0.5$	$-51.03 \pm 0.34$	$717.4 \pm 0.2$	$-13.83 \pm 0.22$
01_13	$679.0 \pm 0.8$	$-54.64 \pm 0.25$	$722.8 \pm 0.4$	$-6.27 \pm 0.10$
02_18	$675.7 \pm 0.8$	$-54.95 \pm 0.51$	$721.2 \pm 0.8$	$-6.48 \pm 0.09$
03_10	$675.0 \pm 1.0$	$-33.60 \pm 0.12$	$719.7 \pm 0.6$	$-3.29 \pm 0.03$
04_13	$678.2 \pm 0.5$	$-53.79 \pm 0.14$	$721.7 \pm 0.8$	$-6.40 \pm 0.17$
05_08	$678.5 \pm 0.2$	$-53.65 \pm 0.36$	$723.0 \pm 0.1$	$-6.66 \pm 0.09$
05_11	$678.1 \pm 0.7$	$-49.54 \pm 0.07$	$724.9 \pm 0.4$	$-5.97 \pm 0.31$
07_B3	$678.6 \pm 0.9$	$-54.74 \pm 0.10$	$723.1 \pm 0.2$	$-9.34 \pm 0.08$
07_A3	$677.9 \pm 0.5$	$-56.97 \pm 0.03$	$721.4 \pm 0.5$	$-9.26 \pm 0.08$
07_16	$677.3 \pm 0.9$	$-57.86 \pm 0.04$	$719.9 \pm 0.05$	$-11.55 \pm 0.65$
08_06	$683.2 \pm 0.3$	$-53.96 \pm 0.03$	$722.6 \pm 0.1$	$-5.55 \pm 0.57$
09_06	$677.0 \pm 0.4$	$-58.84 \pm 0.19$	$721.9 \pm 0.2$	$-8.46 \pm 0.03$

Table 6: Determined onset temperatures of the glass transition, the onset temperature of the crystallisation event and enthalpies of crystallisation and structural relaxation. DSC measurements were executed at 20 K/min.

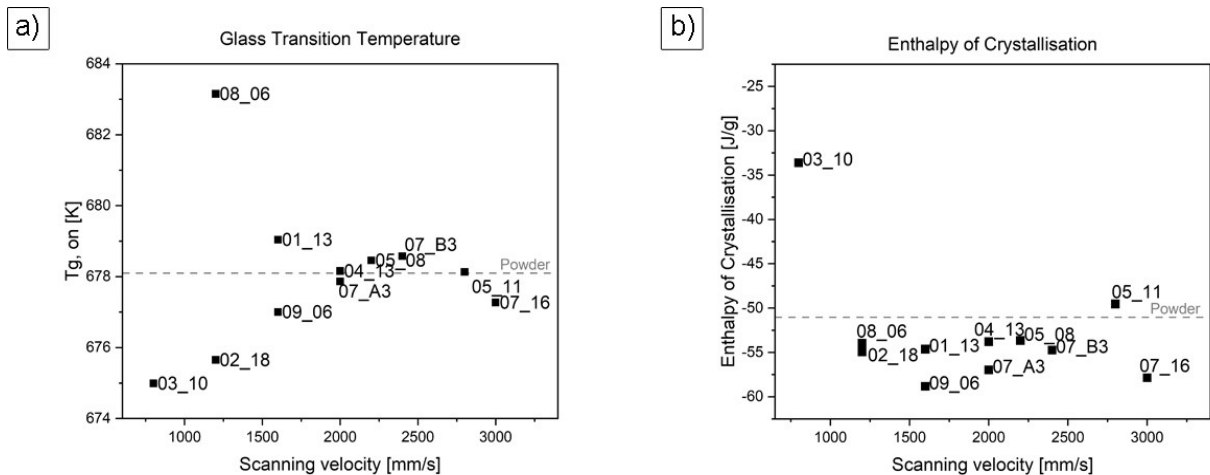


Figure 25: a) Glass transition temperature ( $T_{g,on}$ ) as a function of the used scanning velocity. b) Enthalpy of crystallisation ( $\Delta H_x$ ) as a function of the used scanning velocity. Values of  $T_{g,on}$  and  $\Delta H_x$  can be found in Table 6. The data points are labelled with the samples' identification.

#### 4.2.4. Indentation Tests and Vickers Hardness

Micro-indentation measurements were conducted at various samples with a layer thickness of 0.05 mm and a hatching of 0.10 and 0.20 mm in order to investigate the influence of different parameters on the mechanical properties. The results are shown in Figure 26a and b. The measured values of the indentation hardness hardly differ with the used energy density and the different hatching. The average indentation hardness is  $587 \pm 11$  HV<sub>IT</sub> and  $578 \pm 3$  HV<sub>IT</sub> for a hatching of 0.10 and 0.02 mm, respectively. For the indentation elastic modulus, a slight increase with the used energy density was found for both hatchings (Figure 26b). To gather more information about the interrelation between the process parameters and the indentation elastic modulus, the latter is plotted as a function of the used scanning velocity (Figure 26c). The data points in this figure are labelled with the used laser power. It becomes clear that within one used scanning velocity there is an increase in the elastic modulus when the used laser power is increased, i.e. the energy density is increased. Furthermore, an increase in the indentation elastic modulus is achieved by holding the laser power constant and decreasing the scanning velocity. This finding corresponds to the one of the DSC measurements. Since samples produced with higher scanning speed and lower power are less relaxed, they exhibit lower elastic constants [3]. To compare the samples 03\_10 ( $P = 140$  W,  $v = 1600$  mm/s,  $E = 17.50$  J/mm<sup>3</sup>,  $h = 0.20$  mm) and 01\_13 ( $P = 140$  W,  $v = 800$  mm/s,  $E = 17.50$  J/mm<sup>3</sup>,  $h = 0.10$  mm) once more, they are highlighted in Figure 26 with a green and a blue data point. While sample 03\_10 exhibits an indentation elastic modulus of  $101.39 \pm 1.42$  GPa, the one of sample 01\_13 which was built with higher speed, is  $104.39 \pm 0.95$  GPa.

For the determination of the appropriate load for Vickers hardness measurements, micro-indentation measurements on sample 01\_13 were carried out with varied loading forces. In Figure 27, the measured indentation hardness and the indentation elastic modulus are shown. A plateau value of  $\sim 550$  HV and  $\sim 90$  GPa is reached when a maximum loading of 20 – 30 N is used in the indentation measurement. Below, an increase in both the hardness and the elastic modulus is visible. Therefore, a loading of 5 kgf (49 N) was defined for the Vickers hardness measurements to ensure the exclusion of indentation size effects. To illustrate the connection between the shown plots, the data points belonging together are highlighted in blue.

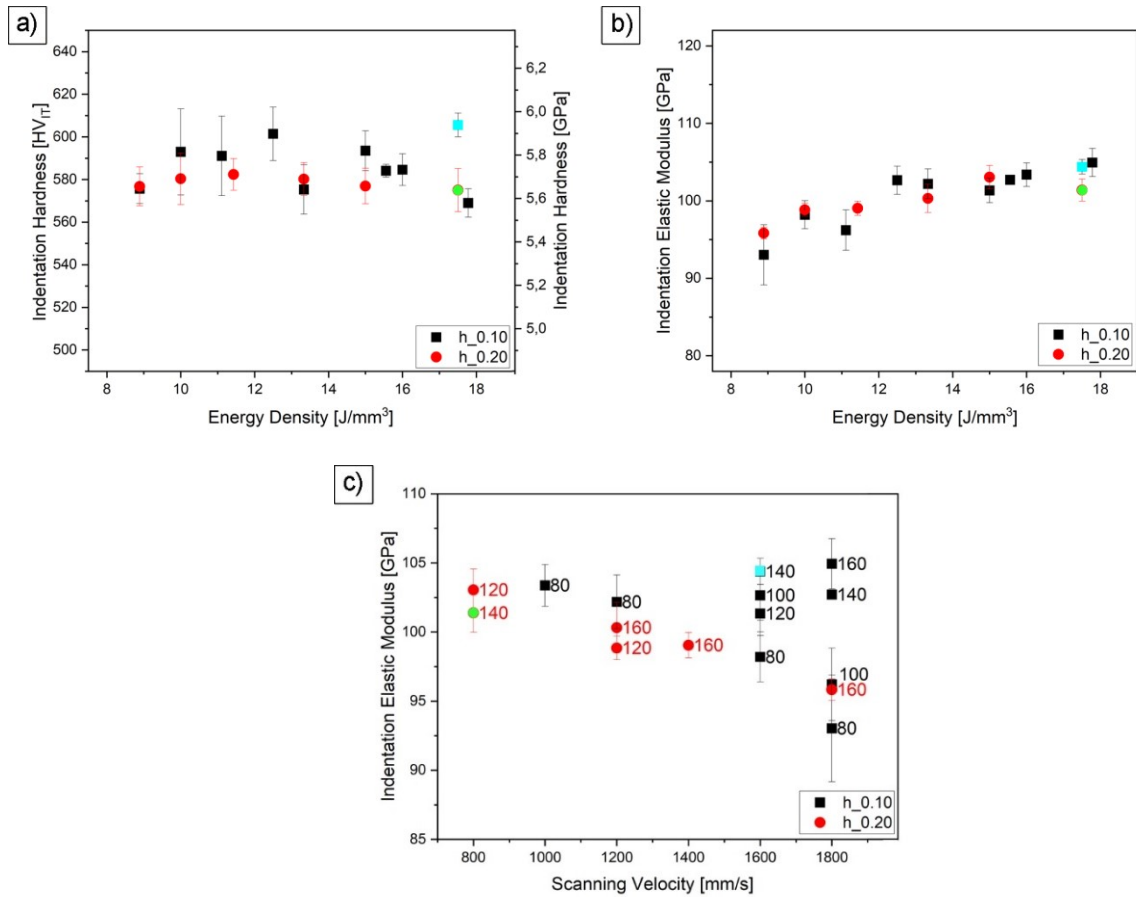


Figure 26: Results of the indentation measurements at various samples of the parameter study produced with a layer thickness of  $t_{s1} = 0.05$  mm. a) Indentation hardness and b) indentation elastic modulus as a function of the used energy density; c) Indentation elastic modulus as a function of the used scanning velocity. Data points are labelled with the used laser power. Samples 03\_10 and 01\_13 are highlighted in green and blue, respectively.

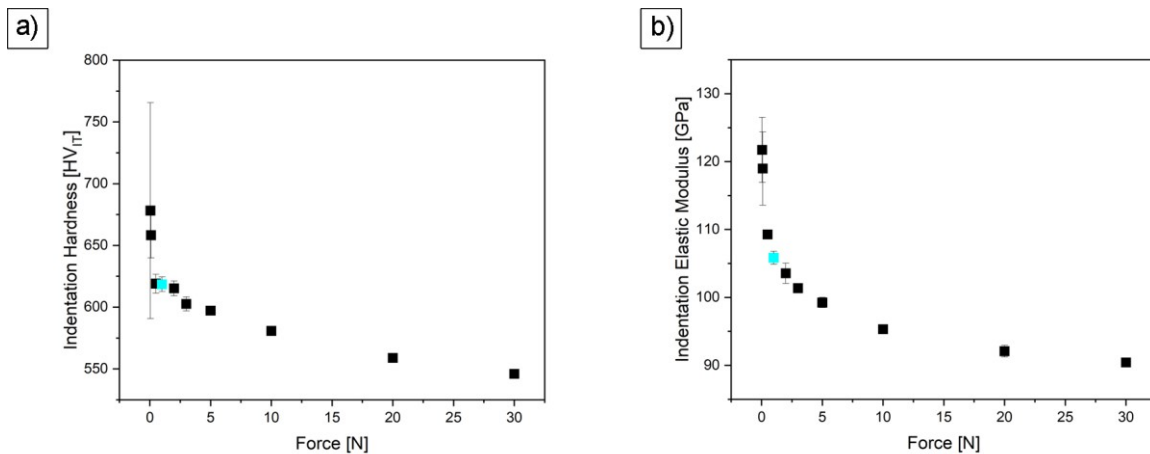


Figure 27: a) Indentation hardness and b) indentation elastic modulus of sample 01\_13. The data point in blue marks the force of 1 N, which was used for the above shown micro-indentation measurements.

In Table 7 the average hardness values (HV5) of various samples of the SLM parameter study are listed. In order to obtain the hardness of the bulk material, measurements were only carried out on the densest samples exhibiting a layer thickness of  $ts_1$ . For the measurements of samples with layer thickness  $ts_2$ , a few more samples were measured. This was done to investigate whether the hardness of the samples varies with different used process parameters or remains stagnant. One can see that the average hardness of the samples does not differ immensely. This is in good accordance with the micro-indentation measurements, where the values of the indentation hardness hardly differ as well. Also a correlation between the used process parameters and the average hardness could not be observed in these measurements. However, differences in the hardness were detected between the yz-plane and the xy-plane (Figure 28a) and along the z-axis while measuring on the yz-plane. Consequently, it can be possible that the layer-wise building in z-direction has an impact on the mechanical properties of the SLM-fabricated BMG. Especially the formation of the melt pools as shown in Figure 21, can influence the measured hardness. Additionally, the complex thermal procedures taking place during the building of the BMG sample can affect the atomic structure, and can thus change the hardness at various positions in the sample. However, these complex phenomenon will not be further discussed within the scope of this thesis.

Although there are differences in the hardness values, the average values of all SLM-fabricated samples are lower than the values of 540 HV5 and  $517 \pm 5$  HV0.3 given in [11] and [51], respectively. To compare, the Vickers hardness (HV0.1) was additionally determined from the indents of the micro-indentation measurements with the CSM indentation software. The values of the measured samples are all above 500 HV0.1 (Figure 28b). However, it should be noted that in this case, a smaller area of the sample was measured. While the estimated diagonal of the Vickers hardness measurement indent is 131  $\mu\text{m}$ , the one of the micro-indentation measurements is only 18  $\mu\text{m}$ . Therefore, microstructural inhomogeneities, such as small pores, do not influence or rather reduce the HV0.1 values. Moreover, the indentation measurements were carried out automatically and potential human measurement errors may be minimised in this case.



Layer Thickness $ts1 = 0.05$ mm		
Sample	Energy Density [J/mm <sup>3</sup> ]	Hardness [HV5]
01_13	17.50	491 ± 9
02_18	17.78	482 ± 4
03_10	17.50	478 ± 5
04_13	15.00	481 ± 3
05_08	15.15	481 ± 2

Layer Thickness $ts2 = 0.02$ mm		
Sample	Energy Density [J/mm <sup>3</sup> ]	Hardness [HV5]
07_A1	25.00	471 ± 3
07_A3	25.00	475 ± 5
08_02	20.00	479 ± 7
08_04	25.00	473 ± 8
08_06	33.33	489 ± 7
09_01	31.25	472 ± 5
09_02	31.25	474 ± 6
09_05	20.83	480 ± 1
09_06	31.25	475 ± 7

Table 7: Average hardness values of various samples of the SLM parameter study.

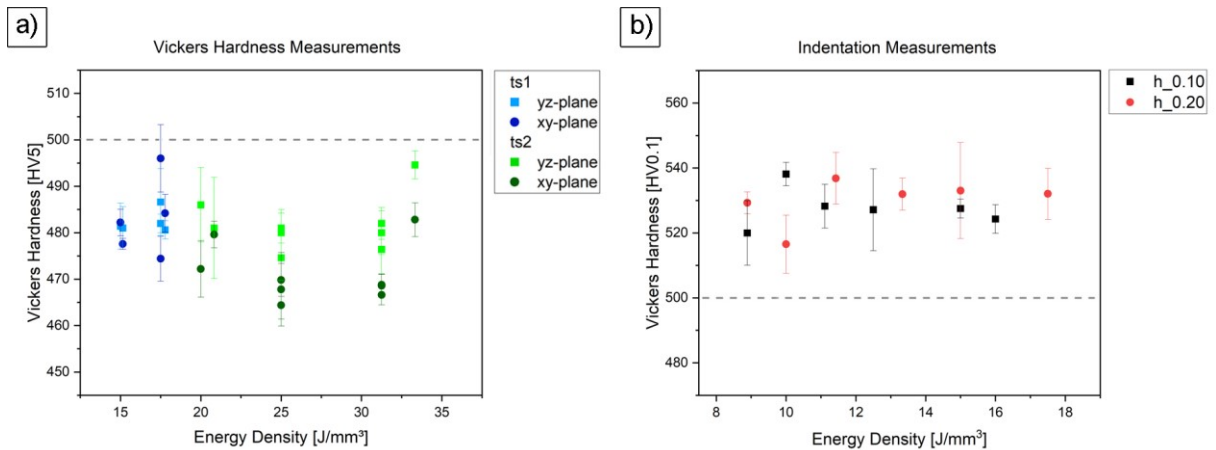


Figure 28: a) Vickers hardness (HV5) of the SLM-fabricated samples manually measured on the yz-plane compared to the values manually measured on the xy-plane. b) Vickers hardness (HV0.1) measured from the indents of the instrumented micro-indentation measurements. In comparison to the HV5 values, the measured samples exhibit a hardness above 500 HV0.1.

### 4.3. Building of Tensile Test Samples

Cylindrical samples and tensile test samples were built in order to check the Zr-based BMGs behaviour when printing a geometry different to a 1 cm x 1 cm x 1 cm cube. It has to be mentioned that the dimensions of the base area are not the only difference. The samples' height ( $H = 85$  mm) also differs strongly from the cubes' height. A picture of the as-built cylindrical samples together with cubes and hexagonal platelets on the building platform is shown in Figure 29a. It is visible that the built cylinders and tensile test samples have a blueish annealing colour in the upper parts of the samples. However, not all samples exhibit the same amount of colouring. There is a dependence on the samples' exact location on the building platform. While the outer samples at the margin exhibit less colour, the ones situated in the middle are more blueish. In Figure 29b, a picture of samples removed from the middle are presented. Even here, a difference with regard to the beginning of the blueish colour is observable. The occurrence of the annealing colour can be explained by the great height of the sample. Since the thermal conductivity of the Zr-based BMG is not very high ( $\lambda \approx 2.5$  W/mK [11]), the developed heat due to the repetitive scanning of the laser cannot be conducted downwards fast enough. Therefore, a heat accumulation takes place in the upper part of the sample and the temperature increases there. In combination with the residual oxygen, a thin oxide layer with a blueish colour evolves.

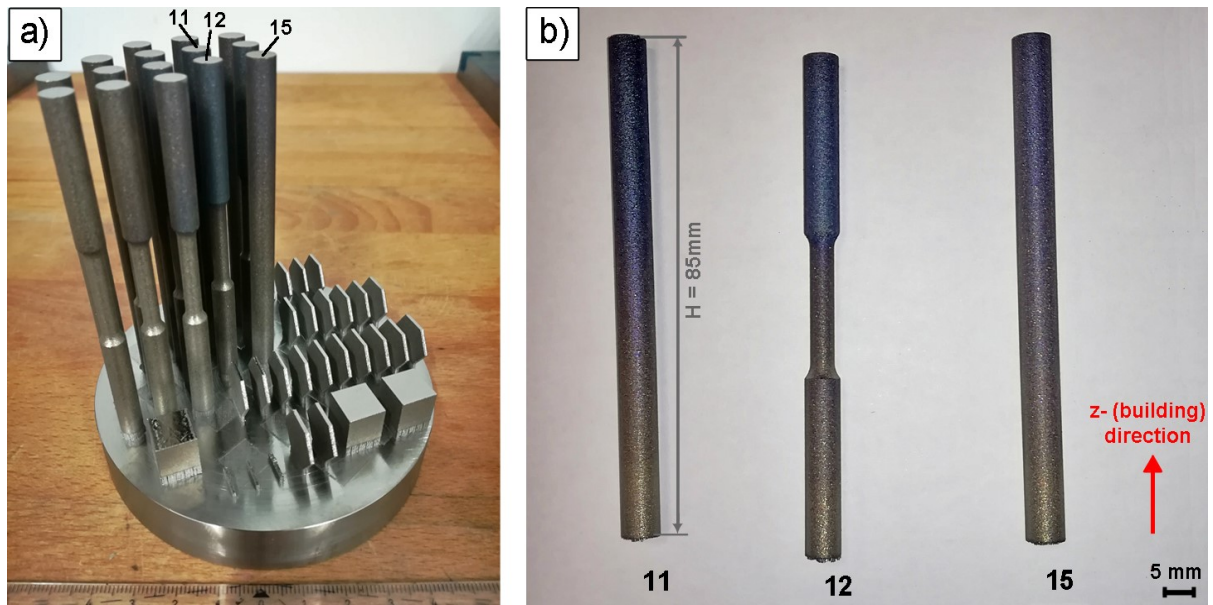


Figure 29: a) Photographs of as-built samples on the building platform. The higher tensile test and cylindrical samples show a blueish annealing colour. Differences in the starting point of the colouring can be seen between samples at the margin and the ones in the middle. b) removed samples, the blueish oxide layer in the upper part of the sample is well visible.

In order to verify if the occurring heat accumulation also has an influence on the microstructure, sample number 11 was cut and analysed by XRD. XRD patterns of slices from the bottom ( $z = 0$ ), the top ( $z = H = 85$  mm), and from in the middle ( $z = \frac{1}{4} H$ ,  $z = \frac{1}{2} H$ , and  $z = \frac{3}{4} H$ ) were taken (Figure 30). It is evident that the critical cooling rate of the BMG could not be achieved between  $x = \frac{1}{2} H$  and  $x = \frac{3}{4} H$  and partial crystallisation took place in these parts of the sample. Furthermore, there is a gradient in the amount of crystallisation. This fits to the assumed heat accumulation which evolves during the ongoing building process. The decreased amount of crystallisation at the top of the sample can be explained by the fact that the last-built layers were measured. A chance to cool down via radiation to the top is given, since hardly any or no layers are further built on there.

The crystalline peaks which are superimposed to the broad scattering maximum of the amorphous phase correspond to the big cube phase ( $\text{NiTi}_2$ -type,  $\text{Fd}\bar{3}\text{m}$ ), a metastable fcc intermetallic compound found in Zr-based metallic glasses [29, 52].

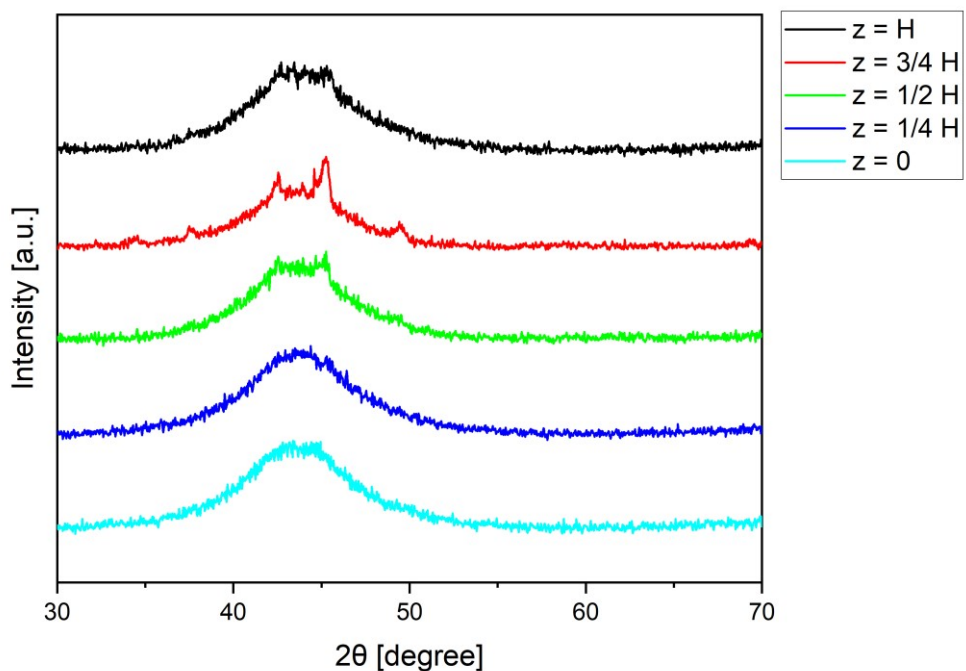


Figure 30: XRD pattern of the investigated cylindrical sample with the number 11 at different  $z$ -positions. Partial crystallisation took place in the upper parts of the sample.

## 4.4. Influence of a Post Processing

Further cubic samples and hexagonal platelets, produced with the process parameter set of cube 08\_06 ( $E = 33.33 \text{ J/mm}^3$ ,  $P = 80 \text{ W}$ ,  $h = 0.10 \text{ mm}$ ,  $v = 1200 \text{ mm/s}$ ,  $ts2 = 0.02 \text{ mm}$ ), were used to study the influence of a post processing on the BMGs' properties. Heat treatments after the SLM process were carried out to modify the thermodynamic state of the SLM-fabricated BMG on the one hand. On the other hand, different surface treatments on the as-built samples were executed.

### 4.4.1. Influence of a Heat Treatment

In Table 8 the gravimetrically and optically determined densities of the as-built cubic samples (Cube 1 - 3) produced with the process parameter set of sample 08\_06 in an additional building job are given. The densities of the subsequently heat-treated cubes are listed in the table as well. There is no difference in the densities measured by means of the Archimedean principle of the as-built cubes. This indicates that, within the building job, the cubes are nearly identical. However, there is a variation between the density of the cubes fabricated in the further building job and the investigated cube from the parameter study (compare values of sample 08\_06 in Table 4). Especially the values of the optically determined density of the cubes of the further building job are considerably different. This confirms that in these cubes, there are definitely more pores present (Figure 31). The reason for the variation is not clearly understood yet, since there are many factors which can affect the SLM process. Nevertheless, a very straight-forward assumption is that an aging or more precisely a moisture absorption of the powder happened because of a higher ambient relative humidity, which consequently impaired the quality of the SLM process. However, a relative density higher than 99.5% is still considerable.

Due to the heat treatment below the glass transition temperature, structural relaxation and a reordering of the atoms into an energetically more favourable state take place. Therefore, a slight increase of the samples density by 0.1% - 0.15% is expected [53]. Even if there is an increase in the relative density determined by the Archimedean Principle (Table 8), the values are in the range of the standard deviation of the measurements. As a result, no explicit increase can be detected with regard to the heat treating below the glass transition temperature.

The reported density increase for a Zr-based BMG due to crystallisation is more than the density increase due to structural relaxation (0.44%) [53]. However, the measured relative density of Cube 3 after the heat treatment above the crystallisation temperature is  $101.35 \pm 0.06 \%$ , which is considerably more than an increase of 0.44%. An

explanation for this can be the formed oxidation layer on the cube due to the heat treatment, which was not removed before the density measurement.

<b>As-built samples</b> <i>Parameter set 08_06</i>	<b>Cube 1</b>	<b>Cube 2</b>	<b>Cube 3</b>
Absolute density (Archimedes) [g/cm <sup>3</sup> ]	6.569 ± 0.002	6.571 ± 0.002	6.571 ± 0.003
$\rho_{\text{rel,archimedes}}$ [%]	99.53 ± 0.03	99.56 ± 0.04	99.56 ± 0.03
$\rho_{\text{rel,optical}}$ [%]	99.470 ± 0.050		
<b>Heat-treated samples</b>		<b>650K for 60 minutes</b>	<b>850K for 60 minutes</b>
Absolute density (Archimedes) [g/cm <sup>3</sup> ]		6.573 ± 0.003	6.689 ± 0.003
$\rho_{\text{rel,archimedes}}$ [%]		99.60 ± 0.04	101.35 ± 0.06
$\rho_{\text{rel,optical}}$ [%]		99.364 ± 0.147	99.704 ± 0.060

Table 8: Densities of the cubic BMG samples produced with the process parameter set of sample 08\_06 in an additional building job. The densities of the subsequently heat-treated samples are given as well.

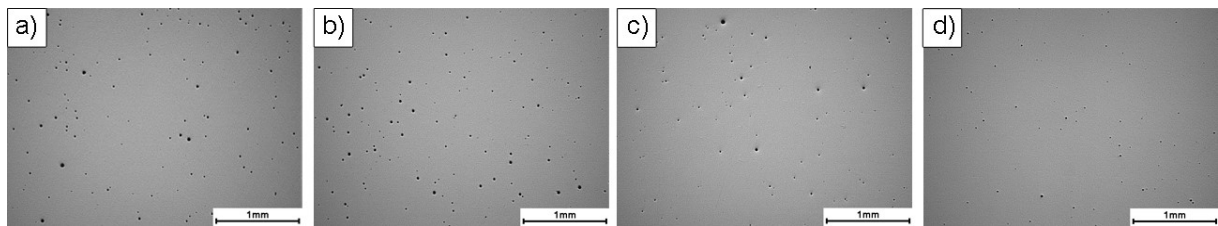


Figure 31: LOM micrographs of the *yz*-plane from cubes fabricated with the selected parameter set 08\_06 compared to the micrograph taken from the cube of the parameter study. a) Cube 1 (as-built), b) Cube 2 (heat-treated at 650 K for 60 minutes), c) Cube 3 (heat-treated at 850 K for 60 minutes), d) Sample 08\_06 of the parameter study.

The XRD pattern of the annealed cubic samples and the as-built cube are shown in Figure 32a. It is visible that the sample, which was annealed below the glass transition temperature (at 650 K for 60 min, curve b), is still XRD-amorphous. However, the heat treatment above the crystallisation temperature (at 850K for 60min, curve c) results in a sample which shows some crystalline peaks in its XRD pattern. Consequently, it points out that in the amorphous microstructure are some (nano-)crystals are present. Due to the reflections positions it can be assumed that the big cube phase (NiTi<sub>2</sub>-type,  $Fd\bar{3}m$ ) is present in the material once again (compare Section 4.3). Nevertheless, Bragg peaks might also belong to the hexagonal Zr<sub>6</sub>NiAl<sub>2</sub> phase, which was detected after an annealing treatment of a melt-spun amorphous Zr-Cu-Ni-Al-Ti-ribbon [52]. As reported in [29] and [52], further phases like CuZr<sub>2</sub> or CuZr can also be present in a crystallised Zr-Cu-Ni-Al-Ti metallic glass [29]. Since in a multicomponent system, such

as the chosen BMG, many variants of crystallisation products are possible, an unequivocal allocation of the reflection peaks is difficult [3]. Additionally, the numerous reflections of the possible phases are close together or even overlap each other, which hampers the allocation as well.

In Figure 32b, DSC curves of samples prepared from Cube 1 (as-built) and Cube 2 (heat-treated at 650 K) are shown. The influence of the heat treatment below the glass transition temperature is clearly visible. Compared to the curve of the powder and the one of Cube 1 the heat-treated cube exhibits a significantly smaller exothermic relaxation peak. Even if there is no observed difference in the density of the sample, the DSC measurement confirms that structural relaxation of the material takes place. Nonetheless, a fully relaxed BMG could not be achieved by the selected heat treatment.

Vickers hardness measurements were carried out in order to obtain initial information about the BMGs mechanical properties and about the different heat treatments' impact on the hardness. The average values of the Vickers Hardness are given in Table 9. In the table the average hardness values of the individual investigated planes are listed as well. The as-built cubes and the cube heat-treated at 650 K exhibit an average hardness which is in the same range. While Cube 1 and the cube of the parameter study has a hardness of  $484 \pm 5$  HV5 and  $489 \pm 7$  HV5, the average hardness value of the structurally relaxed cube (Cube 2) hardly differs from the two as-built cubes. Nonetheless, a slight increase can be seen, when comparing the values of the individual planes. As mentioned above, the higher hardness of the yz-plane, especially found in the cube of the parameter study, might originate from the formation of melting pools and from the layer-wise building in z-direction. Due to the repeated energy input of the laser and the increasing heat of the built BMG sample, the cooling rate is slower and structural relaxation can take place in the upper parts. This results in an increased hardness in the sample which increases the average hardness value of the yz-plane as well. Since the hardness of the xy-plane is measured within a layer which is always situated in the cubes' middle (Figure 10a), the structural relaxation effect can be neglected. Therefore, if one compares the hardness values of the xy-planes, the influence of the heat treatment can directly be seen. An increase of around 100 HV is observed for the hardness of the crystallised sample ( $594 \pm 7$  HV5).

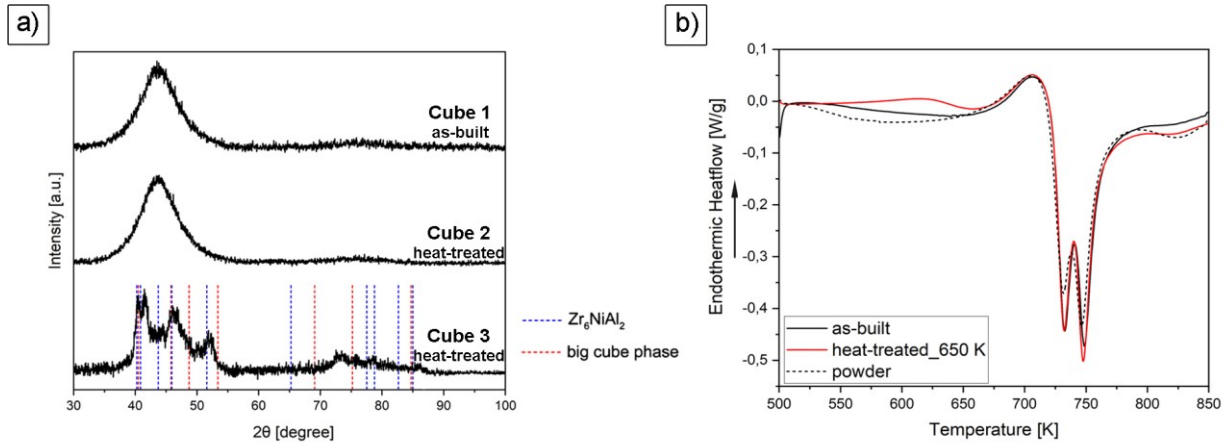


Figure 32: a) XRD pattern of the as-built cube (Cube 1) and the at 650 K and 850 K heat-treated cubic sample (Cube 2 and Cube 3, respectively); the positions of the reflections of  $Zr_6NiAl_2$  [54] and the big cube phase [55] are marked as dotted lines. b) DSC curves of samples prepared from Cube 1 and Cube 2 compared to the DSC curve of the used powder.

	Cube 1 as-built	Cube 2 annealed at 650 K for 60min	Cube 3 annealed at 850 K for 60min	Cube of the Parameter Study- as-built
average HV5	484 ± 5	494 ± 3	594 ± 7	489 ± 7
HV5 (xy-plane)	482 ± 3	493 ± 3	590 ± 4	483 ± 4
HV5 (yz-plane)	485 ± 5	495 ± 1	600 ± 7	495 ± 3

Table 9: Vickers Hardness (HV5) of cubes in different thermodynamic states.

#### 4.4.2. Influence of a Surface Treatment

Examples of the as-built hexagonal platelets with different surface treatments compared to a platelet without a subsequent surface treatment are shown in Figure 33. From the micrographs, it becomes clear that the surface treatment changes the appearance of the different samples. While the surface of the as-built sample appears rough (Figure 33a), the glass blasted one is much smoother and shinier (Figure 33d). The sample blasted with corundum exhibits a smooth surface as well, however, the appearance is more matt (Figure 33g). Details of the different surfaces are also presented in Figure 33. The adherent particles and the layer-wise structure from the SLM process can be seen in the micrographs of the as-built sample (Figure 33b and c). These features are not visible anymore in the micrographs of the surface treated samples. It is noticeable that the surfaces of the treated samples are more homogenous with less coarse asperities. However, a difference between the different blasting treatments is evident, especially in the highly magnified micrographs. The glass blasted samples surface is more flat than the corundum blasted one. This



explains the shinier surface of the samples treated with glass beads. In Figure 33i, a bright particle, marked with an arrow, is apparent. This is most likely an implanted corundum particle, but details to these investigations can be found a little further on in this chapter.

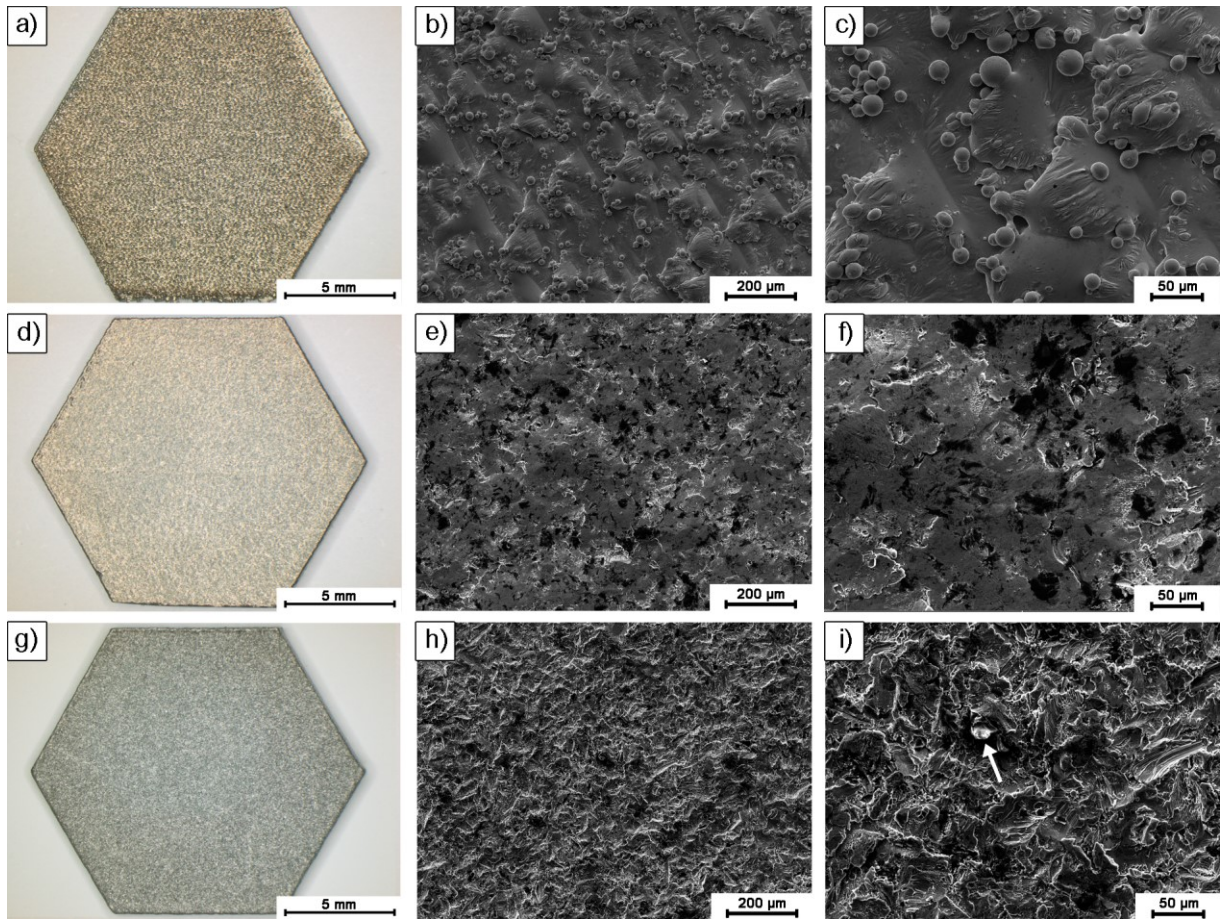


Figure 33: Micrographs of the as-built hexagonal platelets with different surface treatments: a-c) platelet without a subsequent surface treatment, d-f) glass blasted platelet, g-i) corundum blasted platelet.

The surfaces of the samples which were heat-treated at 650 K before the surface treatment looked almost the same. However, the crystallised samples showed a completely different behaviour during the glass blasting. Since the heat treatment results in an embrittlement of the samples, a lot of material was removed during the surface treatment. Thus, the samples surfaces exhibit an extremely furrowed surface with numerous asperities (Figure 34). Additionally, the samples broke during the blasting process as seen in Figure 34a. In the detailed SEM micrograph in Figure 34c, the difference of the materials' behaviour is evident. Because of the bombardment with the glass microbeads in combination with the embrittlement of the crystallised BMG, material fragments broke out by cleavage and smooth fracture surfaces were formed there.



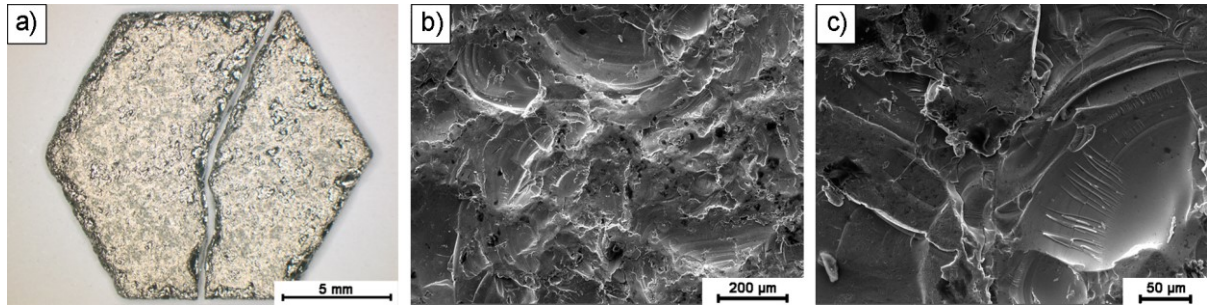


Figure 34: Micrographs of the crystallised hexagonal platelet after the blasting treatment with glass microbeads.

In Figure 35, the arithmetical mean roughness values ( $R_a$ ) and the mean roughness depth ( $R_z$ ) of the various samples are shown. Therein, the values of different combinations of the post processing are compared (different heat treatments combined with different surface treatments). The exact roughness values of the combinations are listed in Table 10. The values are in line with the results of the optical observations. The samples without a surface treatment exhibit a higher roughness than the surface treated ones. While the  $R_a$ -value of the as-built samples is in the order of  $7 \mu\text{m}$ , the values of the surface treated samples are reduced by at least a half. It has to be mentioned that the subsequent heat treatment at  $650 \text{ K}$  does not affect the samples' roughness. Even if there is a slight reduced  $R_a$ -value for the sample which was heat-treated at  $850 \text{ K}$ , the  $R_z$ -value of the sample does not differ from the others. Furthermore, the surface roughness of the glass blasted sample is smoother than the samples surface blasted with corundum. However, if one compares the roughness values of the blasted samples which were not heat-treated with the values of samples which were heat-treated at  $650 \text{ K}$ , there is not a real difference. Therefore, the structural relaxation of the BMG does not affect the subsequent blasting treatment strongly, no matter whether it is carried out with glass beads or with corundum. However, the surface roughness of the crystallised sample is not reduced by the surface treatment. In fact, the opposite occurred: the roughness increases due to the splitting-off of the brittle material, which could already be seen before with the microscope.

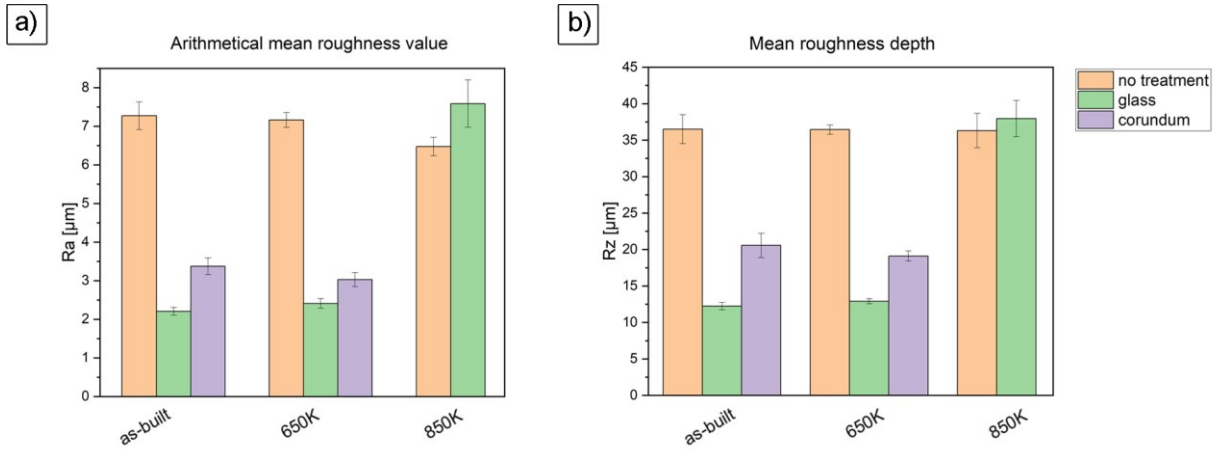


Figure 35: Roughness values of the samples with different combinations of the post processing compared in diagrams. a) Arithmetical mean roughness values (Ra) and b) Mean roughness depth (Rz) of the samples.

Arithmetical mean roughness value - Ra [μm]			
	As-built	650K for 60 minutes	850K for 60 minutes
No treatment	7.271 ± 0.359	7.161 ± 0.192	6.476 ± 0.241
Glass blasted	2.205 ± 0.100	2.409 ± 0.127	7.587 ± 0.613
Corundum blasted	3.374 ± 0.219	3.028 ± 0.182	
Mean roughness depth - Rz [μm]			
	As-built	650K for 60 minutes	850K for 60 minutes
No treatment	36.502 ± 1,978	36.447 ± 0.648	36.306 ± 2.353
Glass blasted	12.229 ± 0.517	12.905 ± 0.361	37.948 ± 2.498
Corundum blasted	20.567 ± 1.663	19.105 ± 0.698	

Table 10: Values of the measured roughness of samples with different post processing.

Due to the bombardment with the glass microbeads and corundum particles, pieces of the blasting material can also be implanted in the samples' surfaces. Therefore, the samples were investigated with the SEM and EDX measurements were carried out. In Figure 36 the micrographs and some results of the EDX measurements of the as-built sample, which was glass blasted are shown. The secondary electron (SE) micrograph, the back scattered electron (BSE) micrograph, the to the micrographs corresponding EDX map, and a representative result of the EDX spot measurement are shown in the figures a-d, respectively. In the BSE micrograph the position where the EDX spot measurement were executed is marked with a red cross. In Figure 37, the same results are shown for the as-built sample which was blasted with corundum. In both samples, fragments of the respective blasting material can be seen. These fragments are well detectable when using the BSE detector. They appear in black due to the comparative small atomic number of the containing elements. However, if one compares the BSE micrographs with the SE ones, particles can be seen as well. The EDX maps prove the observations with the SE- and BSE detector. At precisely the locations where particles are presumed, typical elements which are present in glass (silicon, oxygen, sodium, and calcium) and corundum (aluminium and oxygen), can be detected on the surfaces. In Figure 37a, a particle can clearly be seen. Together with all the investigation tools, it is confirmed that it is a corundum particle from the blasting treatment. Therefore, one can conclude that the particle seen in Figure 33i is a corundum one as well. It is important to bear in mind that even if aluminium is a constituent of the used Zr-based BMG, an allocation to corundum particles can be made unequivocal since an accumulation of aluminium exists at the positions where particles are presumed to be. Additionally, considerable more oxygen can be detected at those positions. In the glass blasted sample, these circumstances are not present since the elements silicon, oxygen, sodium, and calcium are not constituents of the used BMG alloy.

The blasted samples, which were heat-treated at 650 K before, were also investigated. However, no obvious differences compared to the as-built samples could be observed. Again, the typical elements of the blasting material could be detected. Furthermore, there was no pronounced difference in the proportion of implanted particles.

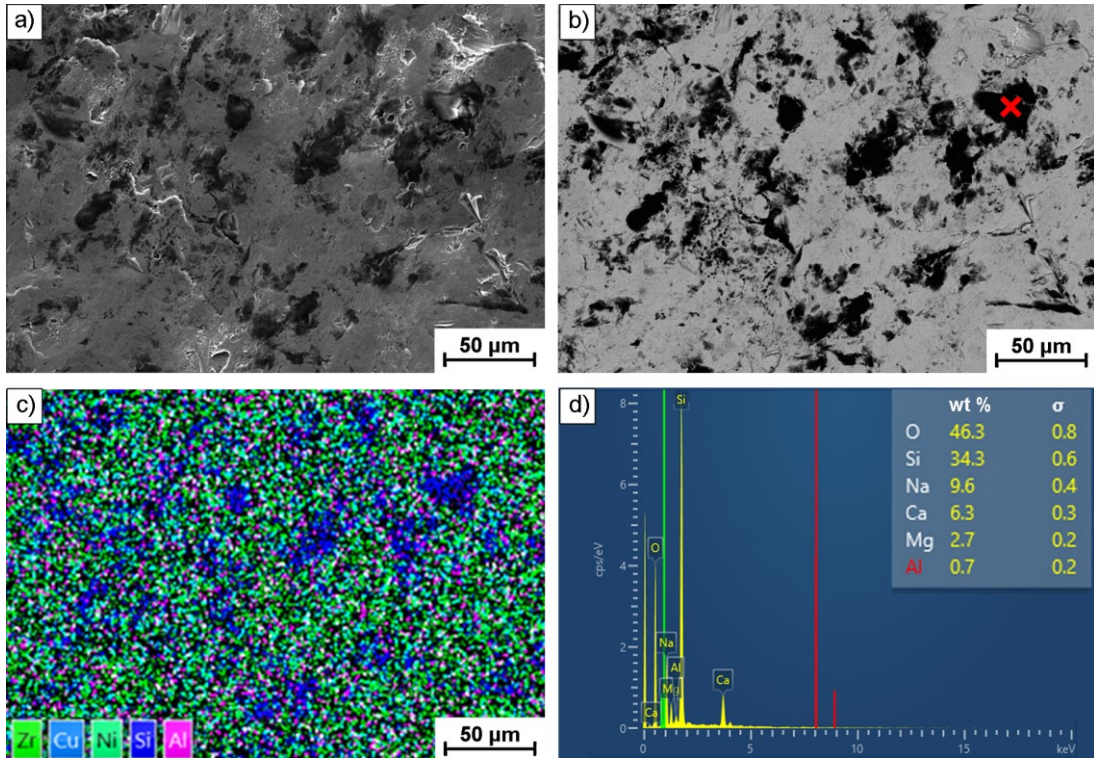


Figure 36: a) SE micrograph b) BSE micrograph c) corresponding EDX map and d) result of the EDX spot measurement (marked in the BSE micrograph) of the glass blasted sample's surface.

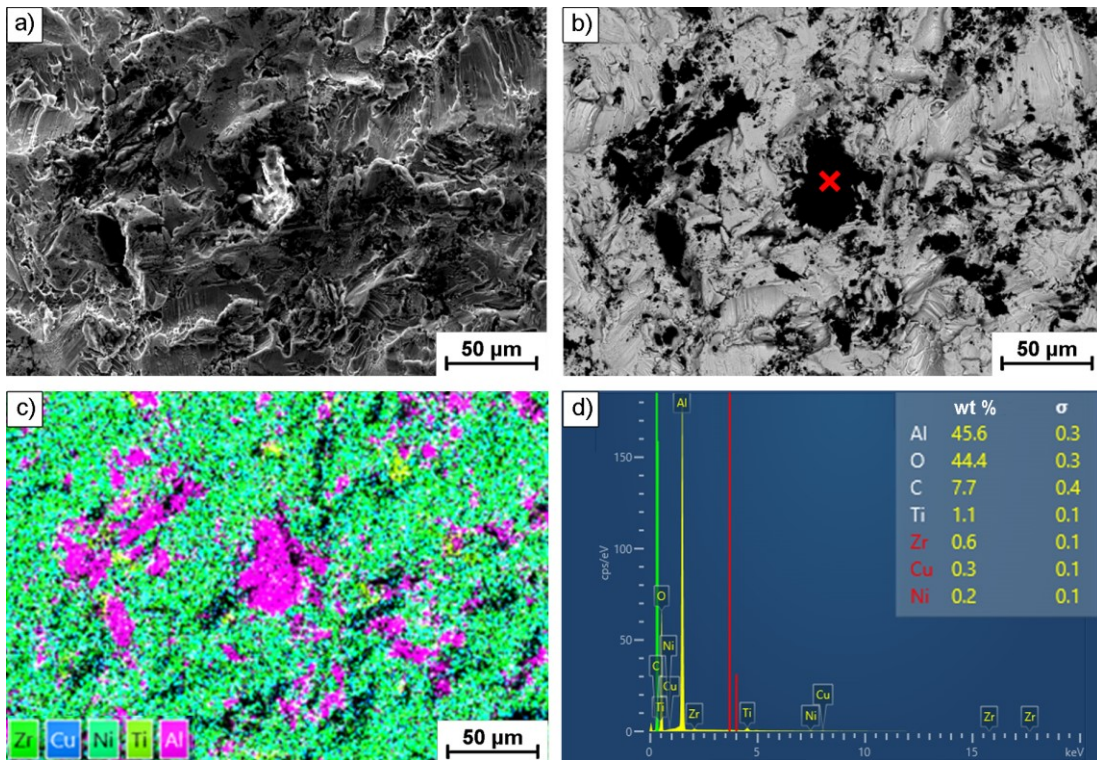


Figure 37: a) SE micrograph b) BSE micrograph c) corresponding EDX map and d) result of the EDX spot measurement (marked in the BSE micrograph) of the corundum blasted sample's surface.



#### 4.5. 4-Point Bending Tests

Mechanical behaviour of SLM-fabricated samples produced with the parameter set 08\_06 was investigated using 4-point bending tests. Samples built in vertical and horizontal direction were tested in various directions after carrying out different kinds of post processing (Table 2).

Since the building of the tensile test samples results in partial crystallisation and the height,  $H_s$ , of the bending test samples is also greater than the cubes', the building strategy for these samples was changed. Additionally, these samples were placed on the building platform with a considerable larger distance to one another in order to avoid the heat built-up (Figure 38b). However, to ensure that any crystallisation in the upper part of the sample evolved during the SLM process, XRD measurements were executed on one sample. The measurements were performed in the same manner as for the cylindrical sample (Section 4.3). The XRD pattern of the measurements are depicted in Figure 38a. Since all the XRD patterns show a broad maximum, it can be assumed that the samples are amorphous.

For the samples built horizontally, a new situation occurred. After removing the samples from the building platform, a bending up of the sample was observable. This can be referred to internal stresses which evolved during the SLM-process. The bend up was optically measured on one embedded and metallographically prepared sample. A value of approximately  $140\ \mu\text{m}$  was obtained for the difference between the samples top edge in the middle and the upper most points of the samples' corners (Figure 38b). Because of this form change, the samples were tested in different orientations:  $H0^\circ$ ,  $H180^\circ$  and  $H90^\circ$  (Figure 39).

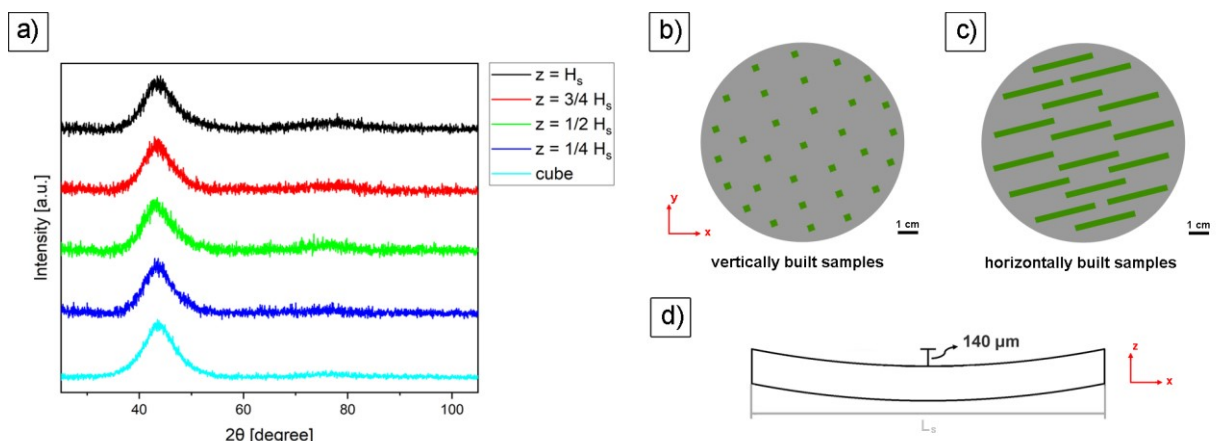


Figure 38: a) XRD pattern of the vertically built bending test sample, b-c) arrangement of the samples on the building platform, d) schematic drawing of the bend up of the horizontally built sample

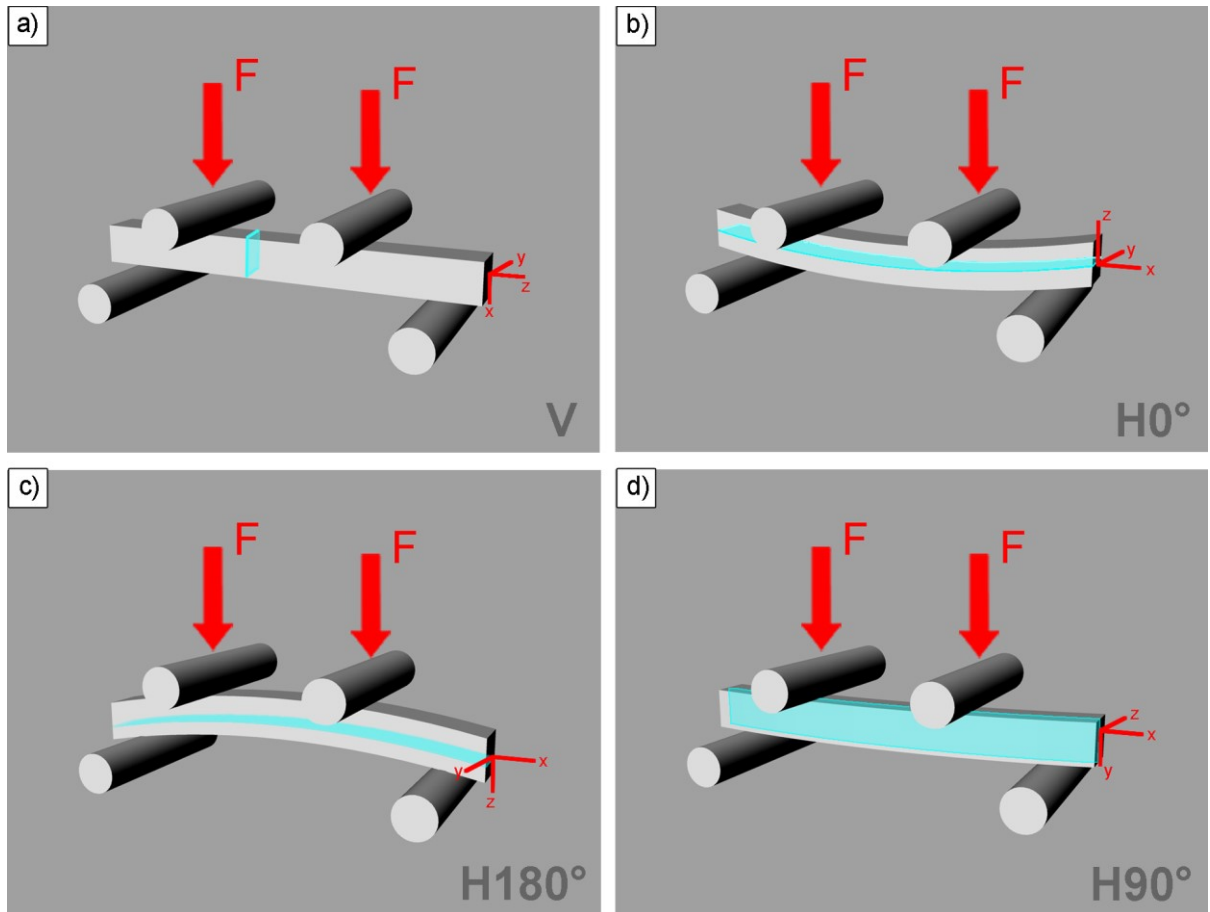


Figure 39: Executed testing orientations within the different test series of 4 point bending tests: a) testing of vertically built samples, testing orientation V; b-d) testing of the horizontally built samples, testing orientations H0°, H180°, and H90°, respectively. The orientation of the layers in the samples are drawn in blueish green.

Stress - displacement curves of various selected samples of the different test series are shown in Figure 40. A summary of the determined average values (flexural strength and maximum bending displacement) is given in Table 11. Generally the bend testing of the SLM-fabricated samples showed the characteristic mechanical behaviour of a BMG as described in the theoretical part (Section 2.1.3). For all samples hardly any macroscopic plastic deformation could be observed.

The glass blasted samples tested in the 1<sup>st</sup> test series reached the highest average flexural strength ( $1741 \pm 119$  MPa). However, the average flexural strength of the samples blasted with corundum is higher than the average value of the as-built samples ( $1698 \pm 57$  and  $1078 \pm 98$  MPa, respectively). Consequently, the surface treatment, whether the glass or the corundum blasting, has a positive effect on the flexural strength. Another significant difference between the samples' curves of this test series is the slope. At the same stress value, all the as-built samples show a greater displacement compared to the surface-treated samples. This has a macroscopic reason: the powder particles adherent on the surface of the as-built samples are easily squeezed when force is applied (Figure 41a). However, due to the smooth surface of the surface-treated samples, this effect does not occur and consequently less displacement is measured for these samples.

The 4-point bending test curves of chosen vertically built samples in different thermodynamic state (2<sup>nd</sup> test series) are shown in Figure 40b. In this test series, the flexural strength of the glass blasted samples in as-built condition is  $2041 \pm 446$  MPa. Compared to the flexural strength of glass blasted samples of the 1<sup>st</sup> test series, this is higher, however the deviation is larger ( $\sim 500$  MPa). When comparing the individual flexural strength values (Appendix, Section 1.5.1), it is noticeable that one sample (sample 13) exhibits a considerably lower flexural strength of 1081 MPa. It is possible that in this sample there was a detrimental fault developed due to worse powder application in the SLM process. Since the layers in the vertically built samples are aligned along the direction of the applied force (Figure 39), a poor connection of individual layers is unfavourable regarding the flexural strength of the sample. Therefore, the scattering of the flexural strength due to possible building mistakes and material inhomogeneities should be taken into account when working with this SLM-fabricated BMG. Nevertheless, an average flexural strength of approximately 2000 MPa is still substantial.

Furthermore, the measurements point out that the heat treatments decrease the flexural strength of the samples. Due to the structural relaxation of the sample, the average flexural strength is reduced by around 25% to  $1488 \pm 382$  MPa. Also, the average displacement is reduced from  $0.977 \pm 0.187$  mm to  $0.830 \pm 0.126$  mm. A far greater reduction of the flexural strength is observable for the crystallised samples. They show an average flexural strength of  $180 \pm 19$  MPa, which corresponds to a reduction of a factor of around 10 compared to the amorphous samples. Additionally, an extremely small bending displacement of  $0.128 \pm 0.015$  mm is noticeable for these samples. This reduction in the flexural strength and bending displacement is a consequence due to the existing crystals in the amorphous microstructure. The evolved residual stress state contributes to the brittle fracture without plastic deformation.

<b>1<sup>st</sup> test series:</b> <i>vertically built samples, testing orientation V</i>	<b>as-built</b>	<b>as-built + glass blasted</b>	<b>as-built + corundum blasted</b>
Flexural strength [MPa]	$1078 \pm 98$ MPa	$1741 \pm 119$	$1698 \pm 57$
Bending displacement [mm]	$0.765 \pm 0.061$	$0.803 \pm 0.061$	$0.873 \pm 0.085$
<b>2<sup>nd</sup> test series:</b> <i>vertically built samples, testing orientation V</i>	<b>as-built + glass blasted</b>	<b>650 K + glass blasted</b>	<b>850 K + glass blasted</b>
Flexural strength [MPa]	$2041 \pm 446$	$1488 \pm 382$	$180 \pm 19$
Bending displacement [mm]	$0.977 \pm 0.187$	$0.830 \pm 0.126$	$0.128 \pm 0.015$
<b>3<sup>rd</sup> test series:</b> <i>horizontally built samples, as-built + glass blasted</i>	<b>testing orientation: H0°</b>	<b>testing orientation: H180°</b>	<b>testing orientation: H90°</b>
Flexural strength [MPa]	$1816 \pm 115$	$2439 \pm 112$	$2416 \pm 134$
Bending displacement [mm]	$1.194 \pm 0.341$	$1.403 \pm 0.094$	$1.455 \pm 0.099$

Table 11: Summary of the average values obtained from the 4-point bending tests. Individual values of the tested samples can be found in the Appendix, Section 1.5



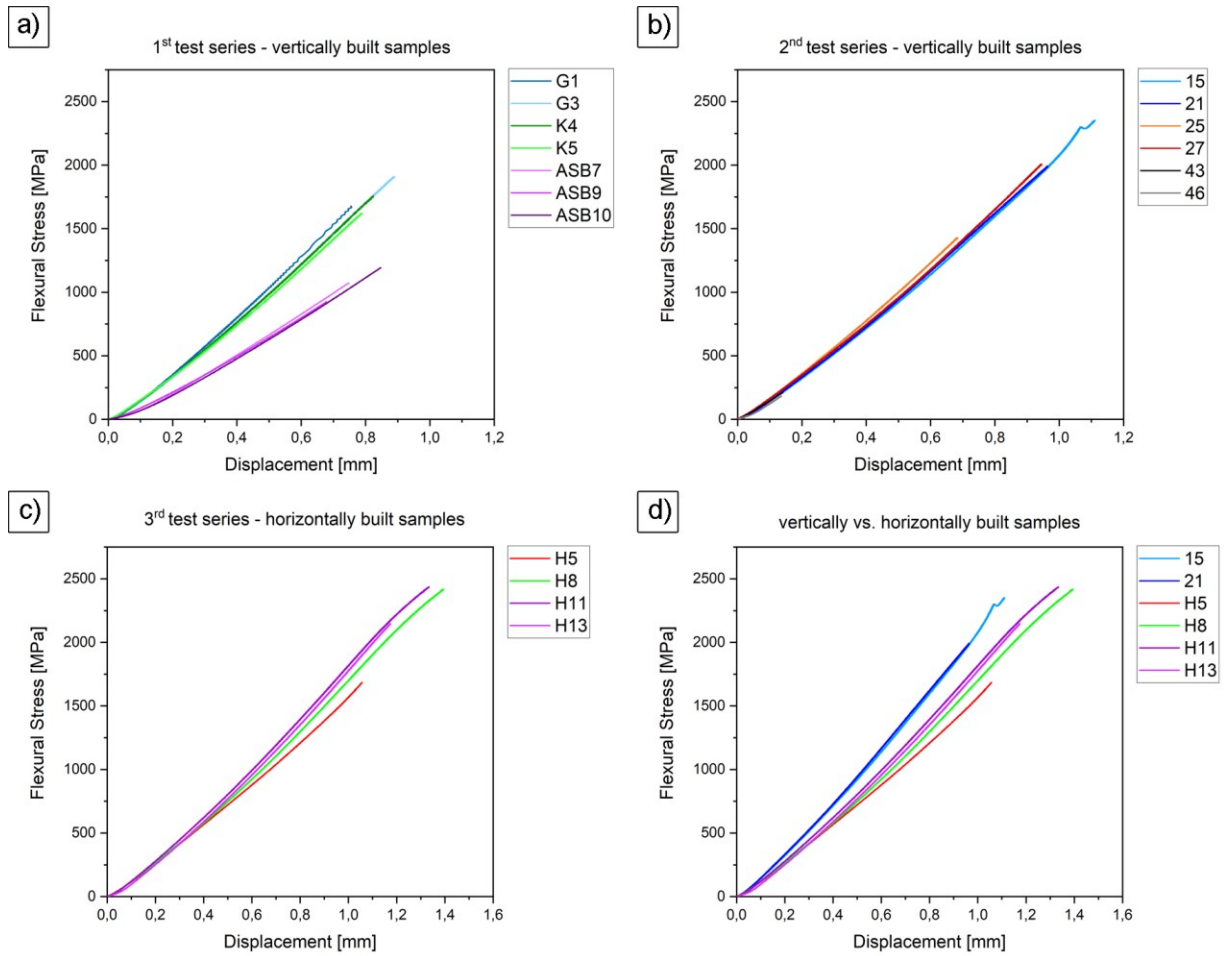


Figure 40: Stress – displacement curves of selected SLM-fabricated samples: a) 1<sup>st</sup> test series, comparison of vertically built samples with different surface treatment, b) 2<sup>nd</sup> tests series, comparison of glass blasted vertically built samples in different thermodynamic state, c) 3<sup>rd</sup> test series, comparison of glass blasted horizontally built samples tested in different directions, d) comparison of vertically and horizontally built samples.

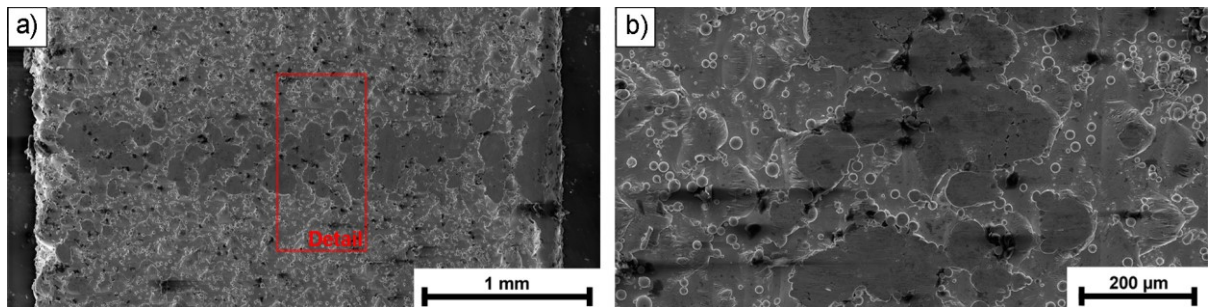


Figure 41: a) Imprint of the supporting and the squeezed powder particles on the surface of the as-built bending test sample ASB10 (1<sup>st</sup> test series), b) a detail - rotated by 90° - of the samples surface.

The SEM micrographs taken from the fracture surfaces of sample 15 (as-built), sample 25 (structurally relaxed) and 46 (crystallised) are shown in Figure 42, Figure 43, and Figure 44, respectively. The direction of the applied force is marked with a red arrow. Additionally, the direction of the sample is displayed in the bottom left part of the pictures. On the rugged fracture surface of the as-built sample, the typical vein-like pattern can be observed. However, there is also an area where a single fracture plane was formed. Such a formation can be found in Zr-based BMG samples which were subjected to compressive stresses [29]. However, in the case of sample 15, the single fracture plane was formed on the side where tensile stresses were present. Nonetheless, it can be an indication that in this area, a stable crack growth took place. The vein-like pattern can be seen on this formed fracture plane as well. However, it is much finer than the one on the rugged fracture surface. On the side where the force was applied a transverse groove is visible (Figure 42b). The groove's position is situated near the pressure points of the loading pins. This phenomenon of material breaking out, where the load was applied, occurred at multiple samples (compare sample H11 in Figure 45). As a result of this, most of the samples failed in this region.

The fracture surfaces of the structurally relaxed samples look similar. Again, they are quite rugged and the vein-like patterns are visible. However, small relatively smooth areas are present (Figure 43b). When observing the samples without a microscope, the appearance of the fracture surface is more reflective than the one of the not heat-treated samples. While most samples broke again in the region of the loading point, sample 25 broke almost in the middle of the bar. As seen in Figure 43c, a horizontally orientated plane is visible in one edge of the fracture surface. It is assumed that this is a defect which evolved during the SLM-process. This would explain the failure in the middle of the sample and its reduced flexural strength of 1428 MPa.

The crystallised samples' fracture surface looks different compared to the ones of the fully amorphous samples (Figure 44). It appears immensely shiny and reflective. Instead of the vein-like pattern an extremely smooth fracture surface with only a few irregularities was formed. Consequently, it can be stated that the existing (nano-)crystals do not only reduce the flexural strength, but that they also change the appearance of the fracture surface.

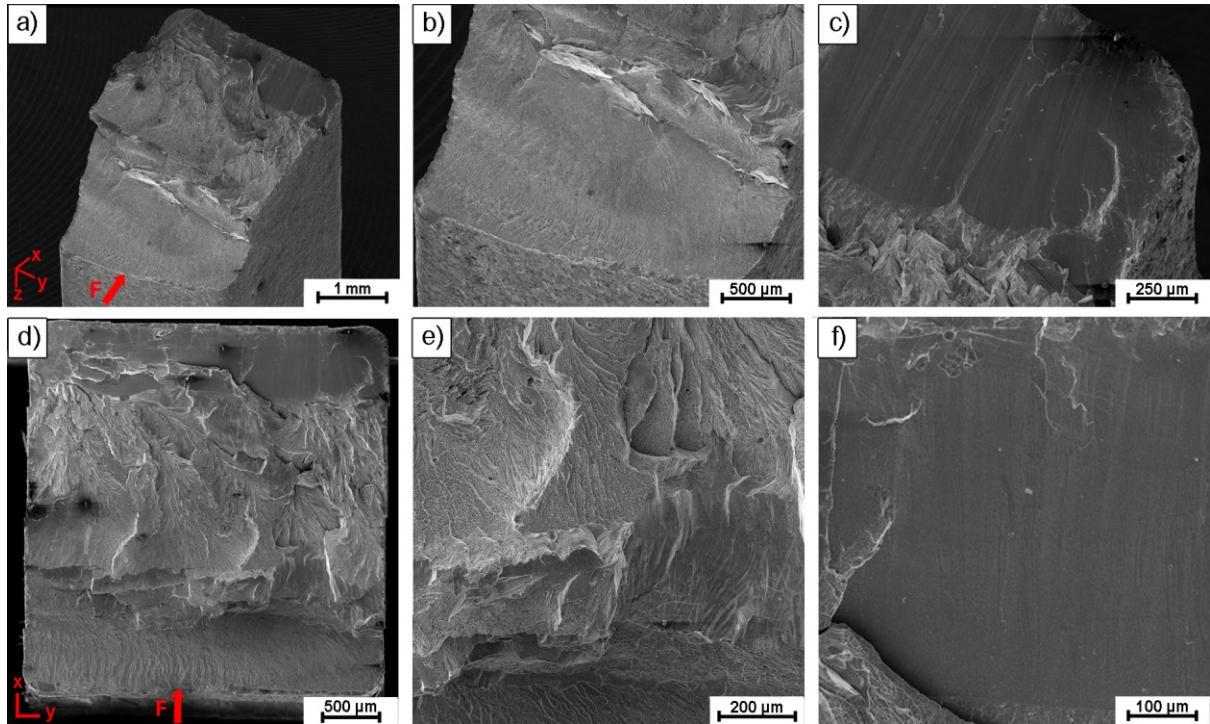


Figure 42: SEM micrographs of the fracture surface of the as-built sample number 15 which was built in vertical direction: a) 3D overview, b) detail of the side where compressive stresses were present, material broke out there, c) smooth single fracture plane at the side where tensile stresses existed, d) top view of the fracture surface, e) and f) details of the top view, the rugged surface and the smooth plane, respectively.

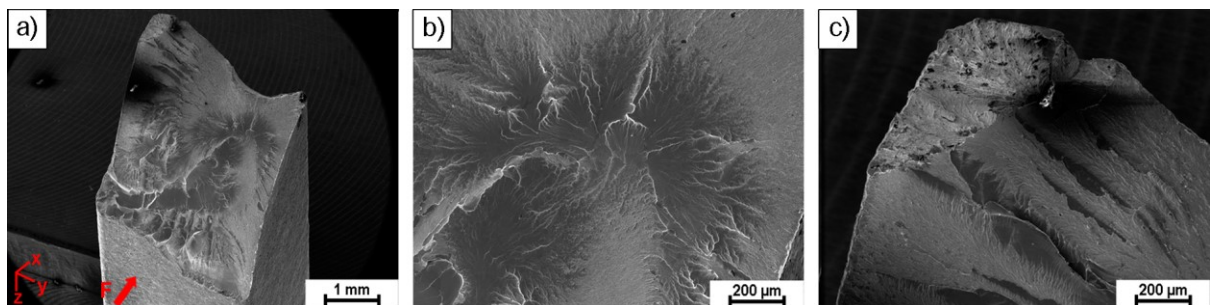


Figure 43: SEM micrographs of the fracture surface of the structurally relaxed sample 25 which was built in vertical direction: a) 3D overview, b) magnified detail of the relatively smooth part of the fracture surface, and c) horizontally oriented plane on the fracture surface.

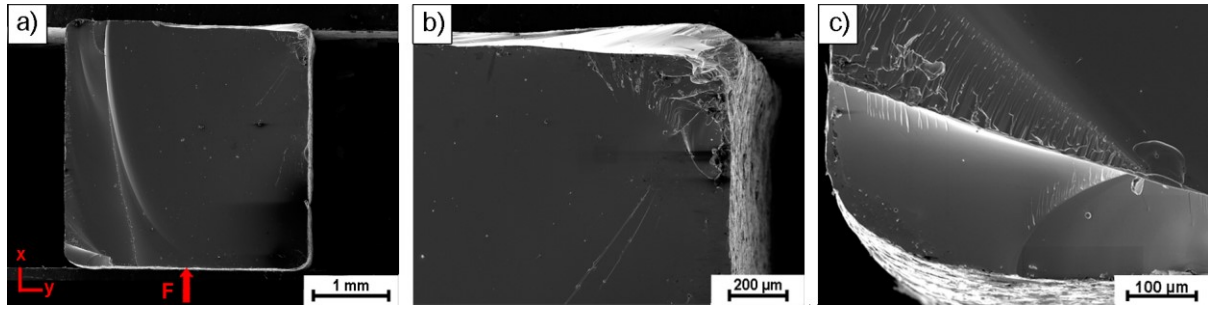


Figure 44: SEM micrographs of the fracture surface of the crystallised sample 46 which was built in vertical direction: a) Top view b) and c) some magnified details of the fracture surface.

For the horizontally built samples the flexural strength is dependent on their test direction. Even before carrying out the bending test, different stress conditions are present in the samples. Due to the bending up, compressive stresses exist on the top surface and tensile stresses are predominant on the other side. When testing the samples in direction  $H0^\circ$  (Figure 39b), the tensile stresses add up and the samples fail earlier, i.e. at lower applied forces. Thus, the average flexural strength of these samples is  $1816 \pm 115$  MPa. The opposite happens for samples inserted in direction  $H180^\circ$ : the compressive stresses compensate the tensile stress from the testing. Consequently, the average flexural strength of samples tested in direction  $H180^\circ$  is higher ( $2439 \pm 112$  MPa).

For the samples which were tested in the orientation  $H90^\circ$  an average flexural strength of  $2416 \pm 134$  MPa was determined. The influence of the bending up should be minimized for this test set up. However, when comparing this value with the one of the vertically built samples, it is evident that the horizontally built samples exhibit a higher flexural strength. This higher value can result from the differently oriented layers or rather the different building direction of the samples (compare the z-directions in Figure 39a and d). Although the microstructure of the SLM-fabricated sample look homogenous (Figure 21), it is assumed that the connection between the layers are potential weaknesses [56]. Therefore, the vertically built samples show a lower flexural strength: their layers are aligned perpendicular to the direction of the stresses. However, in the horizontally built samples, the layers are parallel to the stresses and the weak areas between the layers are less decisive. Due to this preferable orientation of the layers in the horizontally built samples, the average maximum displacement of these sample is higher compared the one of the vertically built samples (Figure 40d). However, individual layers cannot be observed in the samples tested in different orientations. In contrast, this would again suggest that the structure is homogeneously built up. Hence, further investigations have to be done to clarify this behaviour of the layered BMG. To resolve this issue, a finite element analysis can help.



In Figure 45, SEM micrographs of the horizontally built sample H11, which was tested in the testing orientation  $H90^\circ$ , are shown. The fracture surfaces of the other investigated samples built in horizontal direction look similar. As mentioned above, individual layers are not visible. However, vein-like patterns can be observed on the fracture surface due to the amorphous nature of the BMG (Figure 45c and e). Besides, the same features as already discovered in sample 15 (Figure 42) can be seen. On the side where tensile stresses were present, a single fracture plane was formed. Furthermore, a groove which originates from the material break out in the area of the loading pins' pressure points is visible on the other side.

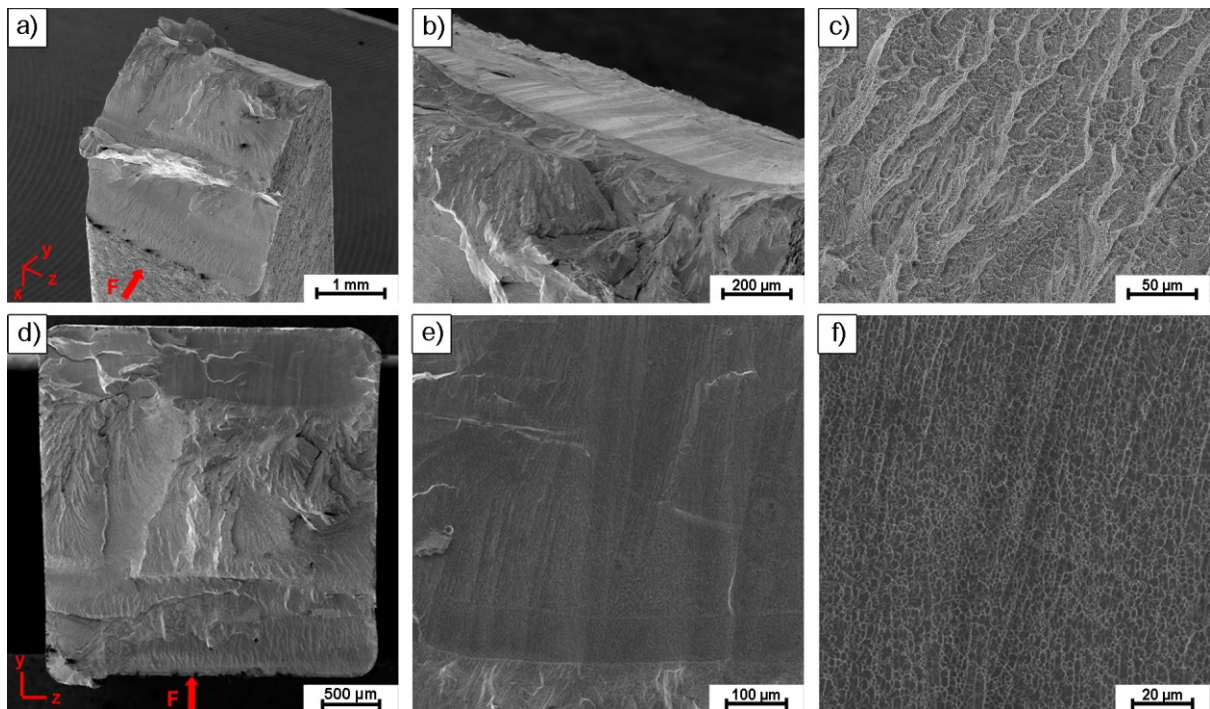


Figure 45: Fracture surface of the horizontally built sample H11. The 4 point bending test were carried out in the testing orientation  $H90^\circ$ . a) 3D overview of the fracture surface, b) smooth fracture plane on the side where tensile stresses were present, c) vein-like pattern of the groove, evolved on the side of compression, d) top view, e) and f) magnified micrographs of the smooth fracture plane and the fine pattern on it.

#### 4.6. Cytotoxicity, Cell Adhesion and Cell Growth

The results of the in vitro cytotoxicity tests are given in Figure 46. The cell viability in the particular eluate is presented as percentage of the viability in the control, where cells can grow under physiological cultivation condition. Samples are non-cytotoxic if the cell viability is above 70%. The most expressive value is the cell viability in the pure eluate. Thus, both variants of the glass blasted samples, the as-built and the at 650 K heat-treated ones, can be referred to as non-cytotoxic samples. The cells can grow there without any significant inhibition. The values of the cell viability are above 90% compared to the control group. Furthermore, the heat treatment entails a slight increase in viability. The same circumstances can be seen for the samples which were blasted with corundum. While the as-built samples without any heat treatment show an enormous growth inhibition (cell viability is 63% in pure eluate), the heat-treated ones exhibit a cell viability of 83%. Consequently, the as-built and corundum blasted samples are cytotoxic whereas the heat-treated ones are acceptable. The difference in the results regarding to the two different surface treatments might result from the rougher surface of the corundum blasted samples as seen in Figure 35. Moreover, the glass and corundum blasted samples differ with regard to their topography (Figure 33). Another cause of the growth inhibition can be a dissolution of the material. However, the reasons of the lower cell viability were not further investigated in this thesis. Also, the difference in viability between the as-built and heat-treated samples is not fully clarified yet. A possible explanation is that the heat-treated samples are more stable in the eluate due to their closely packed atomic structure. Therefore, the cell viability is not considerably affected by material dissolution. Besides this, the increased hardness due to the heat treatment can have an impact regarding to the implantation of blasting material into the surface or the amount of surface roughness. As seen in Figure 35, a slight decrease in the Ra-value of the at 650 K heat-treated and corundum blasted sample is present. Perhaps this small difference can already increase the cell viability. For the glass blasted sample there is no significant difference observable, thus the difference in the cell viability is also not that high; 94% and 98% for the as-built and heat-treated sample, respectively.

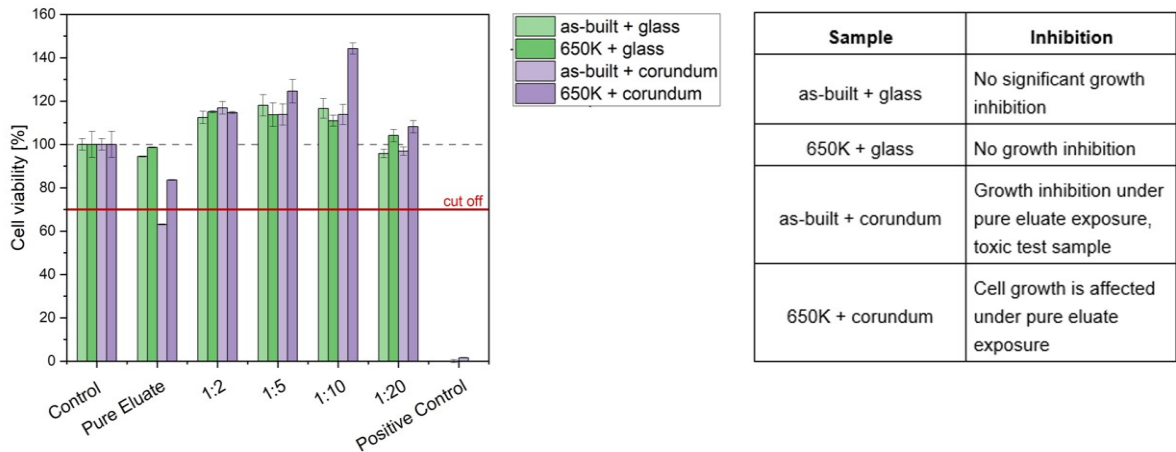


Figure 46: Measured cell viability presented as percentage of cell viability in untreated control and a short summary of the test results.

Figure 47 and Figure 48 show micrographs taken from the stained cells grown on the samples' surfaces. The first micrograph (a) is taken from the as-built samples, the second (b) from the heat-treated ones, and the third (c) is a micrograph taken from the control sample, where cells are grown under physiological cultivation conditions.

In Figure 47, the adhering cells on the glass blasted samples are visible. Even if the SLM-fabricated samples shine in the background the cells can be seen clearly. The cells morphology is only slightly different to the one observed on the control. Therefore, it can be concluded that they are 'healthy'. However, the micrographs taken from the corundum blasted samples (Figure 48) look completely different. On the one hand, there is hardly any reflection of the sample in the background, on the other hand the cells are not easily identifiable. A lot of other particles, most likely the implanted corundum particles, reflect the light of the microscope. Therefore, a distinction between cells and particles is difficult. However, some cells could be found and are marked with white arrows. These cells are smaller than the ones of the control. These results are in line with the results of the cytotoxicity test. While the glass blasted sample offer a satisfying surface for cell adhesion and growing, the corundum blasted samples do not. Also, the positive influence of the heat treatment can be seen. The number of cells found on the heat-treated samples seems to be more than the ones on the as-built samples. This is especially noticeable in the micrographs of the glass blasted sample.

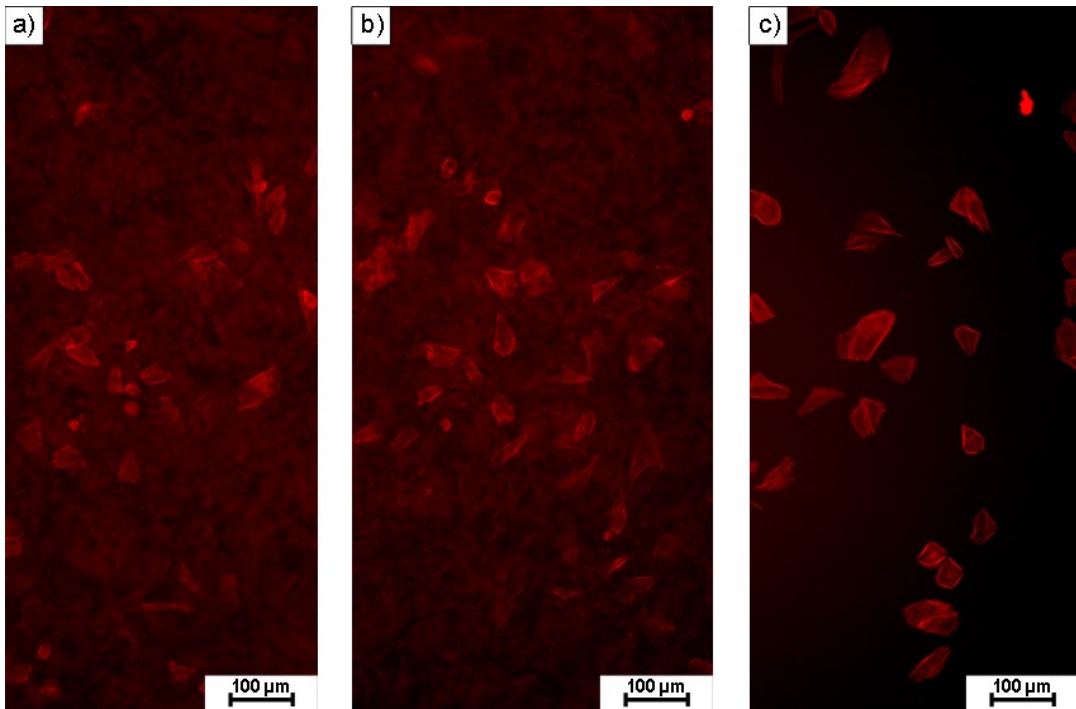


Figure 47: Cell morphology of grown Saos-2 cells on SLM-fabricated BMG samples with different post processing versus cells grown on a control sample: a) as-built and glass blasted BMG, b) heat-treated at 650 K and glass blasted BMG, c) control sample.

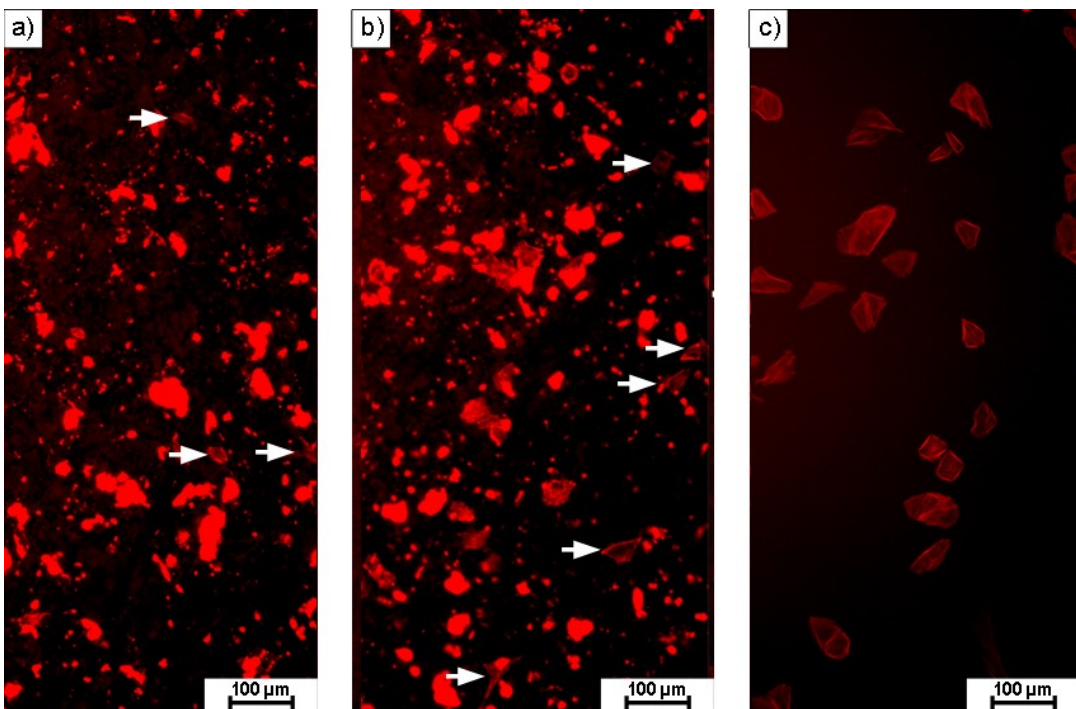


Figure 48: Cell morphology of grown Saos-2 cells on SLM-fabricated BMG samples with different post processing versus cells grown on a control sample: a) as-built and corundum blasted BMG, b) heat-treated at 650 K and corundum blasted BMG, c) control sample.



## 5. Conclusions

This work shows that selective laser melting, an additive manufacturing method, can be successfully applied for the production of dense Zr-based bulk metallic glass parts, which should eventually find an application in the medical field. Even if there are many factors influencing the SLM process, appropriate parameters could be found in order to obtain an amorphous microstructure of the dense BMG samples.

In a SLM parameter study, different values of the process parameters (laser power, scanning velocity, and hatching) and consequently different volume energy densities were applied for two given layer thicknesses (0.05 mm and 0.02 mm). For a layer thickness of 0.05 mm, dense samples could be produced with an energy density greater than 15 J/mm<sup>3</sup>. Lower values of the energy density led to a decrease in the relative density of the BMG sample. The influence of the interrelating process parameters on the relative density was visualised in density contour maps. Thereby, it was found that for a given hatching and volume energy density rather low laser power and low scanning velocity are preferable in order to obtain denser samples. The optimal hatching to obtain a high relative density was determined to be between 0.08 mm and 0.10 mm for the used process parameter combinations. The parameter study carried out with the layer thickness of 0.02 mm showed that for the used process parameter combinations, a higher volume energy density ( $E > 20 \text{ J/mm}^3$ ) is required to produce dense samples. XRD and DSC measurements confirmed that almost fully glassy samples were produced by SLM. Additionally, a dependence of the samples' structural relaxation enthalpy  $\Delta H_{\text{str}}$ , glass transition temperature  $T_{\text{g,on}}$ , and indentation elastic modulus,  $E_{\text{IT}}$ , on the used process parameter, especially on the used scanning velocity, was explored.

4-point bending tests showed that vertically built test samples produced with a selected parameter set, by which dense and amorphous samples were obtained, exhibit an average flexural strength of  $\sim 1100 \text{ MPa}$ . The elasticity of the BMG is reflected in the value of the maximal displacement. This was determined to be  $\sim 0.8 \text{ mm}$  for the tested samples. The investigations regarding the influence of a post processing showed that a surface treatment is beneficial regarding the flexural strength. A blasting treatment with glass microbeads or corundum executed after the SLM process increases the flexural strength of the vertically built bending test samples up to  $\sim 2000 \text{ MPa}$ . However, the determined deviation of  $\sim 500 \text{ MPa}$ , which originates from samples with detrimental building faults, is not negligible.

Moreover, the kind of the surface treatment is important to consider regarding the biocompatibility. It turned out that a surface treatment with glass microbeads is more beneficial in this case. Samples blasted with glass microbeads show a non-cytotoxic behaviour and 'healthy' cells on the samples surface could be observed. However, the cell viability is significantly lower for samples treated with corundum so that they are cytotoxic. In addition, the detection of the adherent cells is difficult, since other reflections, most likely caused by implanted corundum particles from the blasting treatment, outshine them. Within the cytotoxicity tests, an improvement in cell viability was investigated for samples, which were heat-treated below the glass transition temperature (60 minutes at 650 K) before carrying out the respective surface treatment.

Nonetheless, a heat treatment is only beneficial for cytotoxicity and solely if the temperature of the treatment is below the glass transition temperature. Due to partial structural relaxation of the samples, a reduction of the flexural strength by 25% as well as a lower maximal displacement occur. A more drastic reduction in both values is observed for samples heat-treated above the crystallisation temperature (at 850 K). Moreover, due to an embrittlement of the crystallised samples, a blasting treatment after the heat treatment is unfeasible.

The fabrication of bending test samples in horizontal direction leads to a bend up of the samples after removing them from the building platform. Therefore, the flexural strength of these samples strongly depends on the testing orientation and varies from ~ 1800 MPa to ~ 2400 MPa. Moreover, it was determined that horizontally built samples tested perpendicular to the bend up exhibit a higher flexural strength than the vertically built samples.

Despite the possibility to fabricate biocompatible Zr-based BMG parts by SLM, there are still challenges which have to be overcome. It was concluded that the fabrication of samples with a great height might be difficult to realise. Due to an accumulation of the introduced heat, crystallisation of the samples takes place. Consequently, this reduces the manufacturability and usability of the BMG dramatically. Furthermore, difficulties with the reproducibility of the building job were discovered. This shows that not only the process parameter can influence the SLM process, but also other factors that are still not fully understood and require further research.

## 6. References

- [1] S. Pauly, L. Löber, R. Petters, M. Stoica, S. Scudino, U. Kühn, J. Eckert, "Processing metallic glasses by selective laser melting," *Materials Today*, vol. 16, 1-2, pp. 37–41, 2013, doi: 10.1016/j.mattod.2013.01.018.
- [2] M. Telford, "The case for bulk metallic glass," *Materials Today*, vol. 7, no. 3, pp. 36–43, 2004, doi: 10.1016/S1369-7021(04)00124-5.
- [3] C. Suryanarayana and A. Inoue, *Bulk metallic glasses*. Boca Raton: CRC Press Taylor & Francis Group, 2018.
- [4] B. Bochtler, "Thermophysical and Structural Investigations of of a CuTi- and a Zr-based Bulk Metallic Glass, the Influence of Minor Additions, and the Relation to Thermoplastic Forming," Dissertation, Universität des Saarlandes, Saarbrücken. Accessed: Oct. 8 2021. [Online]. Available: <https://dx.doi.org/10.22028/D291-31111>
- [5] *Crystalline and Amorphous Solids*. [Online]. Available: <https://www.toppr.com/guides/chemistry/the-solid-state/crystalline-and-amorphous-solids/> (accessed: Sep. 30 2021).
- [6] W. Klement, R. H. Willens, P. Duwez, "Non-crystalline Structure in Solidified Gold–Silicon Alloys," *Nature*, vol. 187, pp. 869–870, 1960.
- [7] S. R. J. Basu, "Bulk metallic glasses: A new class of engineering materials," *Sadhana*, vol. 28, 3-4, pp. 783–798, 2003, doi: 10.1007/BF02706459.
- [8] W.H. Wang, C.Dong, C.H. Shek, "Bulk metallic glasses," *Materials Science and Engineering: R: Reports*, vol. 44, 2-3, pp. 45–89, 2004, doi: 10.1016/j.mser.2004.03.001.
- [9] J. F. Löffler, "Bulk metallic glasses," *Intermetallics*, vol. 11, no. 6, pp. 529–540, 2003, doi: 10.1016/S0966-9795(03)00046-3.
- [10] A. Inoue, B. Shen, H. Koshiba, H. Kato, and A. R. Yavari, "Cobalt-based bulk glassy alloy with ultrahigh strength and soft magnetic properties," *Nature Mater*, vol. 2, no. 10, pp. 661–663, 2003, doi: 10.1038/nmat982.
- [11] Heraeus Amloy Technologies GmbH, *Datasheet AMLOY ZR02*. [Online]. Available: [https://www.heraeus.com/media/media/group/media\\_group/products/amorphous\\_metals/datasheets\\_1/Datasheet\\_AMLOY-ZR02~2.pdf](https://www.heraeus.com/media/media/group/media_group/products/amorphous_metals/datasheets_1/Datasheet_AMLOY-ZR02~2.pdf)
- [12] A. Inoue and A. Takeuchi, "Recent Progress in Bulk Glassy Alloys," *Mater. Trans.*, vol. 43, no. 8, pp. 1892–1906, 2002, doi: 10.2320/matertrans.43.1892.

- [13] T.-H. Chen and C.-K. Tsai, "The Microstructural Evolution and Mechanical Properties of Zr-Based Metallic Glass under Different Strain Rate Compressions," *Materials (Basel, Switzerland)*, vol. 8, no. 4, pp. 1831–1840, 2015, doi: 10.3390/ma8041831.
- [14] A. Kündig, J. Löffler, and F. Dalla Torre, "Rapid Solidification and Bulk Metallic Glasses — Processing and Properties," in *Materials Processing Handbook*, M. Powers, E. Lavernia, J. Groza, and J. Shackelford, Eds.: CRC Press, 2007, 17-1-17-44.
- [15] D. V. Louzguine-Luzgin and V. I. Polkin, "Properties of bulk metallic glasses," *Russ. J. Non-ferrous Metals*, vol. 58, no. 1, pp. 80–92, 2017, doi: 10.3103/S1067821217010084.
- [16] R. Chatterjee, "Manufacturing of Metallic Glasses," *Advanced Materials Manufacturing & Characterization*, no. 7, pp. 24–29, 2017. [Online]. Available: [http://www.ijammc-griet.com/attach/1491225541\\_5.pdf](http://www.ijammc-griet.com/attach/1491225541_5.pdf)
- [17] D. Ouyang, N. Li, W. Xing, J. Zhang, and L. Liu, "3D printing of crack-free high strength Zr-based bulk metallic glass composite by selective laser melting," *Intermetallics*, vol. 90, pp. 128–134, 2017, doi: 10.1016/j.intermet.2017.07.010.
- [18] ISO/ASTM, *ISO/ASTM52900: Additive Manufacturing— General principles — Terminology*. [Online]. Available: <https://www.iso.org/obp/ui/#iso:std:iso-astm:52900:dis:ed-2:v1:en> (accessed: Oct. 8 2021).
- [19] T. DebRoy *et al.*, "Additive manufacturing of metallic components – Process, structure and properties," *Progress in Materials Science*, vol. 92, pp. 112–224, 2018, doi: 10.1016/j.pmatsci.2017.10.001.
- [20] C. K. Chua, K. F. Leong, *3D Printing And Additive Manufacturing: Principles And Applications*, 4th ed. Singapore: World Scientific Publishing Co Pte Ltd, 2015. [Online]. Available: <https://books.google.at/books?id=Gy88DQAAQBAJ&printsec=frontcover&hl=de#v=onepage&q&f=false>
- [21] T. D. Ngo, A. Kashani, G. Imbalzano, K. T. Nguyen, and D. Hui, "Additive manufacturing (3D printing): A review of materials, methods, applications and challenges," *Composites Part B: Engineering*, vol. 143, pp. 172–196, 2018, doi: 10.1016/j.compositesb.2018.02.012.
- [22] L. Jiao, Z. Y. Chua, S. K. Moon, J. Song, G. Bi, and H. Zheng, "Femtosecond Laser Produced Hydrophobic Hierarchical Structures on Additive Manufacturing Parts," *Nanomaterials (Basel, Switzerland)*, vol. 8, no. 8, 2018, doi: 10.3390/nano8080601.

- [23] D. Gu, *Laser Additive Manufacturing of High-Performance Materials*. Berlin, Heidelberg: Springer Berlin Heidelberg, 2015.
- [24] T. Kurzynowski, E. Chlebus, B. Kuźnicka, and J. Reiner, "Parameters in selective laser melting for processing metallic powders," in *High Power Laser Materials Processing: Lasers, Beam Delivery, Diagnostics, and Applications*, San Francisco, California, USA, 2012, p. 823914.
- [25] D. Herzog, V. Seyda, E. Wycisk, and C. Emmelmann, "Additive manufacturing of metals," *Acta Materialia*, vol. 117, pp. 371–392, 2016, doi: 10.1016/j.actamat.2016.07.019.
- [26] C. Klahn, B. Leutenecker, and M. Meboldt, "Design for Additive Manufacturing – Supporting the Substitution of Components in Series Products," *Procedia CIRP*, vol. 21, pp. 138–143, 2014, doi: 10.1016/j.procir.2014.03.145.
- [27] L.-C. Zhang, H. Attar, M. Calin, and J. Eckert, "Review on manufacture by selective laser melting and properties of titanium based materials for biomedical applications," *Materials Technology*, vol. 31, no. 2, pp. 66–76, 2016, doi: 10.1179/1753555715Y.0000000076.
- [28] K. G. Prashanth, S. Scudino, T. Maity, J. Das, and J. Eckert, "Is the energy density a reliable parameter for materials synthesis by selective laser melting?," *Materials Research Letters*, vol. 5, no. 6, pp. 386–390, 2017, doi: 10.1080/21663831.2017.1299808.
- [29] S. Pauly, C. Schrickler, S. Scudino, L. Deng, and U. Kühn, "Processing a glass-forming Zr-based alloy by selective laser melting," *Materials & Design*, vol. 135, pp. 133–141, 2017, doi: 10.1016/j.matdes.2017.08.070.
- [30] X. P. Li, M. P. Roberts, S. O'Keeffe, and T. B. Sercombe, "Selective laser melting of Zr-based bulk metallic glasses: Processing, microstructure and mechanical properties," *Materials & Design*, vol. 112, pp. 217–226, 2016, doi: 10.1016/j.matdes.2016.09.071.
- [31] S. Pauly, P. Wang, U. Kühn, and K. Kosiba, "Experimental determination of cooling rates in selectively laser-melted eutectic Al-33Cu," *Additive Manufacturing*, vol. 22, pp. 753–757, 2018, doi: 10.1016/j.addma.2018.05.034.
- [32] C. Y. Yap *et al.*, "Review of selective laser melting: Materials and applications," *Applied Physics Reviews*, vol. 2, no. 4, p. 41101, 2015, doi: 10.1063/1.4935926.
- [33] Y. Tian, D. Tomus, P. Rometsch, and X. Wu, "Influences of processing parameters on surface roughness of Hastelloy X produced by selective laser

- melting," *Additive Manufacturing*, vol. 13, pp. 103–112, 2017, doi: 10.1016/j.addma.2016.10.010.
- [34] S. Pal *et al.*, "As-fabricated surface morphologies of Ti-6Al-4V samples fabricated by different laser processing parameters in selective laser melting," *Additive Manufacturing*, vol. 33, p. 101147, 2020, doi: 10.1016/j.addma.2020.101147.
- [35] Y. Kok *et al.*, "Anisotropy and heterogeneity of microstructure and mechanical properties in metal additive manufacturing: A critical review," *Materials & Design*, vol. 139, pp. 565–586, 2018, doi: 10.1016/j.matdes.2017.11.021.
- [36] M. R. Condruz, G. Matache, A. Paraschiv, T. F. Frigioescu, and T. Badea, "Microstructural and Tensile Properties Anisotropy of Selective Laser Melting Manufactured IN 625," *Materials (Basel, Switzerland)*, vol. 13, no. 21, 2020, doi: 10.3390/ma13214829.
- [37] S. L. Sing, *Selective Laser Melting of Novel Titanium-Tantalum Alloy as Orthopaedic Biomaterial*. Singapore: Springer Singapore, 2019.
- [38] M. D. Demetriou A. Wiest D. C. Hofmann W. L. Johnson B. Han ,P. K. Liaw, "Amorphous Metals For Hard-tissue Prothesis," *JOM*, vol. 2010, no. 62, pp. 83–91. [Online]. Available: <https://link.springer.com/content/pdf/10.1007/s11837-010-0038-2.pdf>
- [39] C. Zhang, X. Li, S.-Q. Liu, H. Liu, L.-J. Yu, and L. Liu, "3D printing of Zr-based bulk metallic glasses and components for potential biomedical applications," *Journal of Alloys and Compounds*, vol. 790, pp. 963–973, 2019, doi: 10.1016/j.jallcom.2019.03.275.
- [40] J. Schroers, G. Kumar, T. M. Hodges, S. Chan, and T. R. Kyriakides, "Bulk metallic glasses for biomedical applications," *JOM*, vol. 61, no. 9, pp. 21–29, 2009, doi: 10.1007/s11837-009-0128-1.
- [41] P. Meagher, E. D. O'Cearbhaill, J. H. Byrne, and D. J. Browne, "Bulk Metallic Glasses for Implantable Medical Devices and Surgical Tools," *Advanced materials (Deerfield Beach, Fla.)*, vol. 28, no. 27, pp. 5755–5762, 2016, doi: 10.1002/adma.201505347.
- [42] V. Hoppe *et al.*, "Study of cytotoxic activity of Ti–13Nb–13Zr medical alloy with different surface finishing techniques," *J Mater Sci*, vol. 56, no. 31, pp. 17747–17767, 2021, doi: 10.1007/s10853-021-06430-y.

- [43] P. Ginestra *et al.*, “Surface finish of Additively Manufactured Metals: biofilm formation and cellular attachment,” *ESAFORM 2021*, 2021, doi: 10.25518/esaform21.2089.
- [44] Günter Petzow, *Metallographisches, keramographisches, plastographisches Ätzen*.
- [45] Promega GmbH, *CellTiter 96® AQueous Non-Radioactive Cell Proliferation Assay (MTS)*. [Online]. Available: [https://at.promega.com/products/cell-health-assays/cell-viability-and-cytotoxicity-assays/celltiter-96-aqueous-non-radioactive-cell-proliferation-assay-\\_mts\\_/?catNum=G5421](https://at.promega.com/products/cell-health-assays/cell-viability-and-cytotoxicity-assays/celltiter-96-aqueous-non-radioactive-cell-proliferation-assay-_mts_/?catNum=G5421) (accessed: Oct. 8 2021).
- [46] Thermo Fisher Scientific, *Invitrogen™ Rhodamine Phalloidin*. [Online]. Available: <https://www.fishersci.at/shop/products/molecular-probes-rhodamine-phalloidin/10063052> (accessed: Oct. 8 2021).
- [47] ThermoFisher Scientific, *Invitrogen User Guide - Phalloidins*. [Online]. Available: [https://assets.fishersci.com/TFS-Assets/LSG/manuals/MAN0001777\\_Phalloidins\\_UG.pdf?\\_ga=2.26518142.216225781.1630917669-107846452.1630917669](https://assets.fishersci.com/TFS-Assets/LSG/manuals/MAN0001777_Phalloidins_UG.pdf?_ga=2.26518142.216225781.1630917669-107846452.1630917669) (accessed: Oct. 8 2021).
- [48] MatWeb, *Materion Vit 105 Zirconium-Based Bulk Metallic Glass (BMG)*. [Online]. Available: <http://www.matweb.com/search/datasheettext.aspx?matguid=712680a7da4b4536a421515c7b2fdfa7> (accessed: Oct. 13 2021).
- [49] D. Ouyang, N. Li, and L. Liu, “Structural heterogeneity in 3D printed Zr-based bulk metallic glass by selective laser melting,” *Journal of Alloys and Compounds*, vol. 740, pp. 603–609, 2018, doi: 10.1016/j.jallcom.2018.01.037.
- [50] J. P. Best *et al.*, “Structural periodicity in laser additive manufactured Zr-based bulk metallic glass,” *Appl. Phys. Lett.*, vol. 115, no. 3, p. 31902, 2019, doi: 10.1063/1.5100050.
- [51] F. R. Salgado, J. F. d. S. Gonçalves, M. A. B. Mendes, N. D. de Campos Neto, and M. F. de Oliveira, “Vitreyloy-105 Behavior Under Mutual Wear,” *Mat. Res.*, vol. 23, no. 4, 2020, doi: 10.1590/1980-5373-mr-2020-0021.
- [52] M. Baricco, S. Spriano, I. Chang, M.I. Petrzhik, L. Battezzati, “*Big cube*” phase formation in Zr-based metallic glasses. [Online]. Available: [https://doi.org/10.1016/S0921-5093\(00\)01438-6](https://doi.org/10.1016/S0921-5093(00)01438-6)

- [53] A. Inoue, T. Negishi, H. M. Kimura, T. Zhang, A. R. Yavari, "High Packing Density of Zr- and Pd-Based Bulk Amorphous Alloys," *Materials Transactions, JIM*, Vol. 39, pp. 318–321, 1998. [Online]. Available: <https://doi.org/10.2320/matertrans1989.39.318>
- [54] Materials Project, *Zr<sub>6</sub>Al<sub>2</sub>Ni (hexagonal, P-62m, 189) mp-13092*. [Online]. Available: <https://materialsproject.org/materials/mp-13092/> (accessed: Oct. 13 2021).
- [55] Materials Project, *Ti<sub>2</sub>Ni (cubic, Fd-3m, 227) mp1808*. [Online]. Available: <https://materialsproject.org/materials/mp-1808/> (accessed: Oct. 13 2021).
- [56] W. Shifeng, L. Shuai, W. Qingsong, C. Yan, Z. Sheng, and S. Yusheng, "Effect of molten pool boundaries on the mechanical properties of selective laser melting parts," *Journal of Materials Processing Technology*, vol. 214, no. 11, pp. 2660–2667, 2014, doi: 10.1016/j.jmatprotec.2014.06.002.



## 7. Appendix

### 7.1. Building Jobs – SLM Parameter Study

In the following all the parameters used for the SLM parameter study are listed. For all tables the scanning velocity in [mm/s] is given on the left. The laser power in [W] is given in the upper line. The resulting energy density in [J/mm<sup>3</sup>] with the defined hatching in [mm] is given in the row/column intersection. The sample ID is given next to the resulting energy density in red.

#### 7.1.1. Layer Thickness $t_{s1} = 0.05$ mm

Building Job 01 (h = 0.10 mm)

$\frac{P}{v}$	80	sample	100	sample	120	sample	140	sample	160	sample	175	sample
800	20.00		25.00		30.00		35.00		40.00		43.75	
1000	16.00	01_01	20.00		24.00		28.00		32.00		35.00	
1200	13.33	01_02	16.67	01_06	20.00		23.33		26.67		29.17	
1400	11.43	01_03	14.29	01_07	17.14	01_10	20.00		22.86		25.00	
1600	10.00	01_04	12.50	01_08	15.00	01_11	17.50	01_13	20.00		21.88	
1800	8.89	01_05	11.11	01_09	13.33	01_12	15.56	01_14	17.78	01_15	19.44	

Building Job 02 (h = 0.15 mm)

$\frac{P}{v}$	80	sample	100	sample	120	sample	140	sample	160	sample	175	sample
800	13.33	02_01	16.67	02_04	20.00		23.33		26.67		29.17	
1000	10.67	02_02	13.33	02_05	16.00	02_09	18.67		21.33		23.33	
1200	8.89	02_03	11.11	02_06	13.33	02_10	15.56	02_14	17.78	02_18	19.44	
1400	7.62		9.52	02_07	11.43	02_11	13.33	02_15	15.24	02_19	16.67	02_22
1600	6.67		8.33	02_08	10.00	02_12	11.67	02_16	13.33	02_20	14.58	02_23
1800	5.93		7.41		8.89	02_13	10.37	02_17	11.85	02_21	12.96	02_24

Building Job 03 (h = 0.20 mm)

$\frac{P}{v}$	80	sample	100	sample	120	sample	140	sample	160	sample	175	sample
800	10.00	03_01	12.50	03_03	15.00	03_06	17.50	03_10	20.00		21.88	
1000	8.00	03_02	10.00	03_04	12.00	03_07	14.00	03_11	16.00	03_15	17.50	03_20
1200	6.67		8.33	03_05	10.00	03_08	11.67	03_12	13.33	03_16	14.58	03_21
1400	5.71		7.14		8.57	03_09	10.00	03_13	11.43	03_17	12.50	03_22
1600	5.00		6.25		7.50		8.75	03_14	10.00	03_18	10.94	03_23
1800	4.44		5.56		6.67		7.78		8.89	03_19	9.72	03_24

## Building Job 04 (h = 0.08 mm)

$\frac{P}{v}$	80	sample	100	sample	120	sample	140	sample	160	sample	175	sample
800	25.00		31.25		37.50		43.75		50.00		54.69	
1000	20.00		25.00		30.00		35.00		40.00		43.75	
1200	16.67		20.83		25.00		29.17		33.33		36.46	
1400	14.29	04_01	17.86		21.43		25.00		28.57		31.25	
1600	12.50	04_02	15.63		18.75		21.88		25.00		27.34	
1800	11.11	04_03	13.89	04_07	16.67		19.44		22.22		24.31	
2000	10.00	04_04	12.50	04_08	15.00	04_13	17.50		20.00		21.88	
2200	9.09	04_05	11.36	04_09	13.64	04_14	15.91		18.18		19.89	
2400	8.33	04_06	10.42	04_10	12.50	04_15	14.58	04_19	16.67		18.23	
2600	7.69		9.62	04_11	11.54	04_16	13.46	04_20	15.38		16.83	
2800	7.14		8.93	04_12	10.71	04_17	12.50	04_21	14.29	04_23	15.63	
3000	6.67		8.33		10.00	04_18	11.67	04_22	13.33	04_24	14.58	04_25

## Building Job 05 (h = 0.06 mm)

$\frac{P}{v}$	80	sample	100	sample	120	sample	140	sample	160	sample	175	sample
800	33.33		41.67		50.00		58.33		66.67		72.92	
1000	26.67		33.33		40.00		46.67		53.33		58.33	
1200	22.22		27.78		33.33		38.89		44.44		48.61	
1400	19.05		23.81		28.57		33.33		38.10		41.67	
1600	16.67		20.83		25.00		29.17		33.33		36.46	
1800	14.81	05_01	18.52		22.22		25.93		29.63		32.41	
2000	13.33	05_02	16.67		20.00		23.33		26.67		29.17	
2200	12.12	05_03	15.15	05_08	18.18		21.21		24.24		26.52	
2400	11.11	05_04	13.89	05_09	16.67		19.44		22.22		24.31	
2600	10.26	05_05	12.82	05_10	15.38	05_13	17.95		20.51		22.44	
2800	9.52	05_06	11.90	05_11	14.29	05_14	16.67		19.05		20.83	
3000	8.89	05_07	11.11	05_12	13.33	05_15	15.56	05_16	17.78		19.44	

### 7.1.2. Layer Thickness $ts_2 = 0.02$ mm

Building Job 06 and 08 (h = 0.10 mm)

$\frac{P}{v}$	40	sample	60	sample	80	sample
800	25.00	08_01	37.50		50.00	
1000	20.00	08_02	30.00	08_03	40.00	
1200	16.67	06_01	25.00	08_04	33.33	08_06
1400	14.29		21.43	08_05	28.57	08_07
1600	12.50	06_02	18.75		25.00	08_08
1800	11.11		16.67	06_03	22.22	08_09
2000	10.00		15.00		20.00	08_10
2200	9.09		13.64	06_04	18.18	
2400	8.33		12.50		16.67	06_05
2600	7.69		11.54		15.38	06_06
2800	7.14		10.71		14.29	
3000	6.67		10.00		13.33	

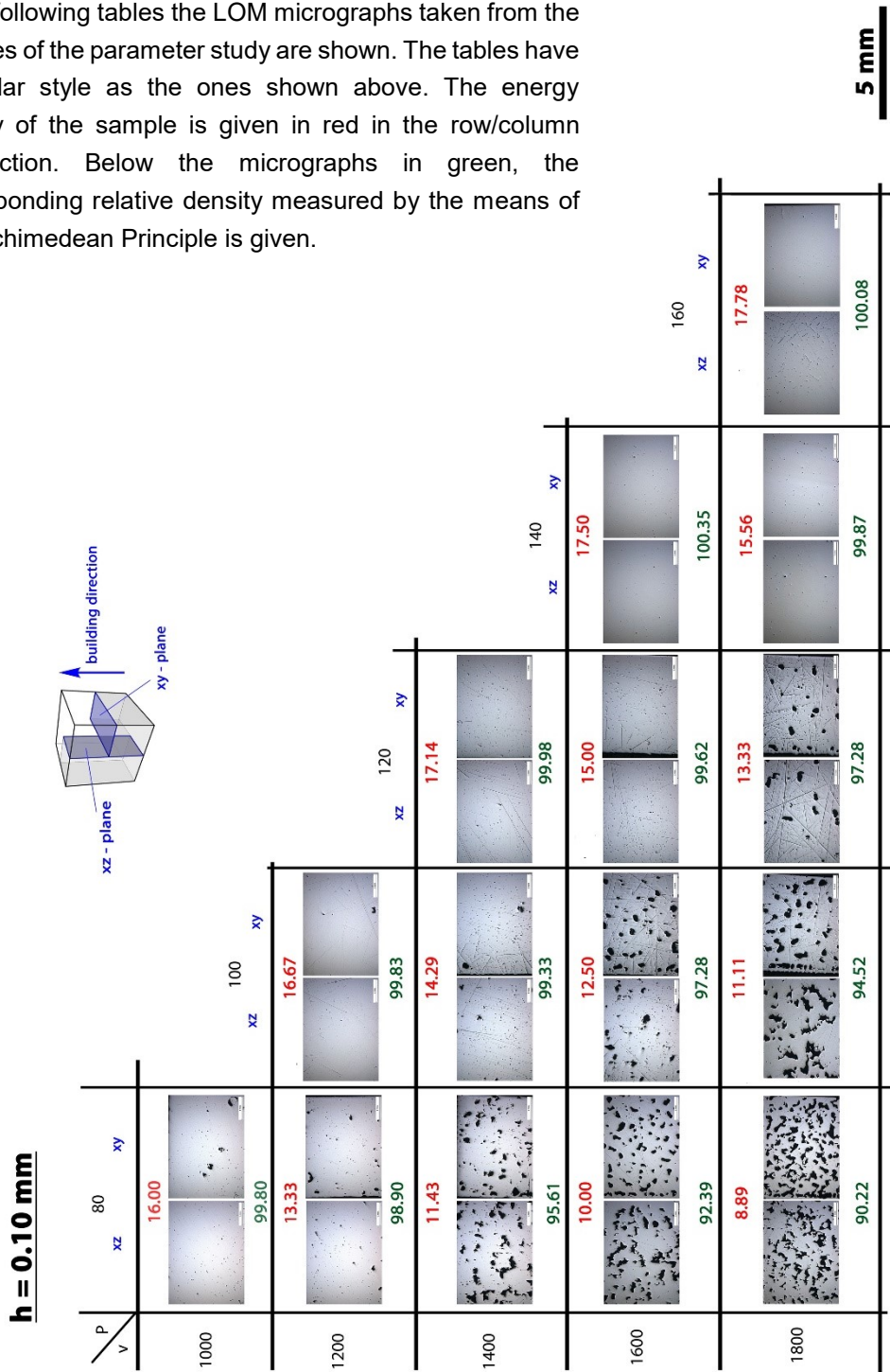
Building Job 07 and 09 (h = 0.08 mm)

$\frac{P}{v}$	40	sample	60	sample	80	sample
800	31.25	09_01	46.88		62.50	
1000	25.00	07_A1	37.50		50.00	
1200	20.83	07_B1	31.25	09_02	41.67	
1400	17.86	07_01	26.79	09_03	35.71	
1600	15.63	07_02	23.44	09_04	31.25	09_06
1800	13.89	07_03	20.83	09_05	27.78	09_08
2000	12.50	07_04	18.75		25.00	07_A3
2200	11.36		17.05	07_10	22.73	
2400	10.42		15.63	07_11	20.83	07_B3
2600	9.62		14.42	07_12	19.23	
2800	8.93		13.39	07_13	17.86	07_15
3000	8.33		12.50	07_14	16.67	07_16

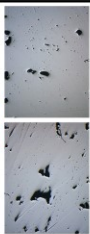

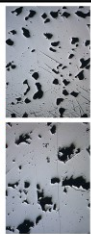
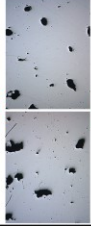
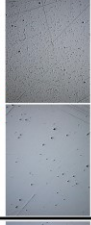






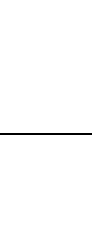
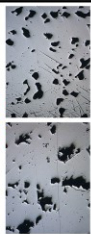
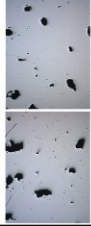

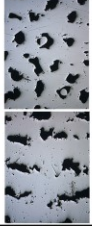



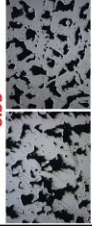





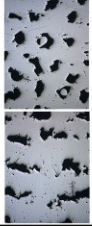



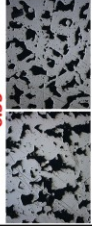









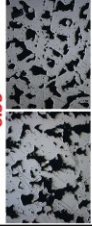







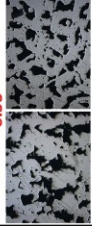












## 7.2. Relative Density - LOM Micrographs

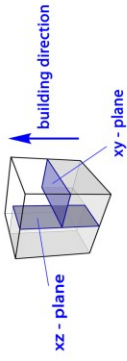
### 7.2.1. Layer Thickness $t_{s1} = 0.05$ mm

In the following tables the LOM micrographs taken from the samples of the parameter study are shown. The tables have a similar style as the ones shown above. The energy density of the sample is given in red in the row/column intersection. Below the micrographs in green, the corresponding relative density measured by the means of the Archimedean Principle is given.



**$h = 0.15 \text{ mm}$**

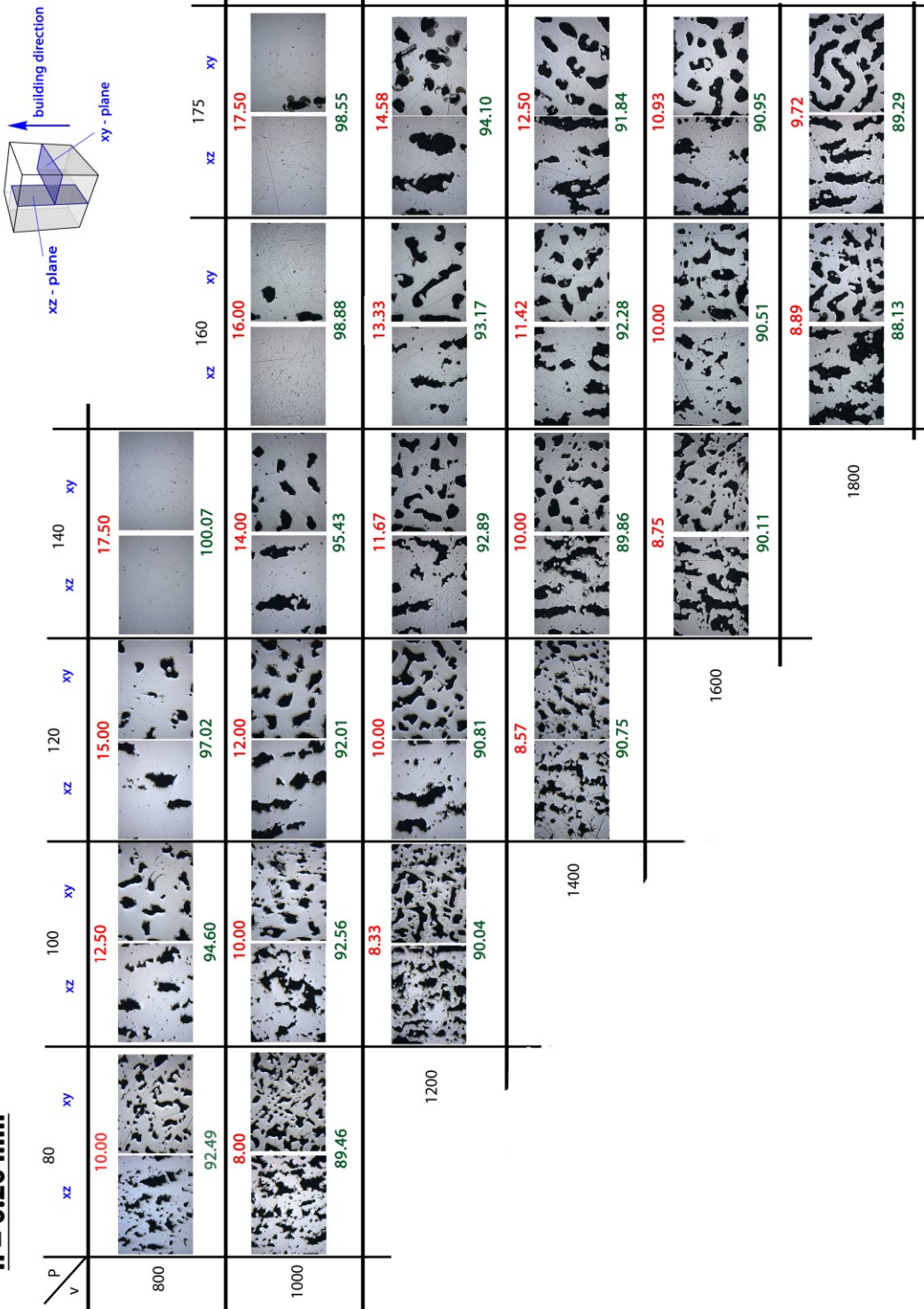
P V	80		100		120		140		160		175	
	xz	xy	xz	xy	xz	xy	xz	xy	xz	xy	xz	xy
800	 13.33	 16.67	 98.41	 100.00	 13.33	 16.00	 98.36	 99.88	 11.11	 13.33	 15.56	 17.78
1000	 10.67	 93.32	 8.89	 90.56	 9.52	 11.43	 8.33	 10.00	 8.89	 10.37	 11.67	 14.58
1200	 90.56	 93.76	 91.02	 94.85	 89.35	 91.45	 89.35	 91.45	 95.89	 95.89	 99.80	 99.10
1400	 91.02	 94.85	 89.35	 91.45	 89.35	 91.45	 95.89	 95.89	 99.80	 99.10	 96.29	 96.29
1600	 89.35	 91.45	 89.35	 91.45	 95.89	 95.89	 99.80	 99.10	 96.29	 96.29	 96.29	 96.29
1800	 89.35	 91.45	 95.89	 95.89	 99.80	 99.10	 96.29	 96.29	 96.29	 96.29	 96.29	 96.29



**5 mm**

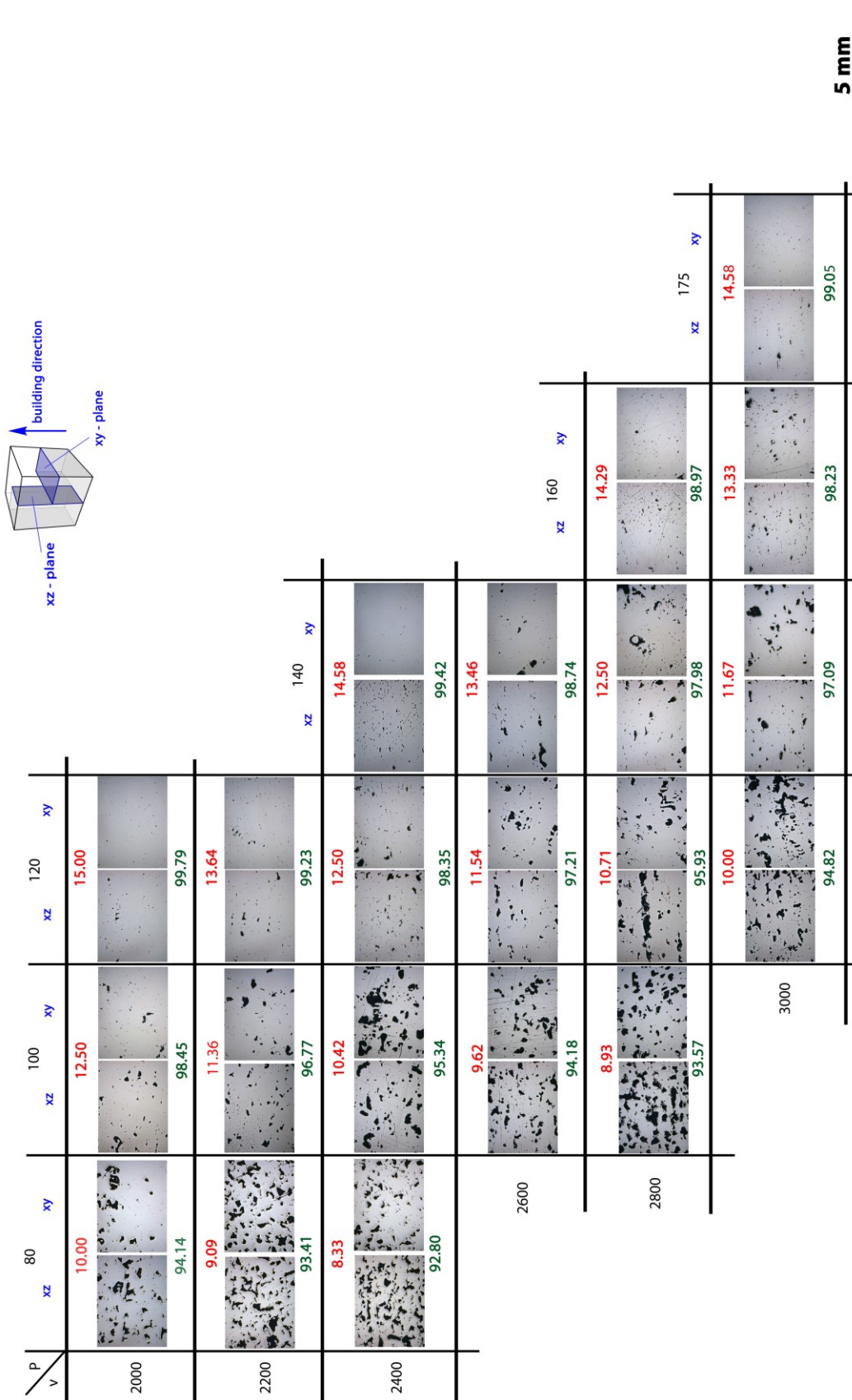


**$h = 0.20 \text{ mm}$**



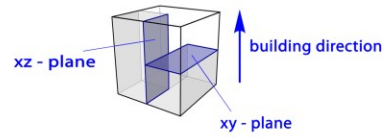
**5 mm**

**h = 0.08 mm**



**h = 0.06 mm**

P \ v	80					
	xz	xy				
1800	14.81					
	99.50					
2000	13.33					
	98.53					
			100			
			xz	xy		
2200	12.12		15.15			
	97.30		99.39			
2400	11.11		13.89			
	95.99		98.50			
					120	
					xz	xy
2600	10.26		12.82		15.38	
	94.15		97.82		99.11	
2800	9.52		11.90		14.29	
	93.24		96.80		98.47	
						140
					xz	xy
3000	8.89		11.11		13.33	15.56
	92.28		95.23		97.80	99.01

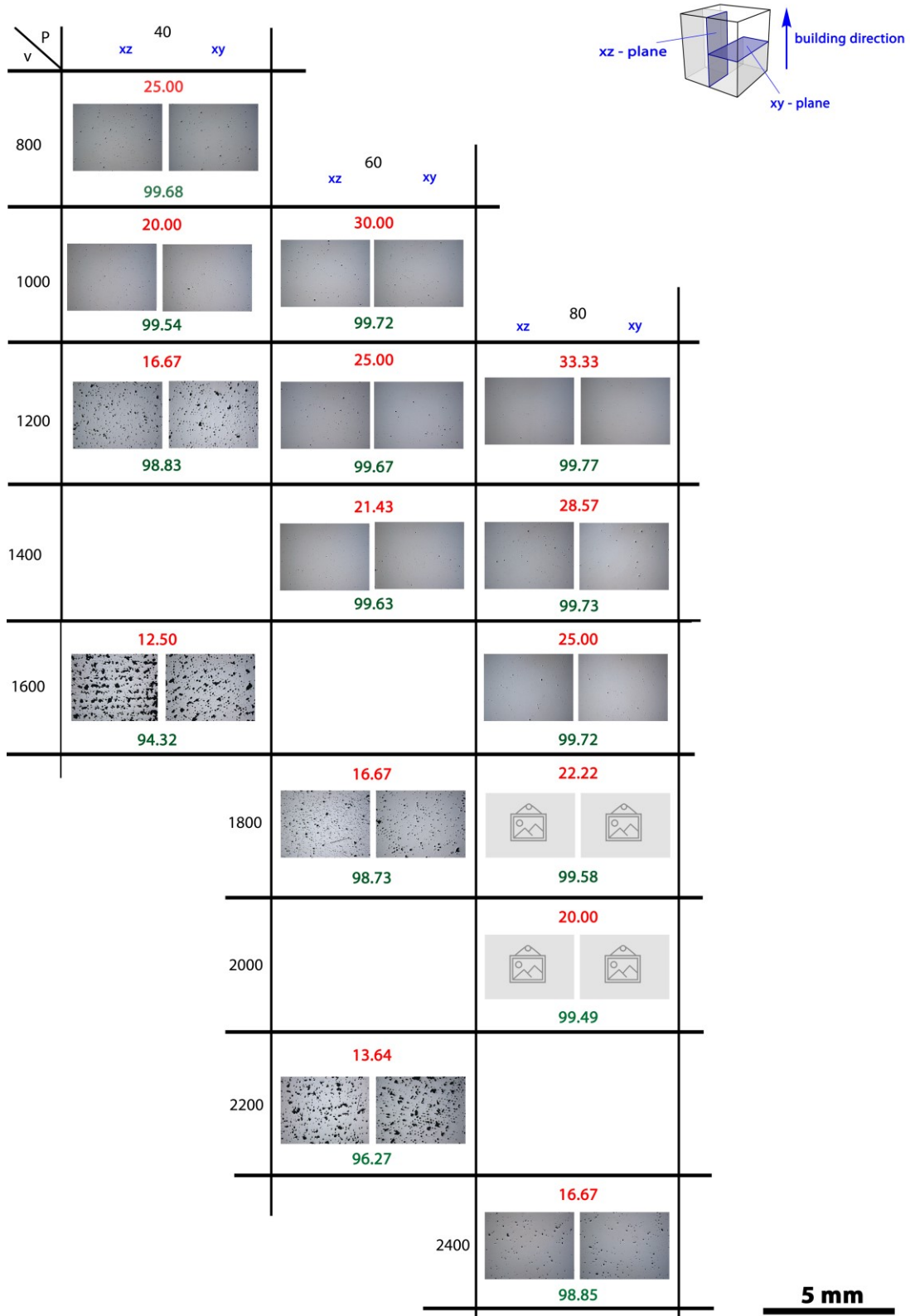


**5 mm**


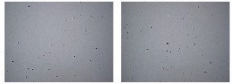
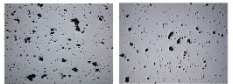
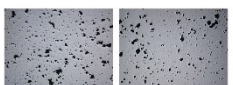

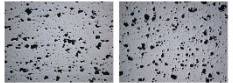
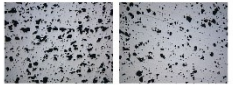
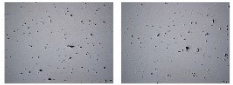
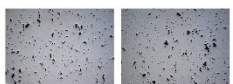


7.2.2. Layer Thickness  $t_{s2} = 0.02 \text{ mm}$

**$h = 0.10 \text{ mm}$**

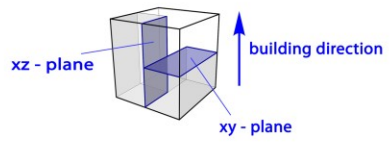
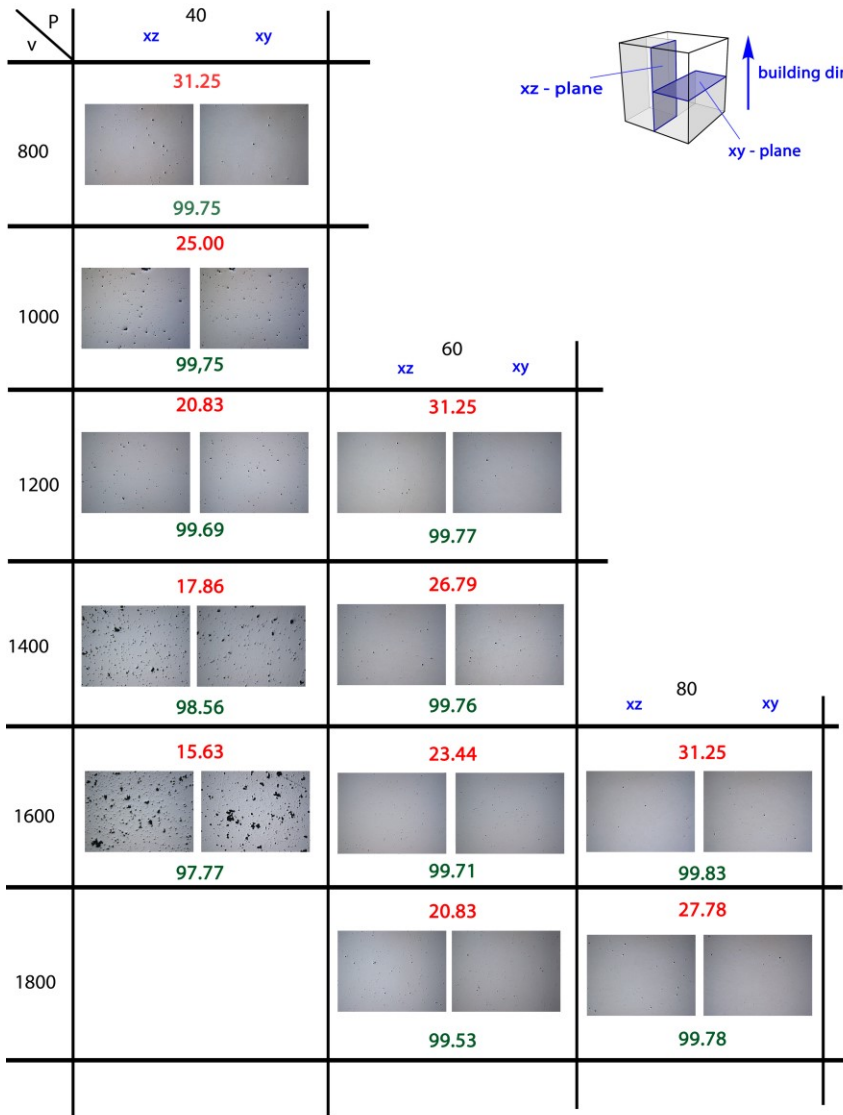


**h = 0.10 mm (continued from page 91)**

2000	<p style="text-align: center;"><b>12.50</b></p>  <p style="text-align: center;"><b>93.38</b></p>		<p style="text-align: center;"><b>25.00</b></p>  <p style="text-align: center;"><b>99.88</b></p>
		<p style="text-align: center;"><b>17.05</b></p>  <p style="text-align: center;"><b>98.47</b></p>	
	2200		
		<p style="text-align: center;"><b>15.63</b></p>  <p style="text-align: center;"><b>96.89</b></p>	<p style="text-align: center;"><b>20.83</b></p>  <p style="text-align: center;"><b>99.48</b></p>
	2400		
		<p style="text-align: center;"><b>14.42</b></p>  <p style="text-align: center;"><b>96.00</b></p>	
	2600		
		<p style="text-align: center;"><b>13.39</b></p>  <p style="text-align: center;"><b>95.00</b></p>	<p style="text-align: center;"><b>17.86</b></p>  <p style="text-align: center;"><b>98.86</b></p>
	2800		
			<p style="text-align: center;"><b>16.67</b></p>  <p style="text-align: center;"><b>97.83</b></p>
		3000	

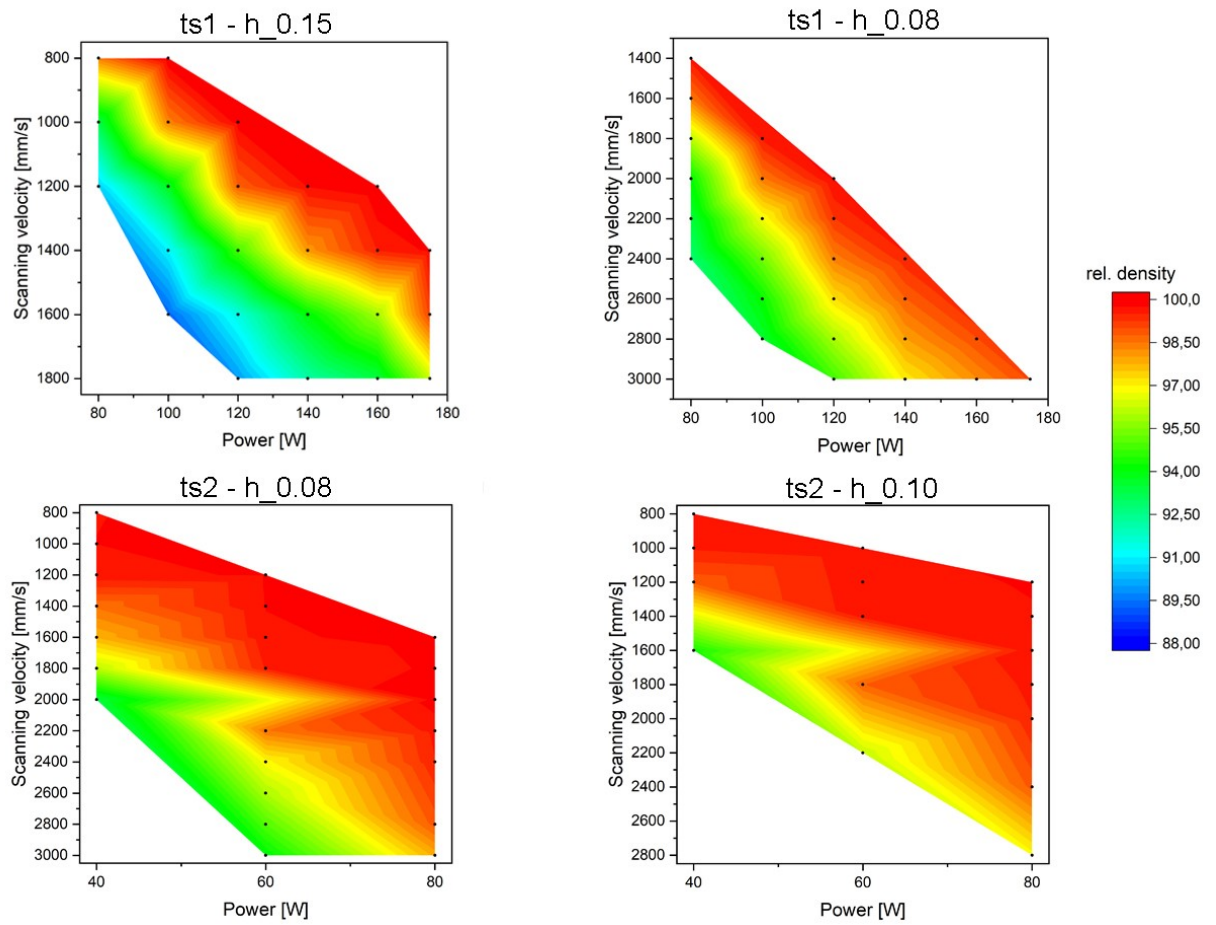
**5 mm**

**h = 0.08 mm**



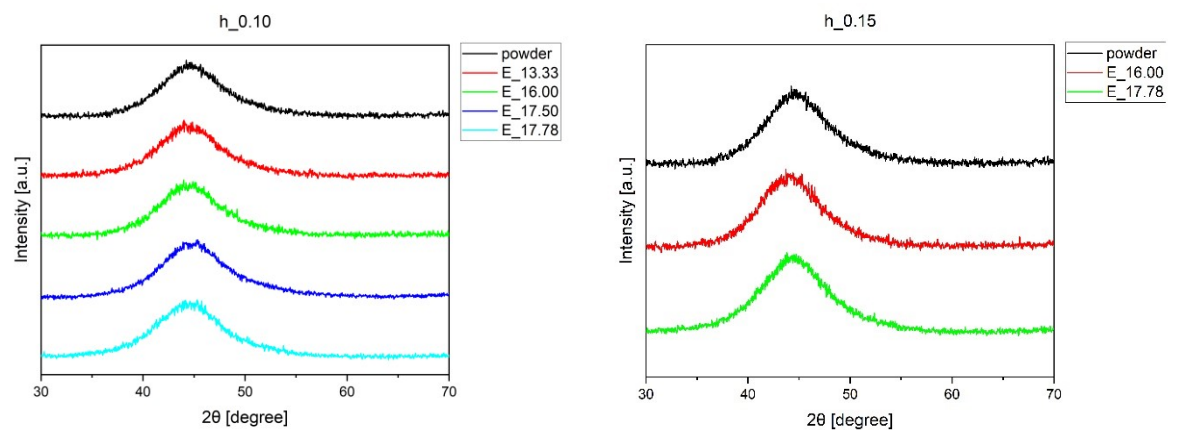
**5 mm**

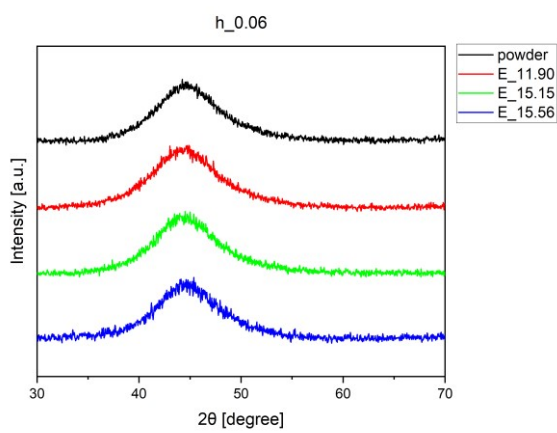
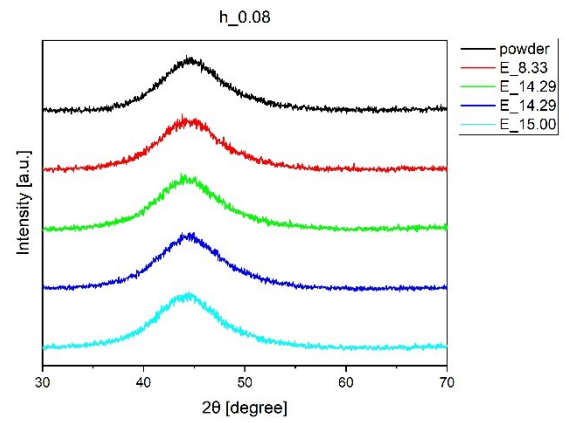
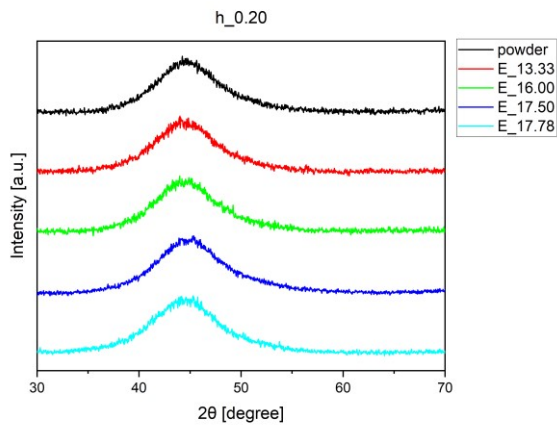
## 1.1. Relative Density - Further Density Contour Maps



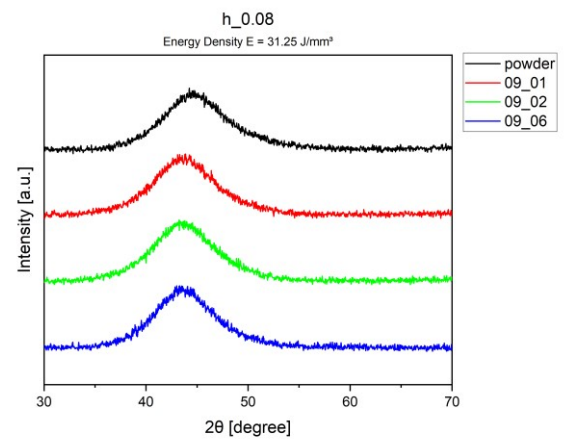
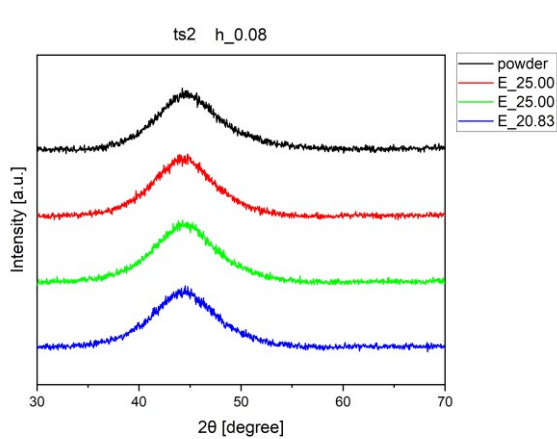
## 1.2. XRD Pattern of Samples of the Parameter Study

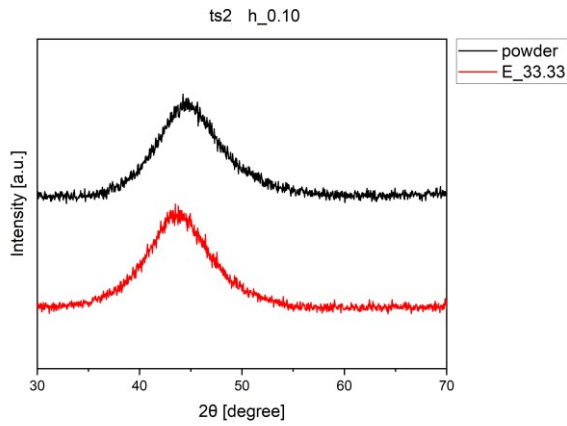
### 1.2.1. Layer Thickness ts1 = 0.05 mm



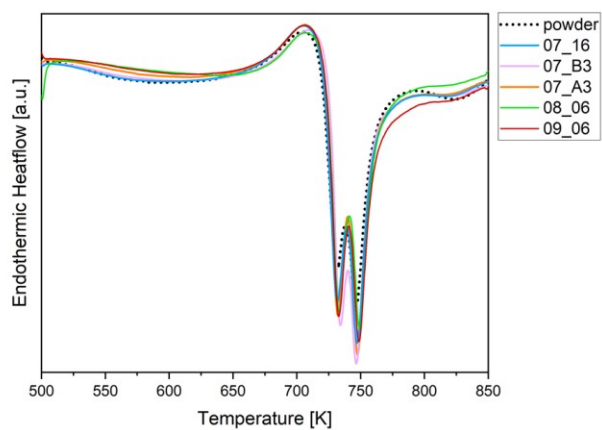
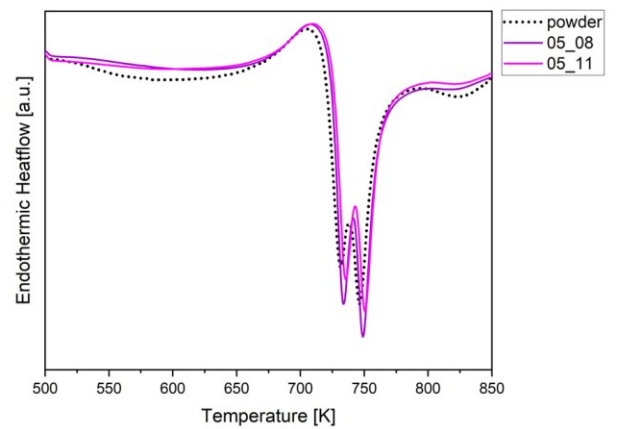
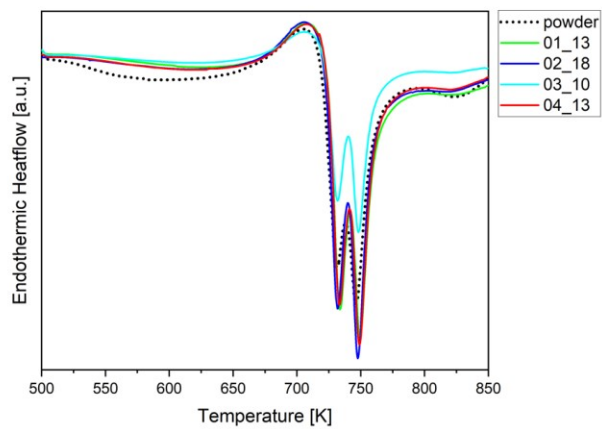


### 1.2.2. Layer Thickness $ts_2 = 0.02$ mm

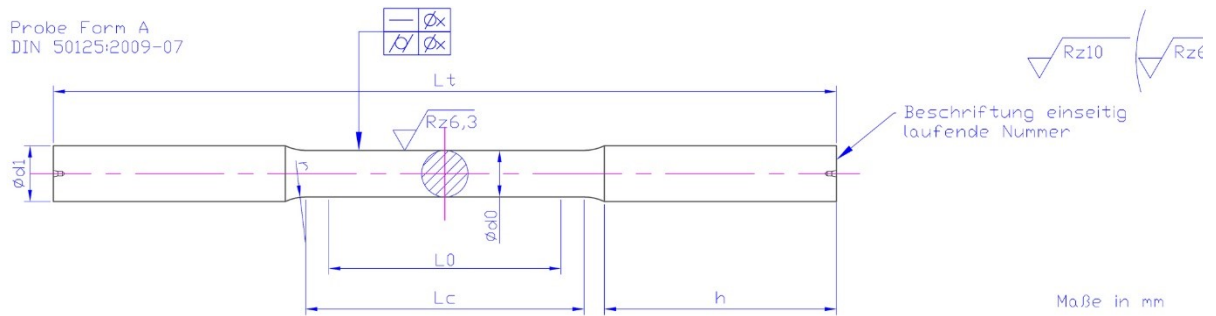




### 1.3. Further DSC Plots of Samples of the Parameter Study



## 1.4. Tensile Test Samples' chosen Geometry



Lt was changed to 85 mm →

Norm	d0	L0	d1	r min.	h	Lc min.	Lt min.	x
ASTM E8	4±0,1	16±0,1	6	4	50	20	125	0,0:
ASTM E8	6±0,1	24±0,1	8	6	50	30	137	0,0:

## 1.5. 4-Point Bending Tests – Samples' Dimensions and Results

### 1.5.1. 1<sup>st</sup> Test Series – vertically built Samples, different Surface Treatment

	Sample	b <sub>s</sub> (mm)	h <sub>s</sub> (mm)	F <sub>max</sub> (N)	Flexural Strength (MPa)	Displacement (mm)
As-built	ASB7	3.105	3.11	1788.69	1072	0.75
	ASB8	3.13	3.135	1914.95	1120	0.78
	ASB9	3.125	3.13	1575.02	926	0.68
	ASB10	3.1	3.1	1974.84	1193	0.85
glass	G1	3.02	3.02	2568.91	1679	0.76
	G2	3.005	3.015	2484.74	1637	0.76
	G3	3.04	3.035	2968.73	1908	0.89
corundum	K4	3.04	3.07	2797.15	1757	0.84
	K5	3.05	3.06	2570.53	1620	0.79
	K6	2.9	2.9	2324.48	1716	0.99

**1.5.2. 2<sup>nd</sup> Test Series – vertically built Samples, different Heat Treatment**

	Sample	b <sub>s</sub> (mm)	h <sub>s</sub> (mm)	Fmax (N)	Flexural Strength (MPa)	Displacement (mm)
As-built	12	3.06	3.04	3546.62	2257	1.09
	13	3.02	3.02	1654.33	1081	0.57
	15	3.025	3	3556.33	2351	1.11
	16	3.03	3.015	3608.13	2358	1.08
	17	3.03	3	3342.66	2206	1.04
	21	3.1	3.05	3193.74	1993	0.97
650K/60min	24	3.03	3.05	1226.99	784	0.69
	25	3.04	3.025	2206.32	1428	0.69
	26	3.035	3.04	2779.34	1784	0.83
	27	3.035	3.045	3137.08	2007	0.95
	28	3.03	3.035	2114.05	1363	1.03
	29	3.05	3.04	2444.27	1561	0.79
850K/60min	40	3.04	3.02	255.76	166	0.11
	41	3.05	3.025	276.8	179	0.14
	42	3.05	3.02	246.05	159	0.11
	43	3.055	3.005	326.98	213	0.14
	46	3.08	3.025	288.13	184	0.14

**1.5.3. 3<sup>rd</sup> Test Series – horizontally built Samples, different Test Orientation**

	Sample	b <sub>s</sub> (mm)	h <sub>s</sub> (mm)	Fmax (N)	Flexural Strength (MPa)	Displacement (mm)
H0°	H1	3.02	2.9	2436.17	1727	0.94
	H2	3	2.93	2625.56	1835	1.04
	H3	3.03	2.89	2555.96	1818	1.06
	H4	3.025	2.88	2811.72	2017	1.87
	H5	3.01	2.89	2353.62	1685	1.06
H180°	H6	3.02	2.88	3600.03	2587	1.29
	H7	3.03	2.92	3321.61	2314	1.52
	H8	3.035	2.88	3379.89	2417	1.4
H90°	H9	2.86	3.035	3719.82	2542	1.45
	H11	2.89	3.025	3582.23	2438	1.34
	H12	2.85	3.015	3661.55	2544	1.41
	H13	2.85	3	3061	2148	1.66
	H14	2.89	3.01	3454.35	2375	1.42
	H15	2.86	3.02	3546.62	2447	1.45